Near-Field Imaging of Microwave Circuits with Electromagnetic Probes

by

Ruifeng Zhai

A Thesis

Submitted to the Faculty of Graduate Studies

in Partial Fulfillment of the Requirements

for the Degree of

Master of Science

Department of Electrical and Computer Engineering

University of Manitoba

Winnipeg, Manitoba

Canada

THE UNIVERSITY OF MANITOBA

FACULTY OF GRADUATE STUDIES

*****

COPYRIGHT PERMISSION

Near-Field Imaging of Microwave Circuits with Electromagnetic Probes

BY

Ruifeng Zhai

A Thesis/Practicum submitted to the Faculty of Graduate Studies of The University of Manitoba in partial fulfillment of the requirement of the degree

Of

MASTER OF SCIENCE

ABSTRACT

The focus of this thesis is to investigate the feasibility of utilization of non-contact near-field probing techniques with miniature electromagnetic probes to evaluate the performance of Microwave Integrated Circuits (MICs). Unlike conventional microwave measurement methods, such as using a vector network analyzer to directly probe the pins of the circuit under test, non-contact near-field probing techniques are non-invasive and capable of measuring at arbitrary spots within the circuit with potentially high temporal and spatial resolution. The thesis gives an overview on non-contact probing systems currently developed for signal measurement and waveform extraction techniques and near-field mapping and imaging techniques.

For the purpose of investigating the feasibility of non-contact near-field measurement techniques, an automated near-field probing platform was developed. An analytic model of the probing system was derived and discussed. Both electric and magnetic probes (monopole probe, coplanar waveguide probe, and single/multi loop probe) were designed, fabricated and installed onto the platform for various applications. Approximate circuit models for these probes were created and analyzed. Various microwave circuits, including coplanar waveguide transmission line (CPW), single patch antenna and microstrip antenna array, were tested by using the near-field probing system. To verify the measurement results of CPW structures using the electric near-field probing system, the electric field variation over the surface of a CPW circuit was numerically evaluated by using a finite difference approach, with a SOR iterative matrix solver, to solve the Laplace Boundary Value problem.

In order to improve the spatial resolution to enable application to on-wafer microwave circuit probing, a micro-fabricated CPW probe, at a scale less than 100 μm, was evaluated using a micromachining process at the Alberta Microelectronics Centre. The fabricated probe was installed onto the automated near-field probing platform and measurement of coplanar waveguide transmission lines was made.

Single-loop and multi-loop magnetic near-field probing was investigated as an alternative to the electric near-field probing technique as a method of production line testing of printed circuit boards. The magnetic near-field probes were used to determine the detection capability of faults in multi-layer Printed Circuit boards. Both indirect and direct excitation measurements were conducted and evaluated. The signal frequency in such applications is limited up to 300 MHz range, and strong coupling between probes was found to have considerable impact on the performance of this near-field measurement approach.

ACKNOWLEDGEMENTS

I would like to express my gratitude to my supervisor, Dr. Greg Bridges, whose expertise, understanding, and patience, added considerably to my graduate experience. I appreciate his vast knowledge and skill in the areas of electromagnetics and microwave, scanning probe technologies and microelectronics, and his assistance in writing reports. I would like to thank the other members of the SPM Lab for the assistance they provided at all levels of the research project.

I would also like to thank my family for the support they provided me through my M.Sc. program and in particular, I must acknowledge my wife, Liting, without whose love, encouragement and editing assistance, I would not have finished this thesis.

The financial support from the National Sciences and Engineering Research Council of Canada (NSERC) is also gratefully acknowledged.

TABLE OF CONTENTS

TABLE OF FIGURES

Chapter 1 INTRODUCTION

The research work completed in this thesis is to investigate the feasibility of applications of electromagnetically coupled probes as non-invasive diagnostic tools for a broad range of microwave circuits. An automated measurement system has been designed and built capable of producing information unavailable from conventional measurement techniques.

1.1 Motivation

Rapid advances in the microelectronics field have enabled the development of faster, denser and more complicated microwave integrated circuits (MICs). The ability to test the performance of a particular technology underlies the progress in developing that technology. It is therefore important to develop appropriate tools to accurately evaluate the performance of these circuits and devices. The increasing chip complexity has made circuit modelling difficult and the prediction of circuit behaviour by computer simulations alone is inadequate, Accurate measurements for device evaluation are sequentially essential. On-chip waveform measurements are often required for complete characterization of devices and for failure analysis purposes. Measurements within a circuit are carried out using internal probing techniques with the device driven by external sources. While the miniaturization and the enhanced speed performance of integrated circuits are constantly being improved, the experimental measurement of these circuits is becoming increasingly difficult. In fact, the performance characteristics of many devices, especially those based on GaAs technology, have surpassed the capability of conventional electronic measurement techniques.

Present measurements require probing techniques capable of measuring Gigahertz signals with sub-micron spatial resolution and milli-volt sensitivity. The complexity of

integrated circuits presents a number of challenges during testing at the chip level. The ideal probing techniques should enable measurements with high temporal and spatial resolution, high sensitivity and low invasiveness. The measurement method should also be simple to operate and enable accurate results. Currently available instruments do not completely satisfy all these requirements. It is therefore important to develop alternative probing techniques.

Conventional circuit measurement techniques rely on some form of direct electrical contact with the point in the circuit being monitored. For example, digital integrated circuits are injected with test patterns and the outputs are monitored to determine the overall functionality of the circuit. This approach, however, does not provide any information on the identification of individual internal faults when one arises. Likewise, conventional network analyser measurements on microwave circuits impose similar limitations. Typically individual components are designed with a high degree of accuracy and reliability, however the integration of several components on a common substrate often gives rise to uncertainties in circuit performance. Often the performance is degraded by mutual coupling of elements due to the excitation of surface waves, particularly at millimeter wavelengths. Network analyser measurements at the device input and output ports are incapable of isolating such problems.

An ideal measurement technique should be non-invasive and capable of measuring waveforms at arbitrary points within the circuits. Depending on the application it may be desirable to perform voltage and/or current measurements, preferably with magnitude and phase data. In addition, the measurement system must possess sufficient spatial and temporal resolution. Developing a measurement system with such characteristics is challenging and critical to the future development of reliable high quality integrated circuits.

For this purpose, the feasibility of using eletromagnetically coupled probes as non-invasive diagnostic tools has been investigated. Probes are in various structure and shape,

including monopole, coplanar waveguide transmission line and looped-wire. Probes are also in various physical sizes, from millimeter level down to μm level. An automated measurement system has been also designed and constructed capable of yielding information acquired by these probes.

1.2 Thesis Outline

Chapter 1 is an introduction of the research work to bring out the thesis.

In chapter 2, a review of the non-contact probing measurement techniques currently researched and developed within industry and academic community is presented. The relative advantages and disadvantages of each technique are discussed and sample measurements are provided.

A description of the hardware and software required for the automated data acquisition system is given in chapter 3.

Chapter 4 discusses the properties of monopole and CPW probes and presents the experimental results of measurements on microwave circuits, i.e. transmission lines, printed antennas.

Chapter 5 gives a description on procedure to fabricate μm level probes by micromachining technology through VLSI process.

Chapter 6 discusses the magnetic loop probe application of printed circuit board failure detection.

Finally, chapter 7 summarizes the research work and presents the future work.

Chapter 2 REVIEW OF NON-CONTACT NEAR-FIELD PROBING TECHNIQUES

With the advent of near-field microscopy, conversional radio frequency (RF) and far-infrared (FIR) microscopy have gained more attention in recent two decades because of their many applications including material characterization and integrated circuit testing [1] . This chapter gives an overview of non-contact near-field probing techniques, which will cover the signal measurement and waveform extraction technologies and the field mapping and imaging technologies. Topics on Electron-beam Probe station, Scanning Force Microscopy probing, Electrostatic Force Microscopy will be discussed for the signal measurement and waveform extraction technologies. The discussion on the field mapping and imaging technologies, including Electro-optic probing, Modulated Scattering probing and near-field Electro/Magnetic probing will also be presented.

2.1 Signal Measurement and Waveform Extraction Techniques

2.1.1 Electron Beam Probing

Electron-beam probing technique is fully developed and used in industry and research institutions. It is based on a modified scanning electron microscope as shown in Figure 2-1 [2] .

The electron gun generates low energy primary electrons. Emitted primary electrons are accelerated through a potential on the order of 0.5 to 2.5 kV and focussed via a lens focussing system to a submicron spot on the device under test. On impact with the device under test, low energy secondary electrons are randomly emitted as a result of elastic collision. It can be seen in Figure 2-2 [5] that probing a +5V transmission line will emit less secondary electrons than that of a -5V line. This is due to low energy electrons being

attractive to the metal conductor by the positive potential of the +5V line while the negative potential of the -5V line repels such electrons.

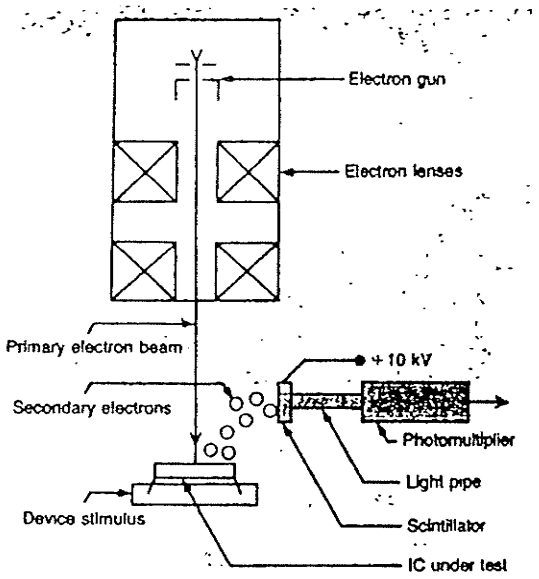

Figure 2-1 Electron beam probing equipment [2]

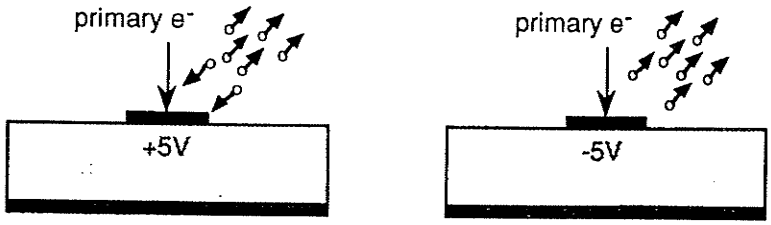

Figure 2-2 Secondary electrons (a) trapped by +5V potential; (b) repelled by -5V potential [5]

The secondary electrons are then collected and counted. The method of collecting the secondary electrons involves using either a high potential electrostatic extraction field generated at the surface of the device under test or a magnetic extraction field. The secondary electrons are fed to a scintillator which converts the electrons to photons. These photons are received by a photomultiplier which generates a specific number of

electrons for each incident photon. In general, the number of secondary electrons is inversely proportional to the potential within a limited area of the point of impact of the primary electron beam. When the output of the photomultiplier is converted to an input of a video display, areas with a positive potential appear dark indicating low secondary electron yield, while negative areas appear bright showing high secondary electron yield. It is called voltage-contrast imaging [2] [3] .

In Figure 2-3 the address buffer output of a 4K Bit RAM is measured using the electron beam probe. A computer simulation for reference is also included. The computer simulation and the electron beam probe measurement compare favourably with a delay time of 2.2 ns, which is much improved due to a tiny loading capacitance on the order of 10^{-5} pF [4] . A variety of applications such as measuring internal waveforms on a 1K Bipolar PROM, a 1 GHz Gunn diode, a 4K MOS RAM can be found in [6] .

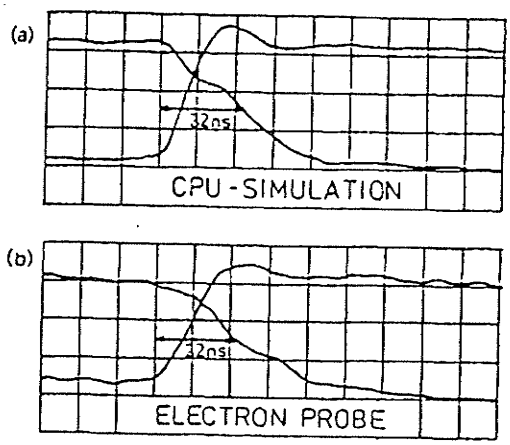

Figure 2-3 Waveforms at the address buffer output of a 4 Kbit RAM [4]

Probing bare conductors is relatively straightforward but probing buried (passivated) conductors presents additional complications. While probing buried conductors, the limitation is that only AC signals can be measured. Because the electrical behaviour of the buried conductor can be inferred from the surface measurement when the passivation

layer acts as dielectric which capacitively couples the surface potential to the buried conductor. For a DC signal, the coupling effect will not function.

Though electron-beam probing is attractive due to its high temporal resolution (1 ps – 1 ns) and submicron spatial resolution it is a complex and expensive technology with inherent limitations. It is required to follow some time consuming and expensive fabrication guidelines [3] . Improvement to make the DC signal measurement available on the buried conductors is also required. Crosstalk from the electric fields of nearby transmission lines is another factor that can affect the results by roughly 10% [4] . As the primary electrons are penetrating into the sensitive area of the device under test, especially for the MOS devices, the electrical characteristics of the device will be affected [4] [6] .

2.1.2 SFM based probing

2.1.2.1 Scanning Force Potentiometry

Scanning force potentiometry is performed by monitoring the electrostatic force on a conducting probe beam due to capacitively induced local charge on the circuit under test. The physical principle of this technique is the local interaction of an atomicly sharp tip mounted on one end of the cantilever and a device under test (DUT) due to the attractive or repulsive forces. The electrical interaction between the tip and the DUT causes a detectible bending of the cantilever.

An example of the direct capacitively-coupled probe has been designed by G. E. Bridges, T. S. Forzly and D. J. Thomson [7] [8] . The probes were fabricated from commercially available Si_3N_4 insulating cantilevers (100 μm long, 10 μm wide, 0.3 μm thick, with a single inverted pyramidal tip at their end.) A gold conducting electrode was deposited on the top side of cantilever beam to make the cantilever respond to the charge density in the localized region of circuit under test at the position of the tip and also to provide a signal line. A grounded conducting electrode was deposited on the bottom side

of beam to provide effective shield. The metalized probe beam and its pyrex support block were then mounted into a 50 Ω stripline feed structure as shown in Figure 2-4 [7] which was connected to a network analyser or spectrum analyser measurement system. The stripline feed is a ground-signal-ground structure and is designed to match the measurement system to the probe which is a parallel plate transmission line structure. Mechanical and piezoelectric manipulators attached to the stripline feed were used for lateral and vertical movement of the probe tip position. By monitoring the vertical position of the probe tip, topographical and electrical characterization can be performed. An equivalent circuit model of this probe was also developed for examining the expected probe resolution and detailed resolution analysis was given in [7] [8] .

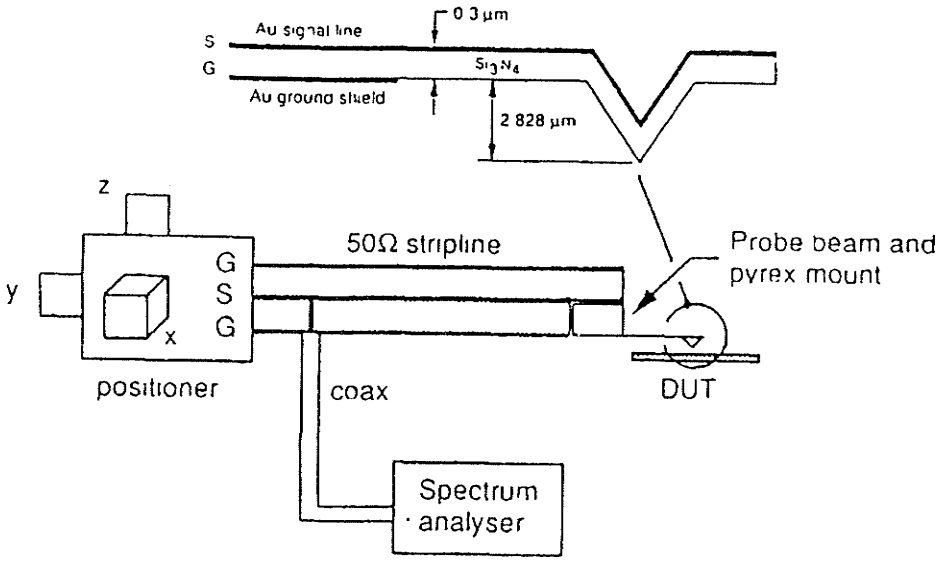

Figure 2-4 Probe measurement system and positioning [7]

The experimental result is compared to the simulation of scanning a transmission line in transverse direction with two tip-sample distances. Figure 2-5 [8] shows both experimental and numerical results for two scan paths. The first case, h1, is where the probe was scanned at a specific height above the transmission line. The second case, h2, involved scanning the probe tip directly across the transmission line in contact with the

S_iO_2 substrate. It was found that as the probe approaches either side of the printed line of transmission line the coupling capacitance and thereby the relative induced signal power increases. Both numerical simulation and experimental measurement yield a resolution of 15 μm for the system. The 15 μm spatial resolution is however still insufficient to examine many of the desired features of integrated circuits. Since the spatial resolution of this system is related to the geometry and the dimension of the probe, to enhance the performance of the test system, micromachined ultra-small tip is necessary while the trade-off should be concerned between the high spatial resolution and the lower signal power output due to the decreased coupling capacitance of the ultra-small micromachined probe.

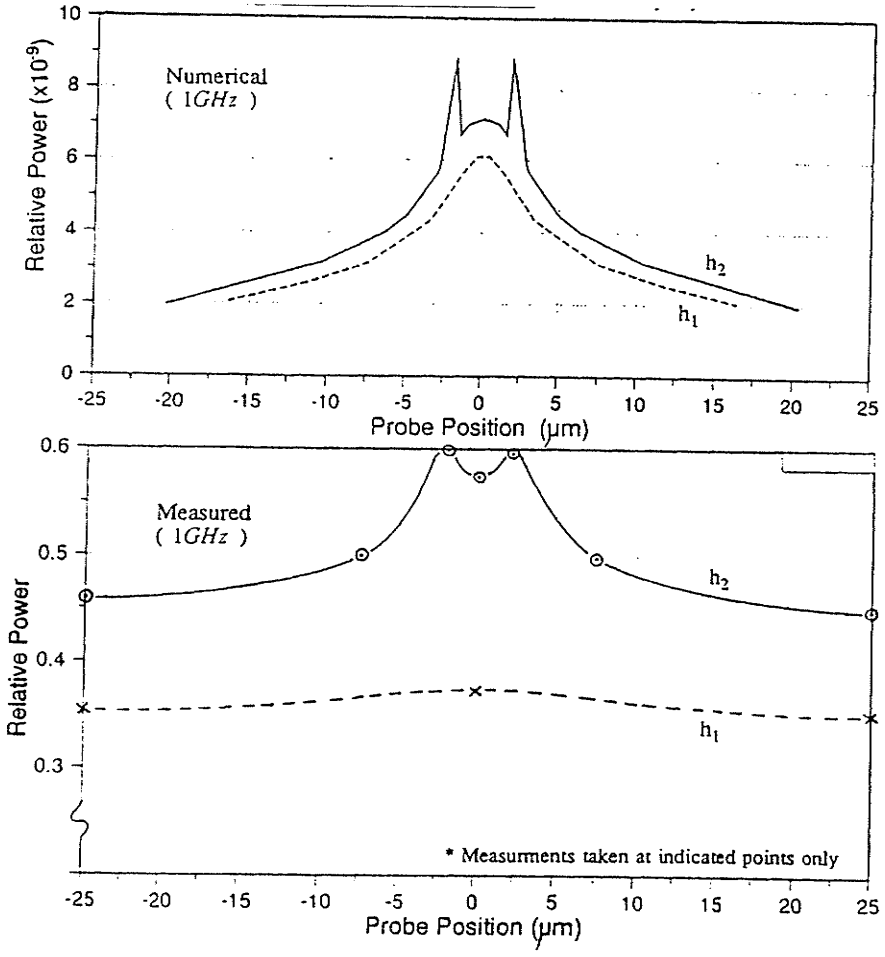

Figure 2-5 Probe measurement system and positioning [8]

C. Böhm et al. also employed the SFM-based test system for MMIC internal electrical characterization [9] . The frequency sweeping measurement was conducted up to 40 GHz to a set of coplanar waveguide structures and a travelling wave amplifier at selected internal test points on wafer. The measurement results were compared with that resulted by an external network analyzer, and demonstrated the feasibility to use SFM-based test system MMIC internal function and failure analysis because of the high spatial resolution (<500 nm) and the achieved high bandwidth (40 GHz).

2.1.2.2 AC Field Measurement with SFM Based Probing System

The active ACSFM is a non-contact measurement technique with high spatial and temporal resolution for AC electrical field measurement. ACSFM relies on the voltage difference V between the tip at the cantilever's end and that on the test point of device under test. The force F on the cantilever goes as [10] :

$$F = -\frac{\varepsilon_0 A(V_{tip} - V_{DUT})^2}{2z^2} \qquad (2\text{-}1)$$

where ε_0 is the permittivity of free space, A is the effective tip area, and z is the tip-sample distance. If the frequency of the voltage signal on the tip is slightly offset from that on the sample, an inner product results from the $(Vtip - V_{DUT})^2$ term which gives a sum and difference frequency. The difference frequency is a mechanical motion of the cantilever that can be detected using the tip-distance control feedback loop of the SFM. If the fundamental and several harmonics of this difference-frequency waveform fall below the first mechanical resonance of the cantilever, it can be displayed on a standard oscilloscope and interpreted as a low–frequency replica of the high-frequency signal on the sample. A. Leyk, et al. have used this technique to measure 104 GHz signals on the gate of a GaAs field-effect transistor [11] . While the established "cantilever-mixing" approach for ACSFM demonstrated the ability to probe devices with the required spatial and temporal resolutions, it has some significant weaknesses in which it needs to drive

the SFM cantilever with an AC signal, which alone can cause unwanted interference or perturbation, and which also should be phase synchronous with the unknown signal on the device. Furthermore, because it uses the motion of the cantilever for mixing, in its basic form it cannot simultaneously acquire topographical and field information; the tip-sample distance feedback loop of the SFM must be broken and the mixing product taken from this point will be the output signal. More importantly, it cannot regulate the tip-sample distance while measure the electrical field. Since compensation for drift during the measurement is made more difficult, there is poorer correspondence between topographic and field images, absolute voltage calibrations are difficult to achieve over the typical time of measurement. Finally, its reliance on standard SFM tip geometry permits long-range Coulomb interactions between the charge on the tip and that on conductors near to the one being measured, meaning that its "electrical resolution" – the ability to distinguish a signal on one conductor from that on a nearby conductor – is lower than its "topographical resolution".

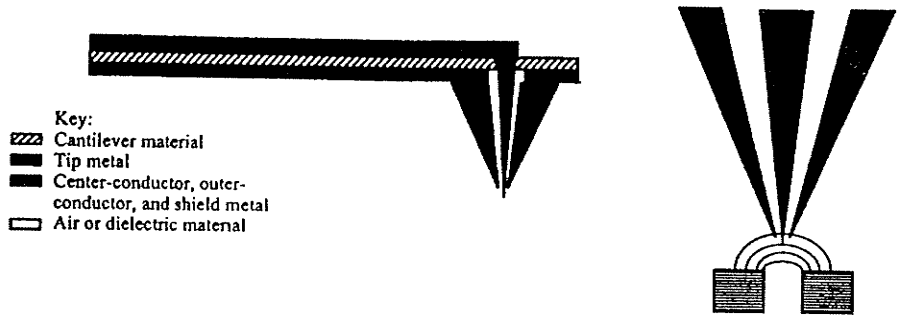

Figure 2-6 Schematic layout of combined SFM/coaxial tip with a coplanar waveguide along the cantilever and the close-up of coaxial tip probing electric field lines between two conductors [10]

To solve the problems in the above active ACSFM system, D. W. van der Weide and P. Neuzil designed a reactive nanoscilloscope that integrated a shield SFM/coaxial tip with a coplanar transmission line along the cantilever [10] . Figure 2-6 illustrates the first-order principle of the near-field probe. Assuming the conductor spacing is 1 μm and

the instantaneous voltage across the conductors is 1 V, a field of 10^4 V/cm exists. If the pitch of the coaxial probe is of the order of 0.1 μm, a voltage of 100 mV, which can be easily detected, develops between the tip and shield.

To realize the satisfactory operation at the nanometer scale, a micromachined silicon/polysilicon coaxial tip with outer shield has been designed (Figure 2-7 a)) [12] . The shield diameter is <100 nm while the tip radius is ~10 nm. The total height of the tip is >5 μm. D. W. van der Weide used this kind of probe to measure a 30 ps waveforms on the nonlinear transmission line (NLTL) diodes with a ~2 nm tip-sample distance while the NLTL was driven by a 2 GHz signal. The probe was estimated to have $R_{cantilever} \cong 10$ Ω, $C_{cantilever} \cong 0.03$ pF, and $L_{bondwire} \cong 0.5$ nH, and the tip–sample capacitance $C_{tip} \cong 0.4$ pF. The experimental results are shown in Figure 2-7 b). Although the three diodes are approximately equidistant from each other, the first one (diode A) had a distortion due to the waveguide bend just before it. The Figure 2-7 b) shows the expected spatial nonlinearity along the NLTL with a progressively steeper falling edge moving along the NLTL. This experiment was made by moving the probe with a step of < 0.1 μm along the NLTL.

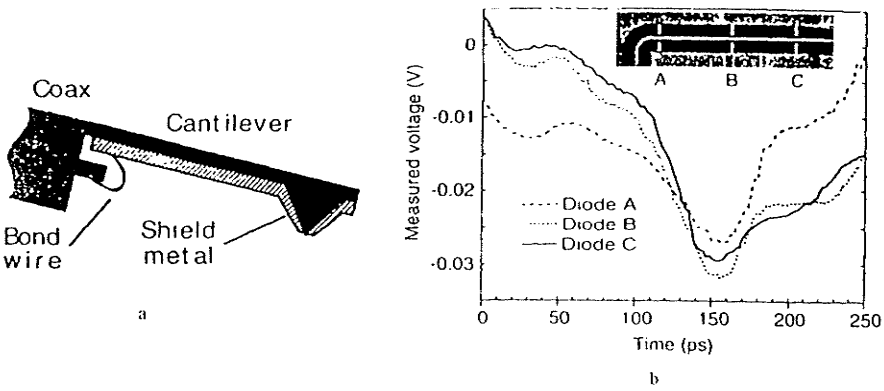

Figure 2-7 a) schematic arrangement of shield SFM tip/cantilever connected to a coaxial out cable; b) Excerpts from a linear scan along the NLTL diodes showing waveform compression at a 2 GHz [12]

Compared to the structure in the active ACSFM system, the techniques in the nanoscilloscope have several advantages. It no longer needs to drive the SFM cantilever with an AC signal. The cantilever height control feed back loop can be now used to maintain a constant distance from the sample as well as to compensate for any DC offset in the voltages between tip and sample. This technology can be calibrated. It can simultaneously acquire topographical and field information. Due to the shield around the central tip, limiting long range Coulomb interactions between the charge on the tip and that on conductors near to the one being measured, ACSFM's "electrical resolution" will be similar to its "topographical resolution". While we expect a wavelength-independent spatial resolution in the 10 nm regime, which is the radius of the probe tip, further theoretical and experimental work is needed to address the effects of finite tip conductivity, i.e., does skin depth affect resolution? The probe invasiveness must also be answered, though we note that by having control over the probe's geometry, its radiation impedance can be designed closer to that of free space, minimizing the invasiveness.

2.1.3 Noninvasive Electrostatic Force Microscopy

Noninvasive Electrostatic Force Microscopy has been developed for both static potential measurements and high frequency digital pattern extractions at internal points of integrated circuits [13] - [17] .

The block diagrams of test fixture are shown in Figure 2-8 [13] [14] for measurements of both localized potential and local digital pattern. A conducting wire probe with a sharp tip at the end is held in close proximity to the test circuit surface on which the potential $V_{DUT}(x, y)$, or $V_c(x, y, t)$ is to be extracted. The wire probe is configured so that it acts as a mechanical cantilever that can be deflected under an applied force. There is a small capacitor $C(x, y, z)$ formed and charged up between probe and circuit under test when a signal V_p externally applied to the probe to create a potential difference between them. The induced capacitive charge produces an attractive force resulting a deflection Δz of the probe cantilever.

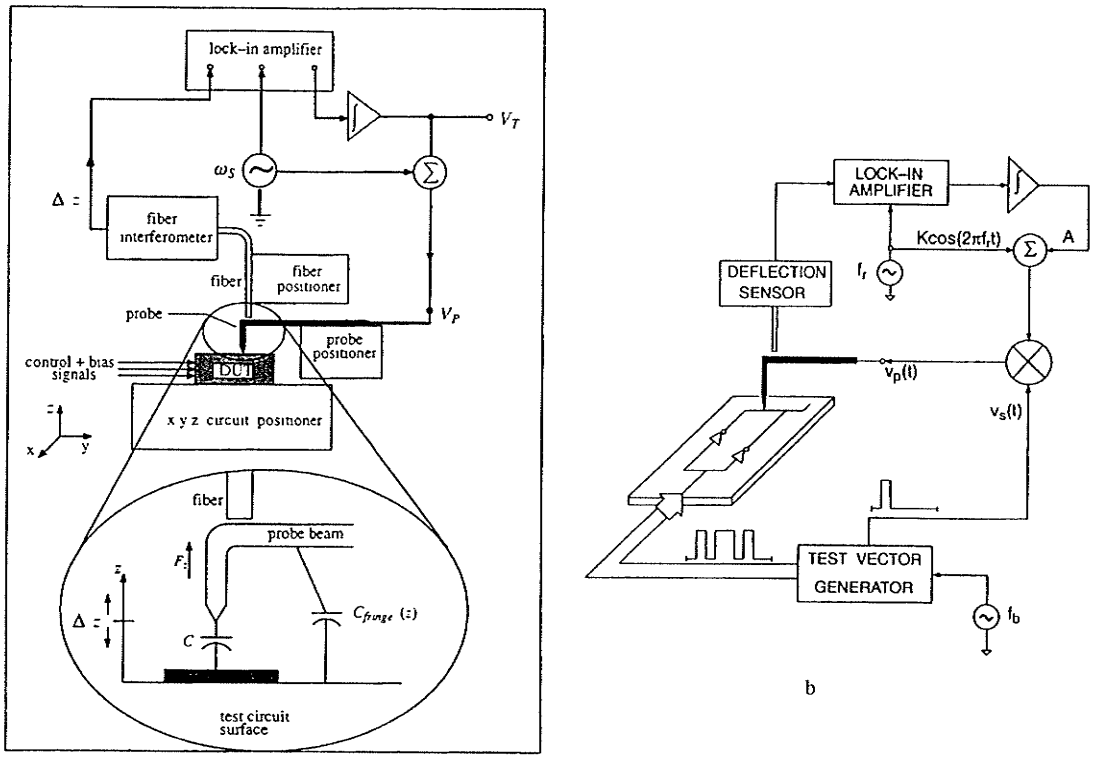

Figure 2-8 a) Diagram of the constructed potentiometric scanning-probe microscope [13] b) Pulse sampled heterodyne eletrostatic force measurement of the local digital pattern [14]

The force can be deduced from the relationship between force and stored energy on the capacitor as [14]

$$F_z = \frac{1}{2}\frac{\partial}{\partial z}C(x,y,z)[v_p(t) - v_c(x,y,t) + \Delta\Phi]^2 \qquad (2\text{-}2)$$

The term $\Delta\Phi$ has been added to represent DC offset effects such as those due to surface charge and material work function differences. A lock-in amplifier is used so the probe deflection at f_r only is monitored, which can be evaluated as

$$\Delta z\Big|_{f_r} = \frac{\partial C(z)}{\partial z} A(\omega_s)[(V_{DUT} - \Delta\Phi) - V_T]V_{ac} \qquad (2\text{-}3)$$

The capacitance derivative ∂C/∂z also has to be evaluated to determine the sensitivity of the instrument. G. E. Bridges and D. J. Thomson have addressed a numerical model [7] to give the analysis of variations of capacitance vs. distances.

By using the nulling technique in the instrument exact values for the terms *C'(x, y, z)*, *Q* and *k* are not required, thus eliminating the need for complex calibration and accurate probe positioning. These terms become important though when noise, sensitivity, and resolution issues are considered. Further, since the method is independent of *C(x, y, z)* measurement of passivated structures is possible without any modifications to the technique. This, however, comes with the penalty of a reduction in achievable spatial resolution due to increased circuit-probe spacing.

The core of nulling technique is to apply a sinusoidal signal of frequency as much close as the lowest mechanical resonant frequency ω_s or f_r in Figure 2-8. By adjusting the controllable parameter V_{adj}, which is either A or V_T, the cantilever or the probe deflection at ω_s is nulled, the potential level at the internal tested point of the integrated circuit can be determined (with a DC offset) as $V_{adj} = V_{DUT} - \Delta\Phi$

R. A. Said and G. E. Bridges have given out the results on resolution [13] , and one of the test structures is shown in Figure 2-9 a), which consists of several interconnect lines of 3 μm, 5 μm, and 10 μm in width. Cases both with and without a passivation layer on top of the interconnect lines were studied. For result shown in Figure 2-9 b) the substrate was grounded and both interconnect lines were fixed at a +5 V potential. The cover passivation was not present, with the probe located approximately 1 μm above the circuit surface and scanned transversally across two of the interconnect lines. Based on this result, and using the half voltage level as the reference, the resolution of the instrument for a probe height of 1 μm is approximately 3 μm. Measurements were also performed

with the presence of a 1 μm thick single passivation layer on top of the interconnect lines (Figure 2-9 c)). It could be seen that the difference between the peaks and between the measured potential and the actual applied potential of =5 V dc is greater than the case when no passivation layer is present. Also, the substrate region between the interconnect lines produces a higher measured potential. These differences are due to the increase in the nonlocalized coupling effects caused by the larger separation between the probe tip and interconnect lines. .

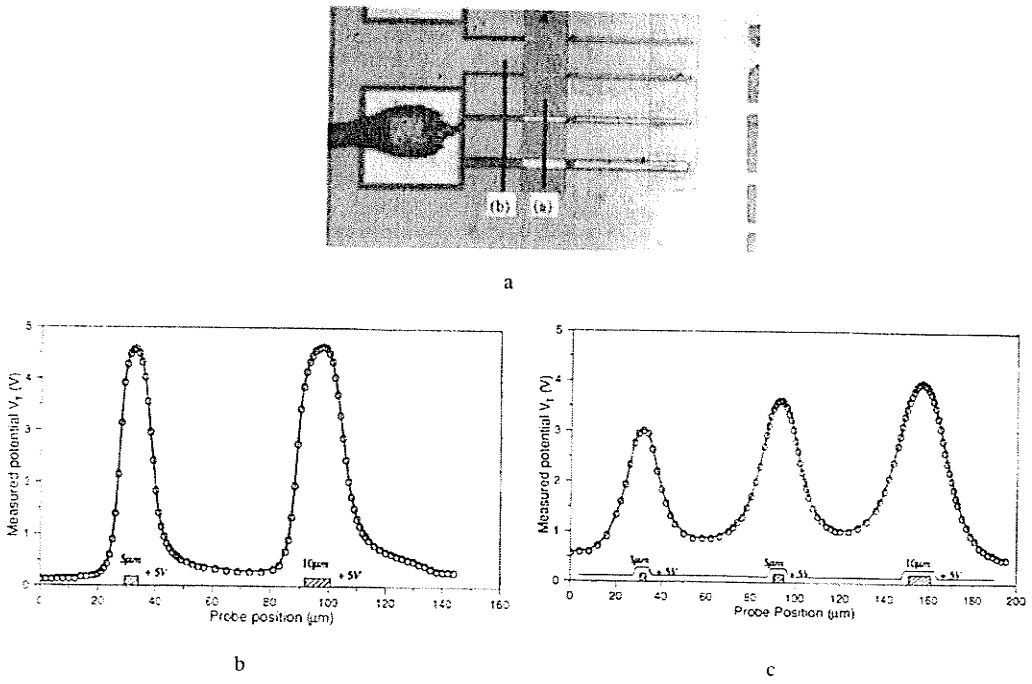

a

b

c

Figure 2-9 a) Interconnect test structure; b) Measured potential across two of the interconnect lines shown in figure a along path (a); c) Measured potential across three of the interconnect lines shown in figure a along path (b) [13]

By introducing a pulse sampled heterodyne technique into the above mentioned system, G. E. Bridges and R. A. Said, etc. have been able to internally extract the high frequency bit-by-bit digital patterns on wafer [14] . As shown in Figure 2-8 b), a multi-

channel test-vector generator supplies an N-bit patterns as indicated in Figure 2-10 a). This N-bit patterns repeat with a period $T = N/f_b = 1/f_0$, where f_b is the circuit clock frequency. Meanwhile, the generator also provides a high-frequency single-bit sampling pulse $V_s(t) = G_\delta(t - \tau_n)$. The sampling bit, as indicated in Figure 2-10 b), has a pulse width $\delta \leq 1/fb$ and can be shifted to a position τ_n along the N-bit test pattern. In this manner, the instrument will be able to measure the logic level of the nth bit of the pattern, i.e., $V_c(x, y, t = \tau_n)$.

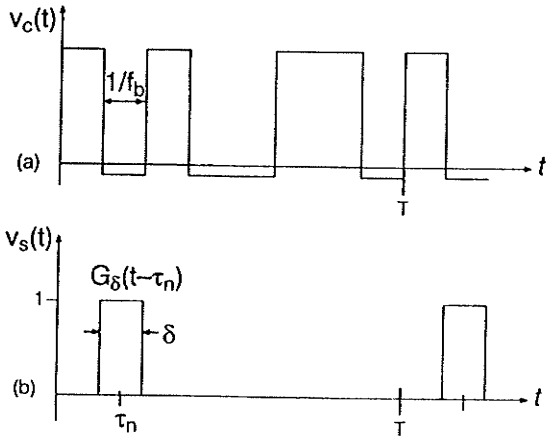

Figure 2-10 a) Example of periodic digital waveform v_c (x, y, t) to be measured; b) ideal sampling pulse $v_s(t) = G_\delta(t-\tau_n)$, which is shifted along the digital pattern [14]

For very high speed applications, the nonideality of the sampling waveform would be a constrain due to skew, finite rise and fall times, and possibly ringing. It requires that the digital signals be reasonably flat so that the unknown signal voltage levels can be determined when adjusting the parameter *A* to null the probe deflection. An 8-bit 1 Mbit/s digital pattern has been extracted with this technique from a CMOS test structure consisting of four 10 μm wide interconnects [14] . D. Noruttun and G. Bridges have achieved to be able to measure a 16-bit 125 Mbit/s pattern stream with an improved test fixture [17] . These results are shown in Figure 2-11.

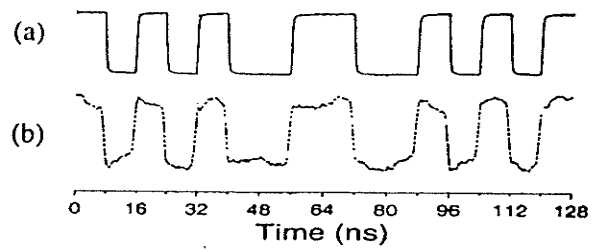

Figure 2-11 Measurement of 16- bit pattern at 125 Mb/s a) applied pattern from generator; b) measured waveform using EFM [17] .

2.2 Field Mapping and Imaging Techniques

2.2.1 Electro-Optic Probing

Electro-optic probing is a technology developed based on the well known electro-optic effect. When an electrical field is applied across an electro-optic medium the electron distribution is perturbed so that the polarizability and hence the refractive index of the medium changes anisotroptically. As a result, the polarization of the light passing through the medium is changed. This change which is linearly related to the electrical field is known as the Pockells effect and can be measured optically. Different types of electro-optic probing systems have been developed in order to obtain more detailed information about the electrical field distribution inside the complex Monolithic Microwave Integrated Circuits (MMICs). Internal (direct) and external electro-optic probing systems help improving electric models for semiconductor devices and support the development of new integrated circuits.

In direct/internal electro-optic probing system, the device under test is fabricated on a substrate that exhibits the electro-optic effect, such as GaAs. A pulsed and polarized laser beam enters the MMIC from the backside of the substrate. The electrical field in the substrate changes the optical properties of GaAs in such a manner that the orthogonal components of a laser beam polarized in the y-z plane and travelling in x-direction get a

phase retardation of $\Delta\Gamma(y, z)$, which is solely proportional to the electrical field component $E_x(x, y, z)$ being normal to the device surface (Figure 2-12 a)). The phase retardation can be transformed into an intensity variation $\Delta I(y, z)$ after the laser beam passing a Pockells-cell arrangement which is relatively a little complicated [18] [19] . Usually the intensity variation $\Delta I(y, z)$ can be detected by photodiodes.

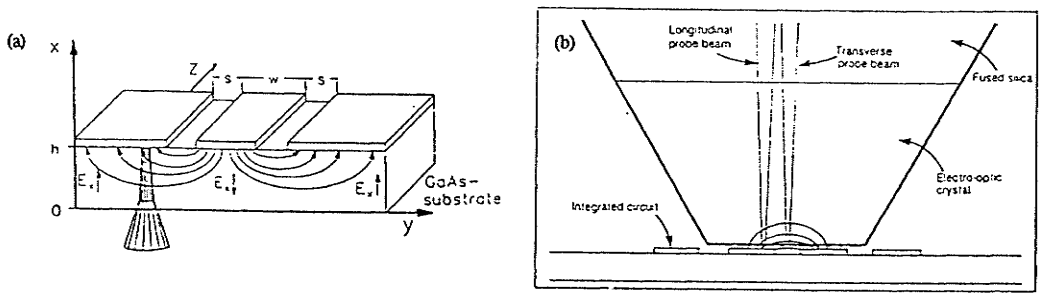

Figure 2-12 Common forms of electro-optic probing a) direct backside probing geometry for a coplanar waveguide; b) external electro-optic probing [5]

In contrast to the polarization analysis, there have been some reports about the Fabry-Perot enhanced internal probing [20] . The laser beam is focused on the MMIC from the backside of the substrate inside which the Fabry-Perot resonance is present. This approach requires an active wavelength control of the laser beam to assure the Fabry-Perot resonance to happen. To detect the resonance, a pair of focusing lens will be put in front of the reflected electro-optic signals from the MMIC. Whether the resonance is observable or not, it depends on the choice of the numerical aperture of the focusing lens which is limited by the maximum spatial resolution to be obtained.

For external electro-optic sampling (Figure 2-12 b)), the device under test need not be fabricated on an electro-optic substrate. Instead an electro-optic crystal is fused to the sampling probe head, hence allowing the electric fringing fields to penetrate the sampling crystal. The probe beam does not penetrate the device under test instead it is reflected off

a reflective coating on the bottom of the crystal. The electrical field from the MMIC around the bottom of the crystal will affect the polarization of the laser beam. Operating in either longitudinal or transverse probing mode is dependent on the type of the crystal utilized. An example measurement set up used shown in Figure 2-13 [21] . The optical beam from a phase-stabilized Ti:Sapphire laser (pulse length 50 fs) is focused inside the probe crystal. The reflected beam is analysed with respect to the change of the polarization state. Due to the phase-locked-loop-electronics of the laser system, it is possible to synthesize continuous wave (cw) signals from a microwave synthesizer to the laser pulse train so that measurements in amplitude and phase can be performed. The probes are fabricated from Bismuth Silicate (BSO) and Lithium Tantalate (LiTaO3), which allow the determination of the normal and tangential field components, respectively. The crystals have a footprint of 90 x 70 μm for the BSO and 84 x 84 μm for the LiTaO3. High spatial resolution is obtained by focusing the laser beam to a small spot at the bottom of the probe. The distance between probe and DUT can be adjusted to be 5-7 μm. The minimum detectable voltage is measured to be around 1 mv and the sensitivity is 40 $\mu V/\sqrt{Hz}$. The examined distribution network circuit is a coplanar design fabricated on high-resistivity Si with the designed working frequency of 5 GHz and15 GHz. Figure 2-14 and Figure 2-15 [21] demonstrate typical electro-optic mapping of the electric normal and tangential field components for a CPW even mode working at 5 GHz and 15GHz respectively in the transverse direction.

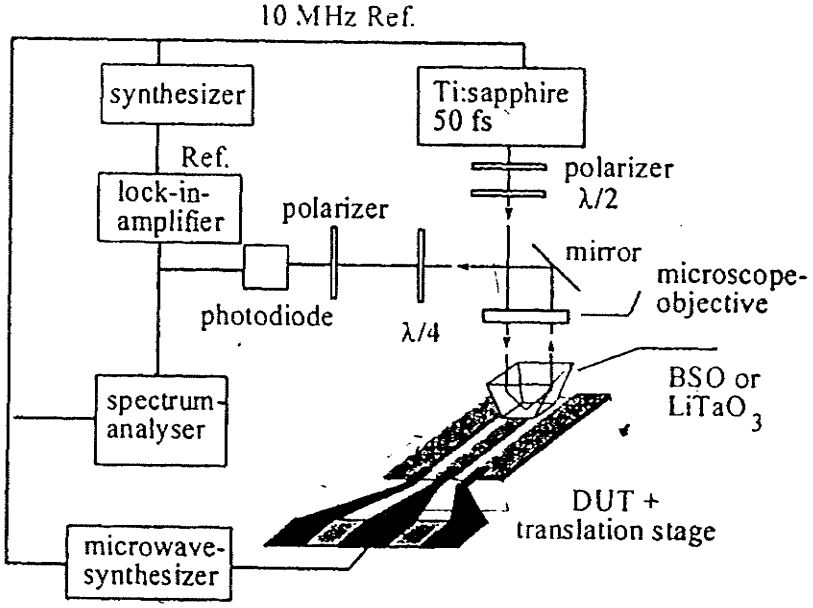

Figure 2-13 External electro-optic probe station [21]

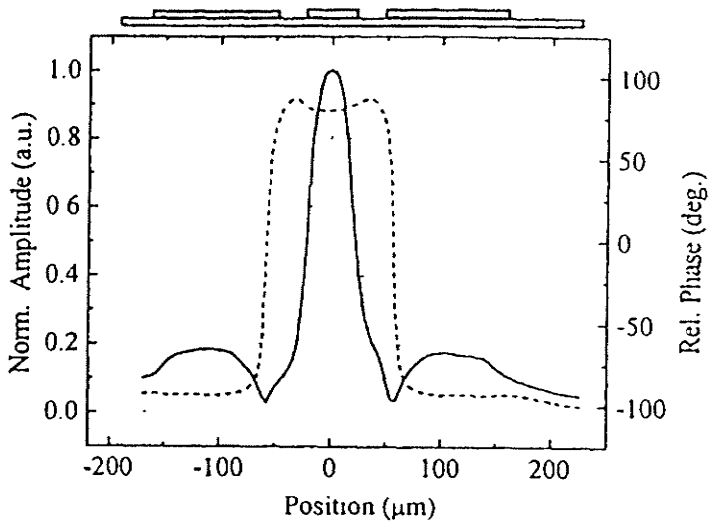

Figure 2-14 Electro-optic mapping of the normal field component of the CPW even mode - solid line: normalized amplitude, dash line: phase [21]

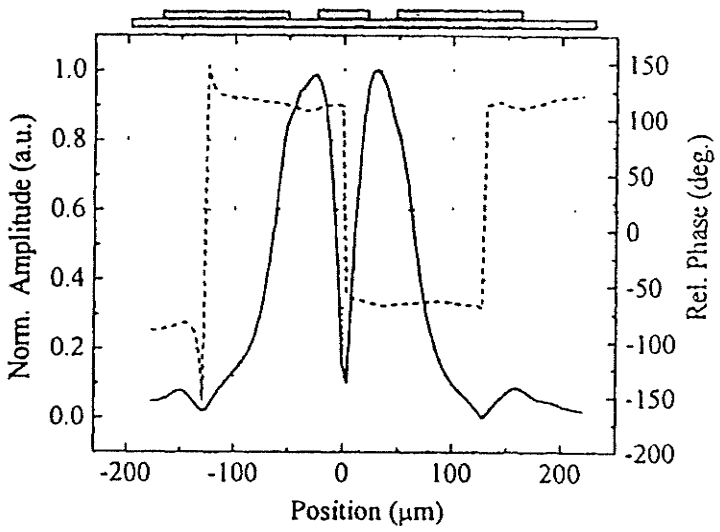

Figure 2-15 Electro-optic mapping of the tangential field component of the CPW even mode - solid line: normalized amplitude, dash line: phase [21]

The electro-optic probing is a complex and expensive technology. But for applications requiring high bandwidth and high spatial resolution, electro-optic probing is a promising candidate. This is because it provides THz bandwidth and a spatial resolution the size of the laser beam diameter or even less. One issue which requires considerable attention is that of system calibration, such as for the internal Fabry-Perot electro-optic probing system, the determination of the wavelength of the laser beam to ensure the Fabry-Perot resonance in each position of the MMIC due to the inconsistent thickness of the substrate. Another inconvenience is that for internal electro-optic probing system, its application is limited only for testing DUT fabricated on special substrate that exhibits electro-optic effect, such as GaAs. Finally, another area of uncertainty is the possible capacitive loading of the electro-optic crystals such as LiTaO3 in the external electro-optic probing system. The perturbation of the electric field above the DUT may affect the normal operation of the DUT. In spite of these difficulties, electro-optic sampling shows great promise as a high speed and resolution measurement technique for a broad range of devices.

More applications of the electrooptic probe are demonstrated to diagnose the microstrip patch antenna [22] and horn antenna for active amplifier array [23] . In addition to the two-dimensional movement of the DUT, several optical components have freedom of movement in the vertical direction, so that one may achieve a three-dimensional field-mapping capability. The minimum detectable power emanating from the patch is measured to be about 45 dBm, where it corresponds to a field strength at the probe of approximately 30 V/m, and the sensitivity of the measurement system is 40 mV/ Hz. The results have been used to evaluate the performance of the arrays and identify important design issues. The high resolution and accuracy of the electrooptic field-mapping technique has proven to be advantageous in the design cycle of amplifier arrays, and has diagnosed problems such as nonuniform bias, nonuniform feed amplitude, and malfunctioning monolithic microwave integrated circuits (MMICs).

A major factor that has yet to be considered when applying electrooptic field mapping techniques to the characterization of active microwave circuits is the temperature dependence of the probe itself. The electrooptic coefficients that govern the response of the probe to RF fields are known to vary with temperature [24] . The flow of optical power P through the semiconductor is found to obey the temperature dependence, $1/P \propto 1 + kT$, k is a constant related to the dimension of the semi-conductor in the direction of propagation. A system was developed [24] to simultaneously measure the electric and thermal fields utilizing an electrooptic semiconductor probe (Figure 2-16). The Pockels effect is employed within a gallium–arsenide probe to measure electric fields, and the effect of photon absorption due to bandtail states in the semiconductor is used to determine temperature. By separating the electric field and temperature signals in frequency, both may be acquired with a single probe.

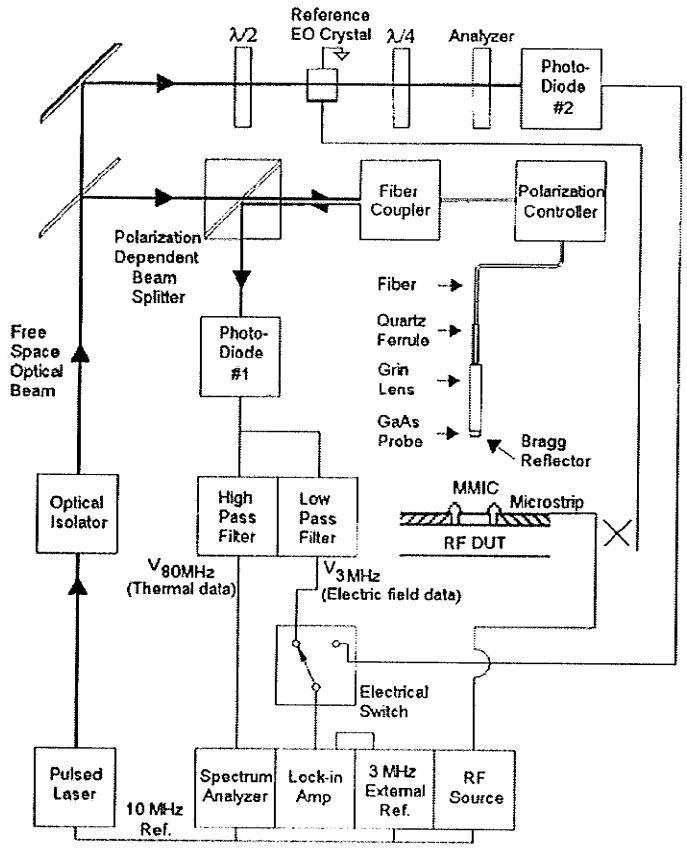

Figure 2-16 An experimental setup for combined electrothermal measurements [24]

Figure 2-17 clearly shows that there is a substantial difference between the behavior of the measured electric-field data obtained from the probe and the measured power from the independent power meter. The explanation for the discrepancy is shown in Figure 2-18 as the absorption data from the probe is seen to decrease with time along with the electric-field data. The change in the absorption signal is consistent with the expected increase in temperature in the vicinity of the biased MMIC due to the dissipation of heat. Calibration of the temperature effects of the probe on the electric- field measurements is possible since the absorption signal is linearly proportional to the electric-field signal. The temperature calibrated electric-field data is shown in Figure 2-19.

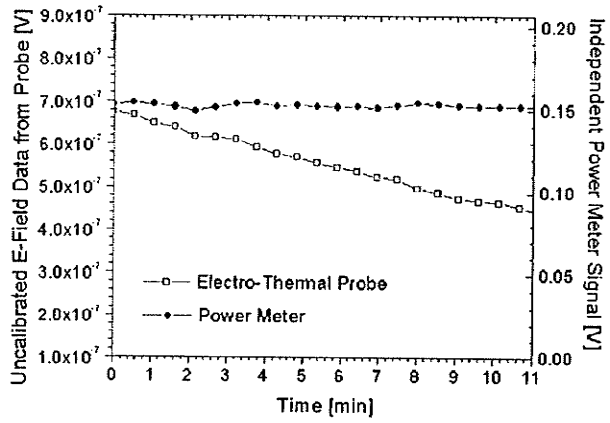

Figure 2-17 Probe and power-meter measurement of the MMIC [24]

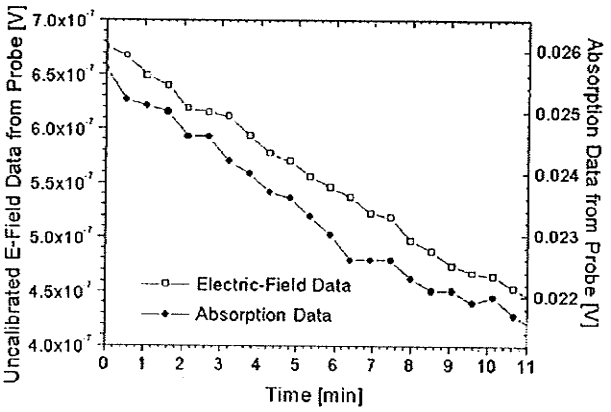

Figure 2-18 Probe-only measurements of the MMIC [24]

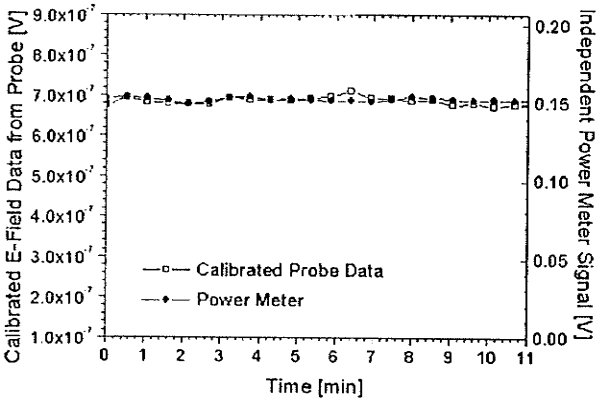

Figure 2-19 Temperature-calibrated electric-field data [24]

2.2.2 Modulated Scattering Technique

The modulated scattering technique is a low cost technology of electromagnetic field mapping of microwave circuits. As a part of the basic operation of the modulated scattering system, a small dipole scatterer with a diode mounted at the centre is placed in the near filed of the circuit of interest. By modulating the bias of the diode at a frequency much lower than the RF, a weak modulated scattered RF signal is returned to the transmitter. The strength and phase of the scattered signal are related to the square of the normalized electric field distribution intercepted at the position of the scattering probe.

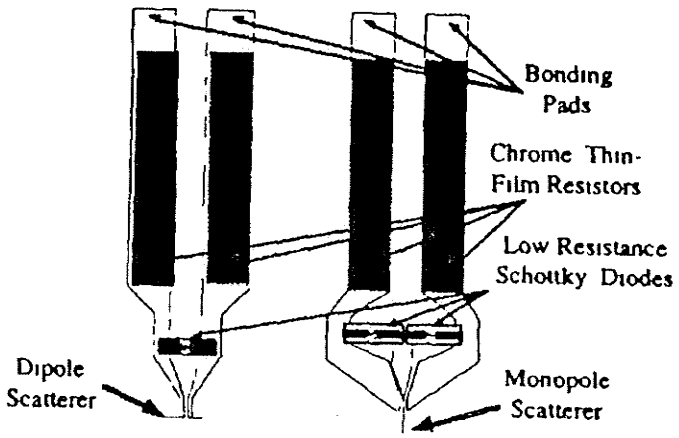

Figure 2-20 The near field scattering probes; The dipole is used for scattering the tangential electric field and the monopole is used for scattering the normal electric field [25]

Figure 2-6 [25] shows the design of the dipole and monopole scatterers. The probes are fabricated on 125 μm thick low loss quartz. Chrome resistive bias lines are used to absorb any RF fields that may propagate along the bias lines and also serve as current limiters to protect the diodes. These lines have a typical resistance of 100 Ω/mm. Commercially available low cost diodes are then silver epoxied between the dipole arms. For monopole scatterer, two diodes are placed between the CPW ground planes and the centre conductor. The diode has a 3 Ω series resistance, 0.25 pF junction capacitance and a 240 GHz cut-off frequency. The probes are fabricated using standard photolithographic

techniques with 1.0 μm thick gold. The monopole and dipole arms are both 100 μm and are expected to have 40 dB dynamic ranges.

The general set up of the modulated scattering system [26] is shown in Figure 2-21. In the RF section of the near-field modulated scattering experiment, part of the RF signal is sent as the LO to a wideband quadrature mixer as a reference. The other part is sent to the input port of the MMIC via a circulator which isolate the interference between the reflected scattered RF signal and the input RF signal. Usually the power scattered to the input/output port of the MMIC by the probe is small, homodyne mixing is used to detect the weakly modulated signal. The in-phase and quadrature IF voltages from the mixer are detected by a lock-in amplifier. Through the use of the absorptive RF switch, both the scattered reflected and scattered transmitted waves can be measured.

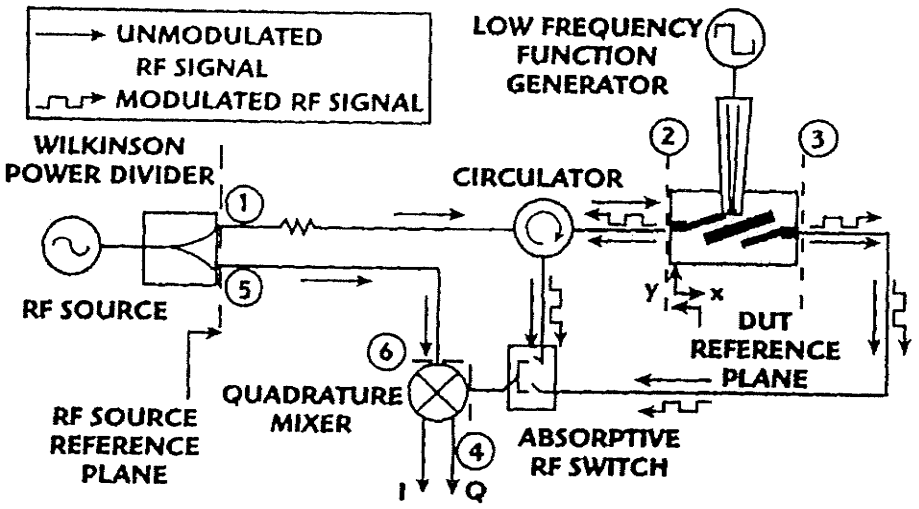

Figure 2-21 The microwave circuit electric field imaging system using modulated scattering probe [26]

The experimental measurements are verified by using a two inch long straight section of 50 Ω microstrip on RT/Duroid 5880 (ε_r = 2.2, h = 0.015″) at 9 GHz [25] . A monopole probe is scanned over the microstrip line with 50 Ω SMA termination in the match mode.

The raw data collected from the in-phase and quadrature signal are shown in Figure 2-22 a) and b). The maxima and minima along a transmission line for the in-phase and quadrature signal are separated by a distance $\lambda_{eff}/4$ (λ_{eff} = 26,000 μm). The normal electric field intensity and phase delay measurements are display in Figure 2-22 c) and d), respectively. The intensities are nearly constant along contours parallel to the microstrip. An intensity ripple of 0.1 dB is present which is due to the non-ideal match of the termination or non-ideal connections made with the SMA connectors. The phase cycles by 2π every 13,000 μm which is $\lambda_{eff}/2$ as can be seen in Figure 2-22 d). The slight angle in the phase is possible due to a variation in the height of the probe across the microstrip. Some measurements were also conducted to a three stage coupled-line bandpass filter at 10 GHz [26] [27] and a distributed amplifier MMIC at 13.5 GHz [26] by the modulated scattering probing.

As a low cost and flexible electromagnetic field mapping system, modulated scattering system is capable of mapping the normal and tangential electric field intensity and phase delay above a MMIC with any substrate in the frequency range of 0.5 to 18 GHz. The spatial resolution is limited by the dimension of the monopole/dipole probe. It is believed that the resolution can be pushed to 25 μm with smaller and thinner probes before the system becomes noise limit. Further more by using a system of circulator and absorptive RF switches the bandwidth and the signal to noise ratio can be greatly improved.

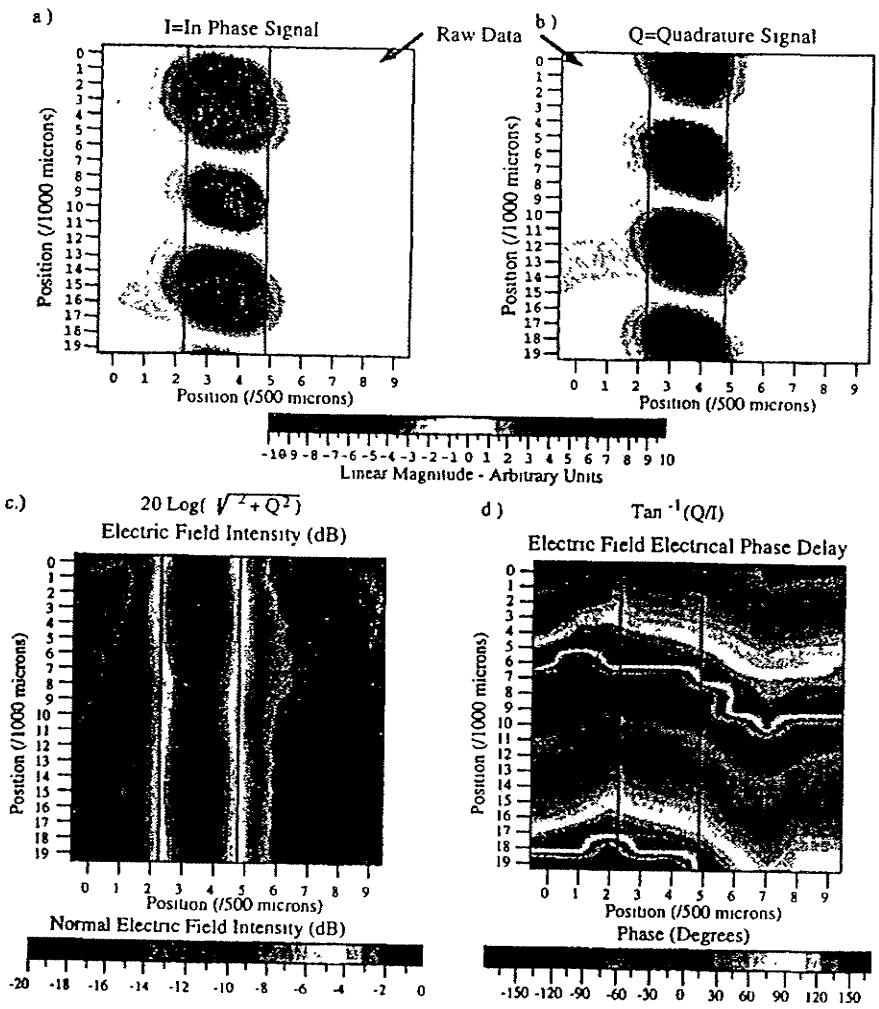

Figure 2-22 a) In-phase signal of normal electric field; b) Quadrature signal of normal electric field; c) Normal electric field; d) Normal electric field phase delay [25]

2.2.3 Passive Electromagnetic Probing

2.2.3.1 Double/Single Loop Magnetic Probe

The design of the magnetic field current probes started using conducting loops. It was assumed that the loop is immersed into a plane linearly polarized electromagnetic wave in free space and is placed in the *x-y*, *x-z*, or *y-z* plane, perpendicular to the magnetic field *Hz-*, *Hy-*, *Hx-* components, which are considered to be constant over the area of the loop.

The system resolution is limited by the dimensions of the loop probe which should be much smaller than the wavelength.

A double-loop magnetic probe has been developed by S. S. Osofsky [28] with the size of 15 mm x 7 mm for each loop and physical form of magnetic quadrupole (Figure 2-23). Its field configuration matches the fields of both microstrip and CPW, as shown in Figure 2-24. It was a large-scale model which can be easily constructed and tested in the 0.1-0.3 GHz range. The ultimate goal, however, is construction of probes useful at 20 GHz or higher by means of microfabrication technology. The advantage of this double-loop configuration is:

- For both microstrip and CPW, the waveguides' magnetic field goes up through one loop and down through another, their contributions add.
- Signals induced in the two loops by a nearly uniform field coming from a distant source, such as another waveguide in the microcircuit, tend to cancel.

The major concern of this method however is the electric asymmetry of the probe central conductor. That means the probe also works as an electric field probe in the perpendicular direction. This asymmetry disturbs the magnetic measurements, especially in the position where the magnetic field is minimum and the electrical field is maximum.

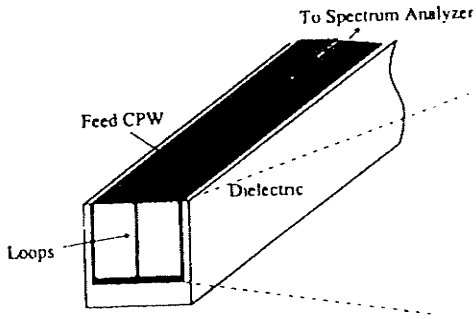

Figure 2-23 Double loop magnetic probe [28]

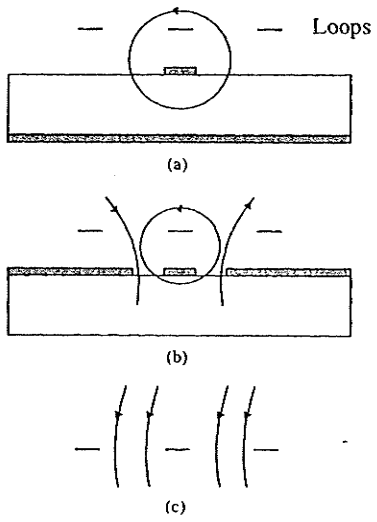

Figure 2-24 Double-loop magnetic probe coupling to magnetic fields of a) microstrip; b) coplanar; c) interacts between two loops [28]

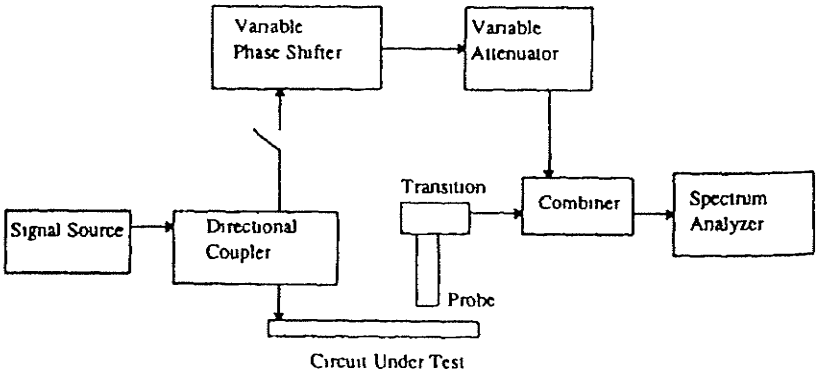

Figure 2-25 Measurement configuration [28]

A typical measurement configuration is shown in Figure 2-25. The current induced in the probe passes through the CPW transmission line to a spectrum analyser. By this means, measurements of current amplitude can be made. To make phase measurements, a reference signal of the same frequency and adjustable phase is added to the probe signal. The reference signal's phase is varied until the amplitude seen by the spectrum analyser

is maximum. The phase at the point of measurement is then compared with that at some other point of the circuit chosen as the reference. Thus the inherent phase delays of the probe and its transmission line are of no concern.

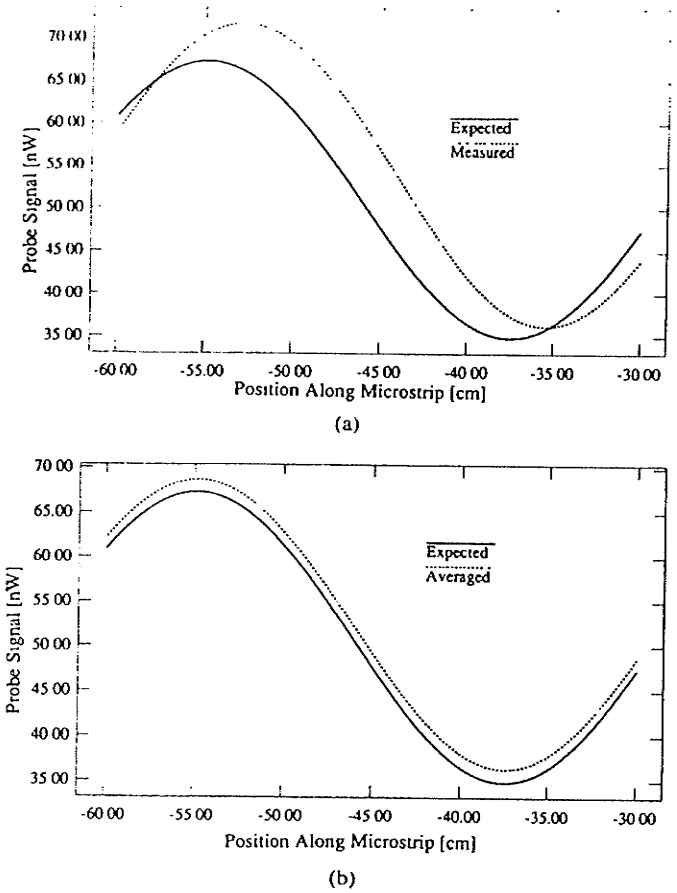

Figure 2-26 Comparison of the expected and measured standing wave along a microstrip having an SWR = 1.36 - a) not improved; b) improved by the probe-reversal technique [28]

The measurement results of the probe signal along the microstrip are shown in Figure 2-26 a) and b). The current maximum and minimum are cycled along the microstrip. The transverse patterns of an open-circuit microstrip taken at the current maximum and minimum points are shown in Figure 2-27 a) and b). These measurements were made at 280 MHz and the microstrip had a center conductor width of 5mm and a dielectric with ε_r

= 12 and thickness of 6.35 mm. The transverse pattern at a current minimum is quite different from that at the current maximum. This observation reveals that there is an unwanted contribution to the observed signal arising from electrostatic pickup. This contribution is usually small, but at a point on a transmission line corresponding to a current minimum of the probe output, the magnetic field is reduced and the electric field is increased, this causes the effect of the electrostatic to appear. However, the error from this source can be greatly removed through the expedient of making two measurements at the point of interest, between which the position of the probe is rotated around a vertical axis through 180°. By averaging these two measurements, the error caused by parasitic electric field coupling is greatly reduced (Figure 2-26 b)).

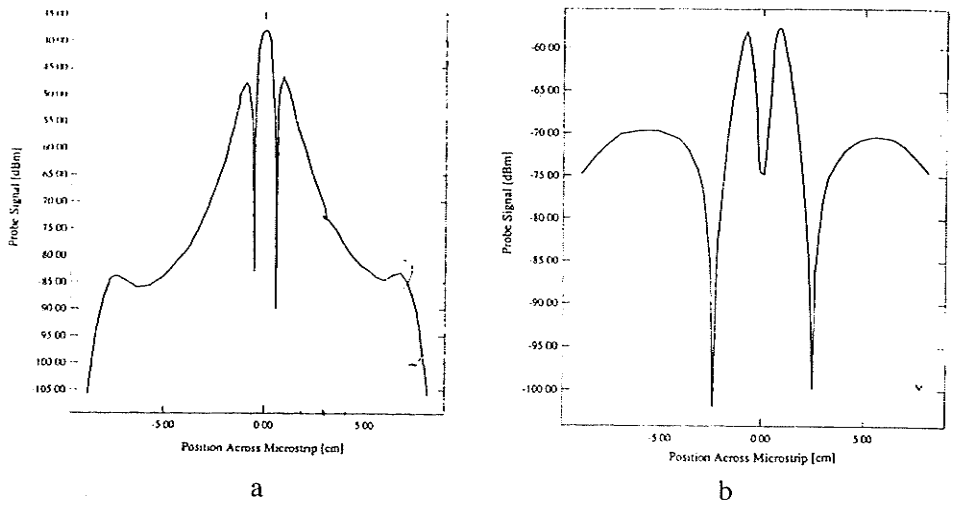

Figure 2-27 Transverse pattern of an open-circuited microstrip - a) taken at a current maximum; b) taken at a current minimum [28]

Due to the electric asymmetry problem in the double-loop magnetic probe, Grzybowski and Bansal [29] designed a half-loop magnetic field probe in which a 1 mil gold bond wire was connected to a Cascade Microtech WPH-102-250 wafer probe test head. Because the fabrication procedure is very complicated and additionally the wafer probe test head is expensive, it seems not to be suitable for practical applications. In the

work made by Y. Gao and I. Wolff [30] a single loop square magnetic field probe was designed (Figure 2-28). The square loop of the probe is 710 μm by 710 μm in size and its conductor width is 55 μm. It is an inexpensive one which also solves the electric asymmetry problem. But for both microstrip and CPW, the waveguides' magnetic field goes up and down through the same loop and their contributions cancelled. Furthermore, signals induced by a nearly uniform field coming from a distant source can't be avoided.

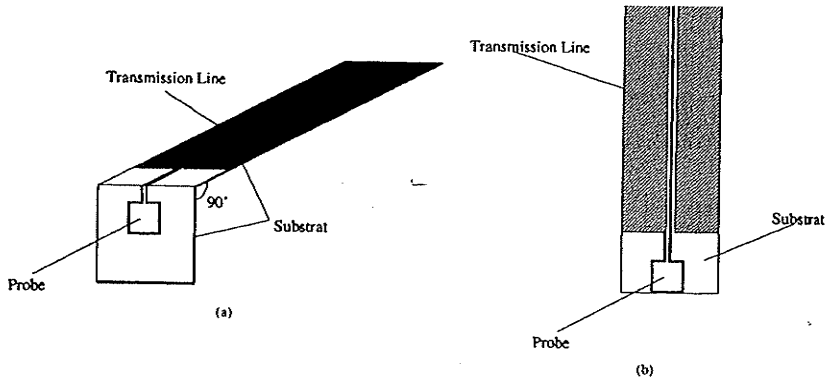

Figure 2-28 Single square loop magnetic probe - a) Probe for H_z magnetic measurement; b) Probe for H_x and H_y magnetic measurement [30]

The comparison of measured and calculated *Hz*- amplitude along and across the shorted microstrip is shown in Figure 2-29. The measurement was made at 20 GHz. We can see that the measured and calculated signals agreed well. But there is a notch in the amplitude curve of Hz- perpendicular to the shorted microstripline at the center point. The currents are cancelled while the magnetic field goes up and down through the same loop.

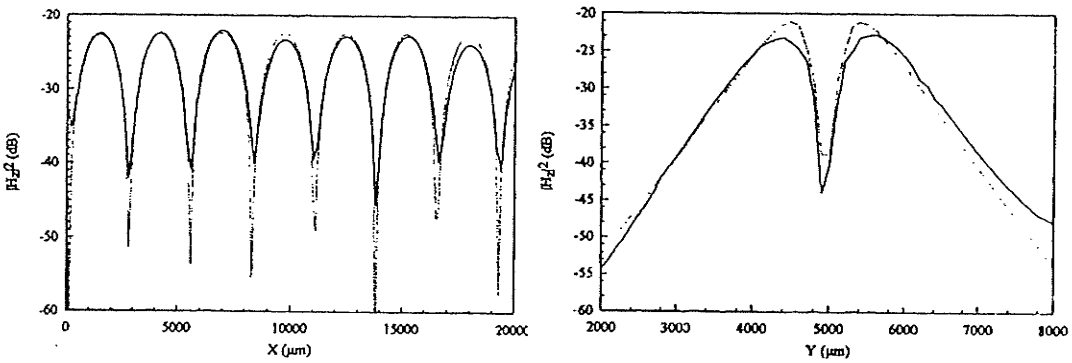

Figure 2-29 Comparison of measured and calculated squared-amplitude of H_z - a) along the microstrip; b) perpendicular to the microstrip at current maximum [30]

Magnetic field probe is a relatively simple device for circuit testing. The fabrication of reliable small scale probe for operation at high frequency is a major issue. One of the difficulties is in establishing good electrical contact between the loops and CPW feed which are right angled to each other. Another issue of uncertainty is the electrostatic coupling. If both of these problems solved, the magnetic probe could be a viable diagnostic tool.

2.2.3.2 Passive Electric-field Probe

As discussed in the above section, the passive magnetic-field probes appear to be incompatible to strong radiating circuits, e.g., antennas and circuits on substrates with small dielectric constant substrates. This made people come back to the eclectic-field probes. The early passive coaxial electric-field probe was designed in 1980 by J. S. Dahele [31] which used the central conductor of a coaxial cable to capacitively couple to a microsrtip under test. With the development of the microfabrication technology, the probe can be made smaller. A miniature probe designed by Y. Gao and I. Wolff [32] consists of a miniature coaxial line with 508 μm outer diameter and an inner conductor diameter of 112 μm. The inner conductor extends 300 μm beyond the outer conducting shield, as shown in Figure 2-30 a). Coaxial electric-field probe is usually used to measure

the electric field in the z-direction perpendicular to the substrate and is named EPZ, while the dipole electric field probe EPXY shown in Figure 2-30 b) is designed for tangential electric field measurement. The dipole electric field probe EPXY consists of an electric dipole and a coplanar transmission line with 50-Ω impedance.

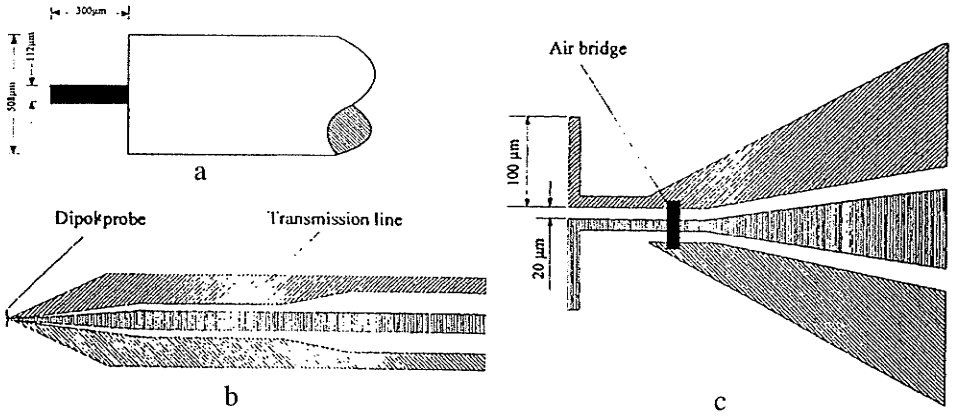

Figure 2-30 Electric field probes - a) EPZ; b) EPXY with transmission line; c) expended EPXY without transmission line [32]

Some measurement results using these electric field probes were discussed [32] . The measurement results of a bandpass filter with probe EPXY is shown in Figure 2-31. It is found when the probe enters the filter, the coupling effects between probe and the filter change the reflection of the filter (Figure 2-32). The S_{11} changes in the passband are about 7.0 dB. In order to improve the accuracy of the measurement, a smaller probe is needed or set the probe in a higher position, but both of them will reduce the sensitivity of the probe and further more the second solution will also reduces the resolution of the measurement.

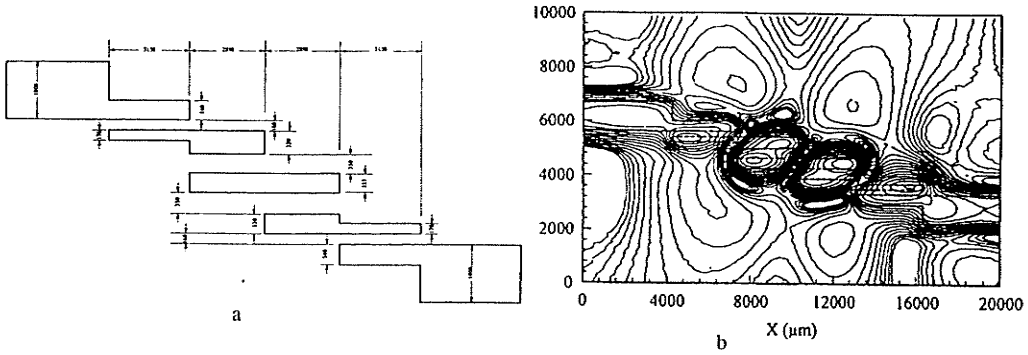

Figure 2-31 a) The layout of the bandpass filter, and b) 2-D representation of the measured squared field strength $|E_x|^2$ in the passband at 12.8GHz [32]

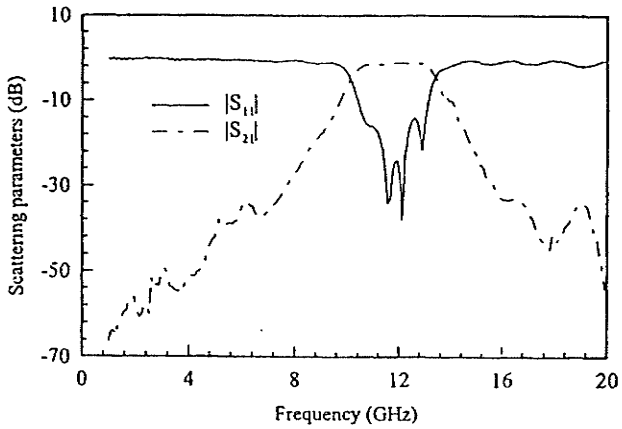

Figure 2-32 Measured scattering parameters for the bandpass filter [32]

Another factor that must be taken into account is the probes' influence to the DUT when the probes are positioned near the DUT since the measurement principle of the electric and magnetic near-field probes is to couple the electromagnetic near field of DUT to the probes. Further research work was done on EPZ probe (Figure 2-30 a)) to reveal a new calibration technique [33] for application of near-field probing. By using the finite-difference time-domain (FDTD) method, the probe shown in Figure 2-30 a) was theoretically analyzed to determine its most sensitive probe segment. Taking the

amplitude of the normal electric field at this segment as a known field, the probe is calibrated by defining a performance factor (PF), which is the ratio of the known field amplitude to the probe signal amplitude. PF, which is derived as a function of frequency, is shown in Figure 2-33. Using the fitting curve of the PF as a calibration curve, the measured and calculated normal electric-field distribution over a cross section of a microstrip line at 11.8 GHz is shown in Figure 2-34. Comparing the calculated results with measured results, the agreement is good.

With a calibrated probe, Y. Gao, etc estimated the coupling effect between the probes and the DUT, a microstrip line. The change of the scattering parameters S21 of the DUT was measured with an NWA during the movement of the field probe perpendicular to the line direction at a height of 50 μm above the microstrip line. It can be seen on Figure 2-35 that the influence of the probe on S21 is very small, about 0.05 dB. If the field probe is placed higher than 50 μm above the DUT, the influence of the probe is smaller and can be neglected.

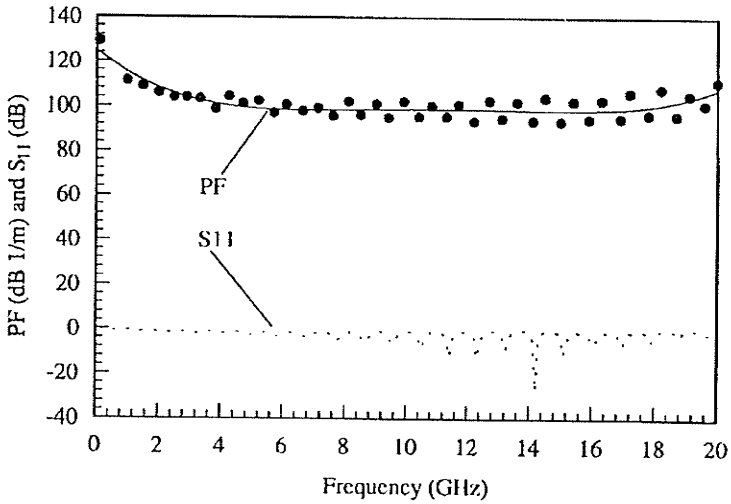

Figure 2-33 The PF and reflection coefficients S11 of the coaxial electric-field probe [33]

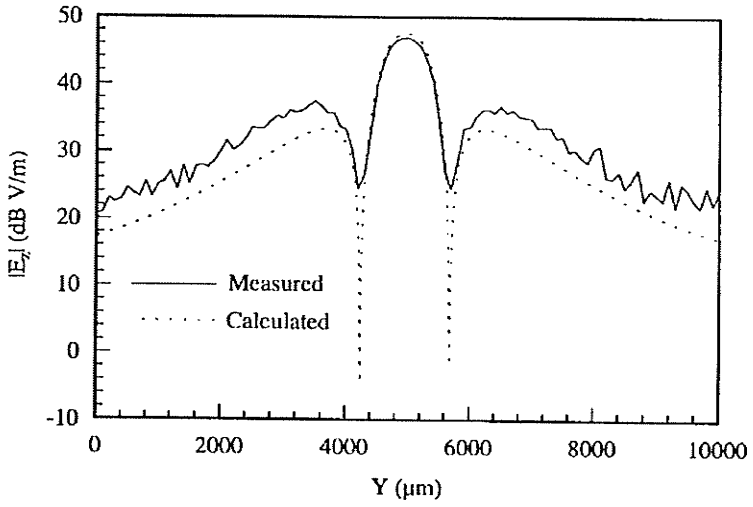

Figure 2-34 Comparison between the measured and calculated normal electric field at a cross section of the microstrip line at 11.8 GHz. (Substrate: $A_{l2}O_3$, $\varepsilon_r = 9.8$, h = 635 μm, w = 700 μm) [33]

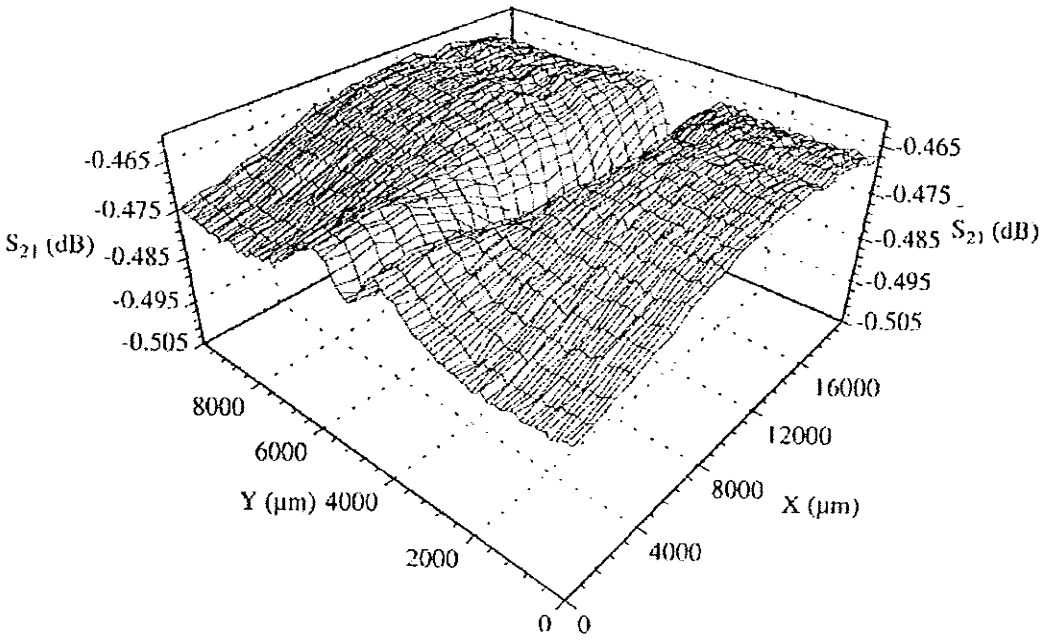

Figure 2-35 The investigation of the influence of the probe on the microstrip line [33]

Chapter 3 AUTOMATED NEAR-FIELD SCANNING SYSTEM

An automated measurement system is mandatory for investigating the feasibility of various electromagnetic near-field probing techniques. The hardware and software of the system must be flexible in order to facilitate testing on wide range of applications. Since experiments may require μm or mm scale resolution depending on circuit dimensions, there has to be two sets of hardware apparatus. The corresponding probe design and its characteristic dimensions must compliment the application. The software required must be user friendly and capable of driving commonly used measurement instruments, i.e. Network Analyzer, Spectrum Analyzer and Oscilloscope. This chapter will introduce the fundamentals of near-field scanning system and describe the hardware and software required for the system.

3.1 Fundamentals of the Scanning System

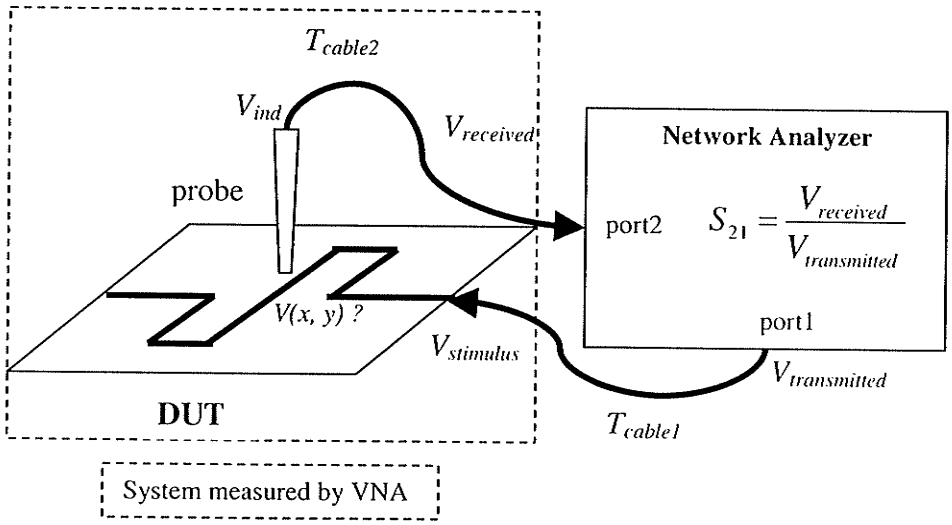

Figure 3-1 Diagram of Near-field Scanning System

Figure 3-1 shows the diagram of a near-field scanning system. To analyse the functionality and performance of a device under test (DUT), it is required to find the transfer function $T_{circuit}$ of DUT. As shown in Figure 3-1, given the circuit input signal $V_{stimulus}$, the $T_{circuit}$ can be calculated by sampling voltage signal $V(x, y)$ at test point (x, y).

$$V(x,y) = T_{circuit}(x,y) \cdot V_{stimulus} \tag{3-1}$$

The traditional contacting measurement methods have the probes directly touch on the surface of DUT to get the voltage signal $V(x, y)$ at each test point. The near-field probing concept is not intending to do a contacting measurement on the DUT. In contrast, by using a Network Analyzer to measure the S_{21} parameter of the system under test, as shown in Figure 3-1, it derives the transfer function of DUT from probing the electromagnetic field distribution above the surface of DUT. Equation (3-2) shows how the S_{21} parameter is measured.

$$S_{21}(measured) = \frac{V_{received}}{V_{transmitted}} = \left(20\log_{10} \frac{|V_{received}|}{|V_{transmitted}|} \right) \frac{\angle V_{received}}{\angle V_{transmitted}} \tag{3-2}$$

where $V_{transmitted}$ is the transmitted signal on port 1 of Network Analyzer, and $V_{received}$ is the signal received by Network Analyzer on port 2. Equation (3-3) shows the relationship between $V_{transmitted}$ and the input signal to DUT $V_{stimulus}$, whereas Equation (3-4) shows the relationship between $V_{received}$ and the induced signal picked up by probe V_{ind}.

$$V_{stimulus} = T_{cable1}(\omega) \cdot V_{transmitted} \tag{3-3}$$

$$V_{received} = T_{cable2}(\omega) \cdot V_{ind} \tag{3-4}$$

By substituting (3-3) and (3-4) into (3-2), S_{21} can be formulated as

$$S_{21}(measured) = \frac{V_{received}}{V_{transmitted}} = T_{cable2} \cdot V_{ind} \cdot \frac{T_{cable1}}{V_{stimulus}} \tag{3-5}$$

As it will be discussed in the following section, V_{ind}, the induced voltage signal by probe, can be formulated as

$$V_{ind} = T_{probe} \cdot V(x, y) \tag{3-6}$$

Substitute Equation (3-6) into (3-5),

$$S_{21}(measured) = T_{cable2} \cdot T_{cable1} \cdot T_{probe} \cdot \frac{V(x, y)}{V_{stimulus}} \tag{3-7}$$

Given Equation (3-1),

$$\begin{aligned} S_{21}(measured) &= T_{cable2} \cdot T_{cable1} \cdot T_{probe} \cdot \frac{T_{circuit}(x, y) \cdot V_{stimulus}}{V_{stimulus}} \\ &= T_{cable2} \cdot T_{cable1} \cdot T_{probe} \cdot T_{circuit}(x, y) \end{aligned} \tag{3-8}$$

The transfer function of DUT is then obtained from Equation (3-8),

$$T_{circuit}(x, y) = \cdot \frac{S_{21}(measured)}{T_{cable2} \cdot T_{cable1} \cdot T_{probe}} \tag{3-9}$$

In Equation (3-9), S_{21}, T_{cable1} and T_{cable2} can be obtained by measurement. It is expected to create a circuit model for the probe being used for near-field scanning. If the transfer function T_{probe} is derivable from modelling, the idea described above is then feasible. The following section will briefly discuss the monopole probe modelling.

3.2 Approximate Circuit Modelling of the Monopole Probe

In Equation (3-9), the transfer function of probe T_{probe} has to be found so that $T_{circuit}$ can be then calculated. Although an exact theoretical model is unavailable P.G. Frayne [37] [38] has developed a preliminary model to investigate the interaction between a monopole probe and an isolated conducting strip of finite width and infinite length.

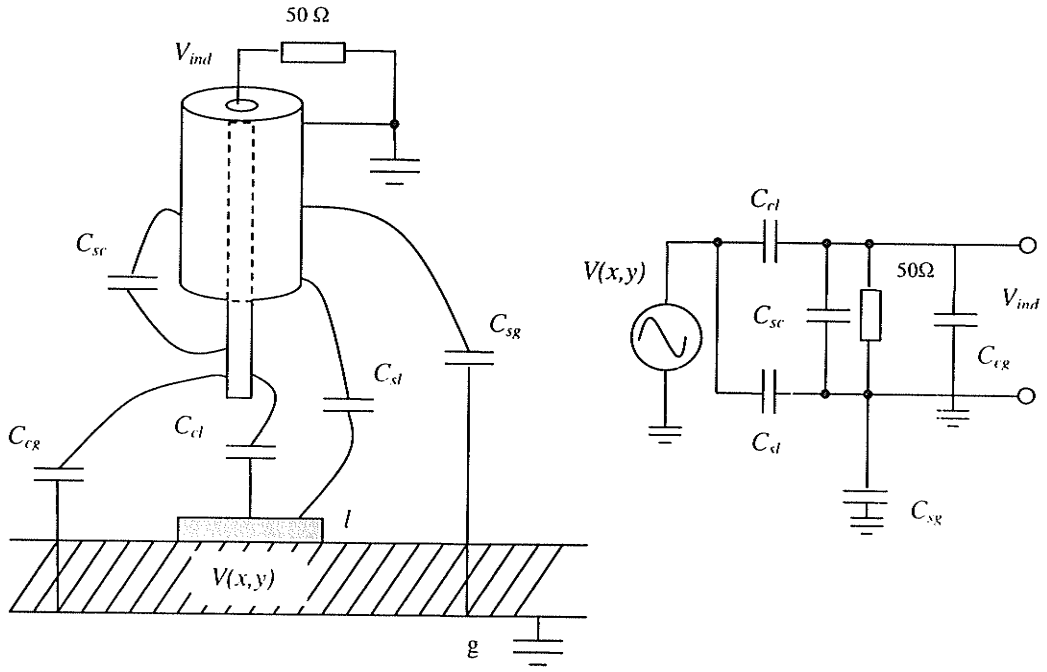

Figure 3-2 An approximate monopole probe model and the corresponding equivalent circuit model [5]

Figure 3-2 shows the model of monopole probe and an approximate equivalent circuit on the right hand side [5] . The model assumes that the probe load impedance is much greater than local circuit impedance. C_{cl} is the capacitance formed between conductor of probe and transmission line circuit, C_{sc} is the capacitance formed between probe conductor and shield, C_{sl} is the capacitance formed between shield of probe and

transmission line circuit, C_{cg} is the capacitance formed between probe conductor and ground plane, C_{sg} is the capacitance formed between probe shield and ground plane.

Given that probe shield is at ground, C_{sg} is large compared to C_{sl}, a simplified equivalent circuit can then be drawn as Figure 3-3.

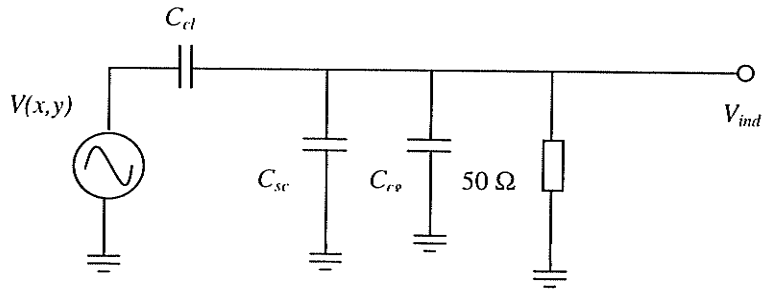

Figure 3-3 Simplified equivalent circuit for monopole probe assuming

$$V_{ind} = V(x,y)\cdot\frac{Z_0 \,//\, \dfrac{1}{j\omega(C_{sc}+C_{cg})}}{Z_0 \,//\, \dfrac{1}{j\omega(C_{sc}+C_{cg})} + \dfrac{1}{j\omega C_{cl}}} = V(x,y)\cdot\frac{j\omega C_{cl}Z_0}{1+Z_0 j\omega(C_{sc}+C_{cg})+j\omega C_{cl}Z_0} \tag{3-10}$$

for frequency where $1/j\omega(C_{sc}+C_{cg}) >> Z_0$, or $j\omega(C_{sc}+C_{cg})Z_0 << 1$

$$V_{ind} = V(x,y)\cdot\frac{j\omega C_{cl}Z_0}{1+j\omega C_{cl}Z_0} \tag{3-11}$$

Provided that $j\omega C_{cl}Z_0 << 1$

$$V_{ind} \cong j\omega C_{cl}Z_0 V(x,y) \tag{3-12}$$

From Equation (3-6) and (3-11), T_{probe} can then be express as

$$T_{probe} \cong j\omega C_{cl} Z_0 \tag{3-13}$$

By using a method of moment (MOM) solution, the coupling capacitance C_{cl} can be calculated. With the potential specified as 1 Volt, T. Forzley gave a plot of C_{cl} for various heights h of the probe above the transmission line and incremental displacements relative to the center of the transmission line [5] . As shown in Figure 3-4, for example, C_{cl} is on the order of 5 fF for a 1/16″ OD and tip length of 0.5 mm probe at a height of 0.5 mm above the transmission line.

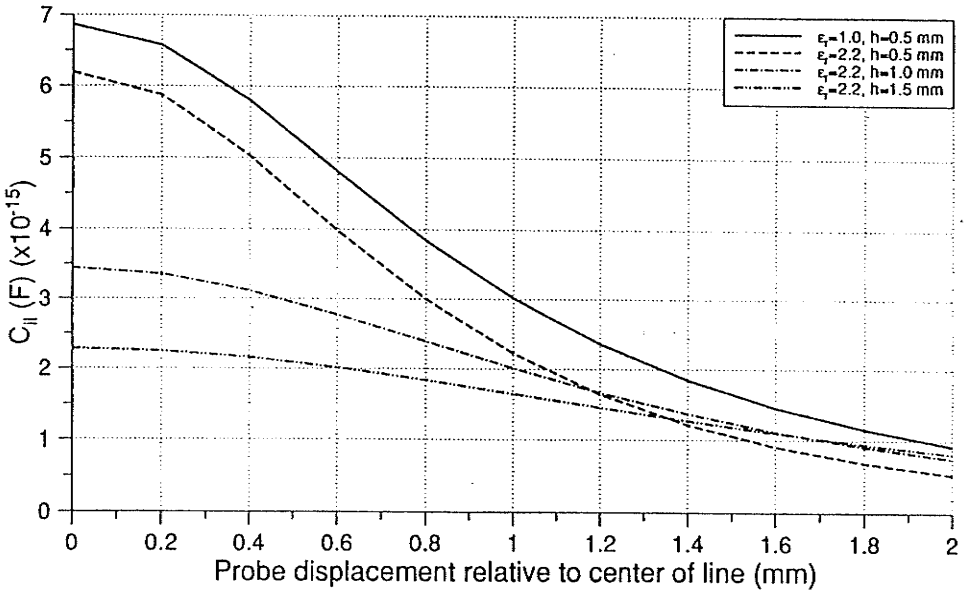

Figure 3-4 Calculation of the critical coupling capacitance C_{cl} (C_{il}) [5]

Some fundamental properties of the monopole probe have been discussed [37] [38] [5] . Firstly, the spatial resolution of the probe is not purely a factor of the coax outer diameter. Instead, the operating frequency and standing wave ratio on the structure must also be considered.

Secondly, the sensitivity of the probe is directly proportional to the tip length t. As t increases so does the number of electric field lines terminating on the center conductor, hence a greater potential difference between the conductors is induced. On the other hand, the resolution as a function of tip length is difficult to calculate and cannot be readily quantified. The most tactical approach to quantify the resolution would be to incorporate both an experimental and theoretical analysis on probes of various sizes and tip lengths.

Finally, the net probe response is due to both capacitive and magnetic coupling. The magnetic field coupling is due to the transverse magnetic field component which is proportional to the axial current density. Ideally, the monopole probe should respond only to electric field coupling, hence it is the natural dual of the loop probe. In contrast, while the monopole probe measurement error arises from magnetic field coupling, the error in the loop probe measurement is due to electric field coupling.

The usable bandwidth of the monopole probe is a function of its dimensions. Both the tip length and outer diameter must be a small fraction of the wavelength in the medium being measured. This restriction is necessary to avoid any spurious radiation by the probe. The measurement error incurred as a result of undesirable magnetic field coupling is another limitation.

3.3 Scanning System Hardware Description

The measurement system shown in Figure 3-5 consists of an HP8753E Network Analyser (for up to 6 GHz measurement) or a Wiltron 360 Network Analyzer (for up to 40 GHz measurement), a host PC, and a two-axis positioning stage. The computer acts as the central controller which manipulates the positioning state by RS-232 serial link, conducts the Network Analyzer operation and subsequent data acquisition via General Purpose Interface Bus (GPIB or also commonly known as the IEEE- 488 standard).

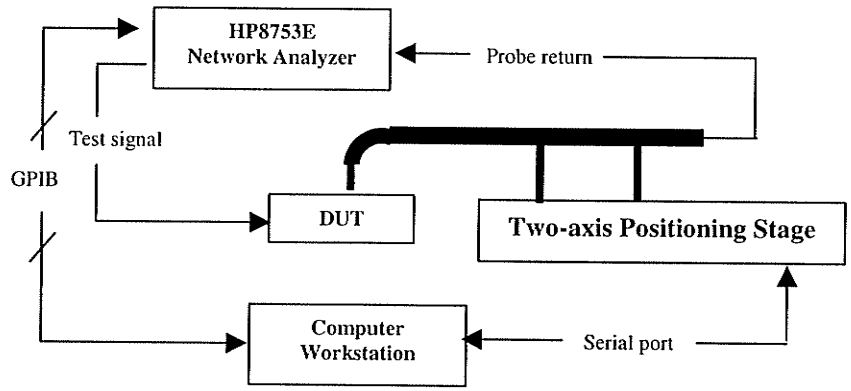

Figure 3-5 Measurement system hardware

Two different positioning stages were developed for targeting on different applications where the DUT areas are varying and different resolutions are demanded. For applications requiring mm or sub-mm sampling intervals, an HP7220C plotter has been proven to be reliable and versatile. The scan area of the plotter is limited by the design of the probe support. Currently scans on the order of 15 cm by 28.5 cm with a minimum step resolution of 25 μm. For probing on tiny scale circuit, such as MMIC on-wafer testing, where μm to sub-μm resolution is required, a DC motor driven table was alternatively used. Two limitations of using DC motors are backlash and speed. If the backlash of each motor is known it can be compensated for in software. The minimum step size of the motors being currently used is 0.1 μm for each axis capable of 25 mm of displacement.

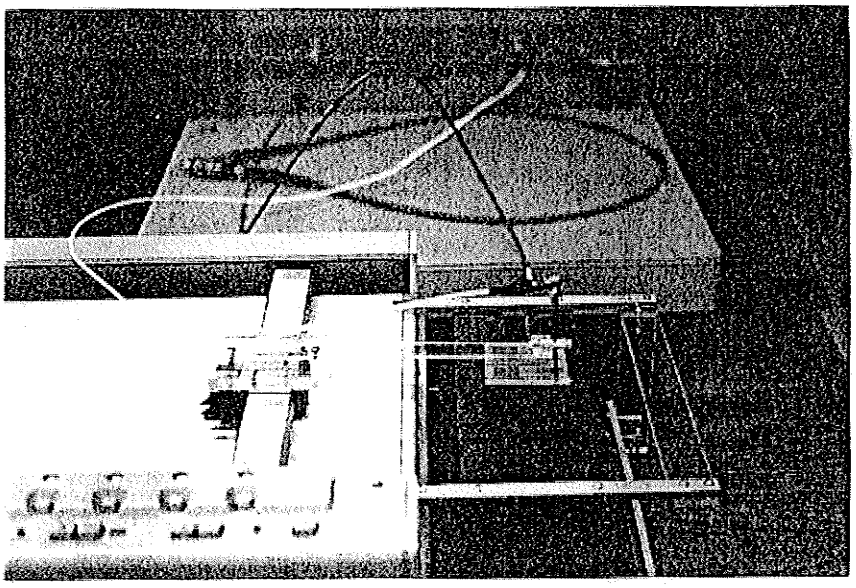

Figure 3-6 Plotter mounted with monopole probe for mm resolution scans

Figure 3-6 shows the test platform for mm level measurement of microwave devices. The probe is mounted on the plotter which is controlled by a computer. The scanning resolution of the plotter is of 25 μm.

Figure 3-7 shows the apparatus required for μm resolution scans. The monopole probe is mounted on a plastic beam that is fixed on the DC motor driven table. When using the monopole probes whose dimensions inhibit direct connection to a SMA connector some ingenuity is required. A miniature coax (D_o = 0.32 mm and D_i = 0.05 mm) is soldered directly to a large coax (D_o = 2.2 mm and D_i = 0.51 mm) which in turn directly mates with a SMA connector. For slightly large coax it is possible to use an intermediary microstrip transmission line to construct a coax-microstrip-SMA configuration. To investigate the effects of the discontinuities introduced to the transmission line, time domain measurements can be performed.

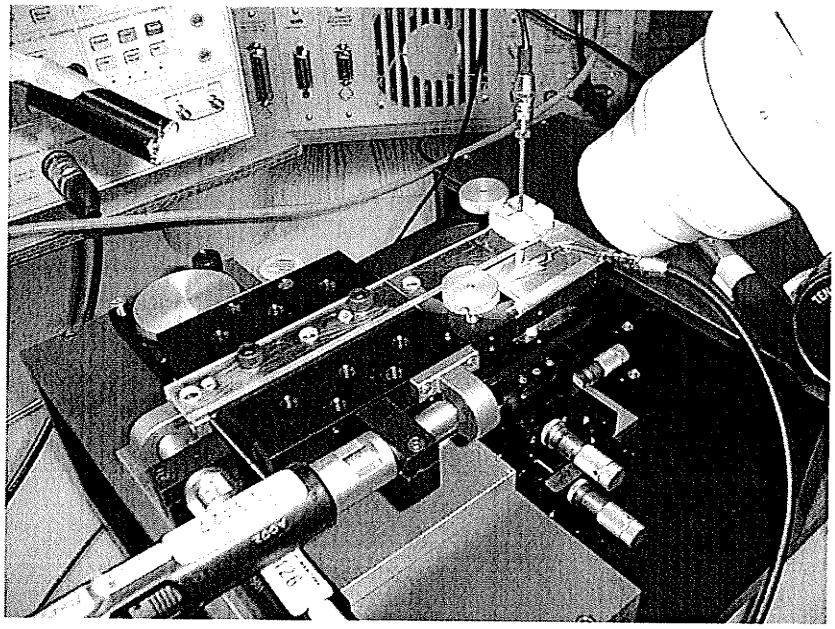

Figure 3-7 Close up of DC motor test station used to scan μm circuits

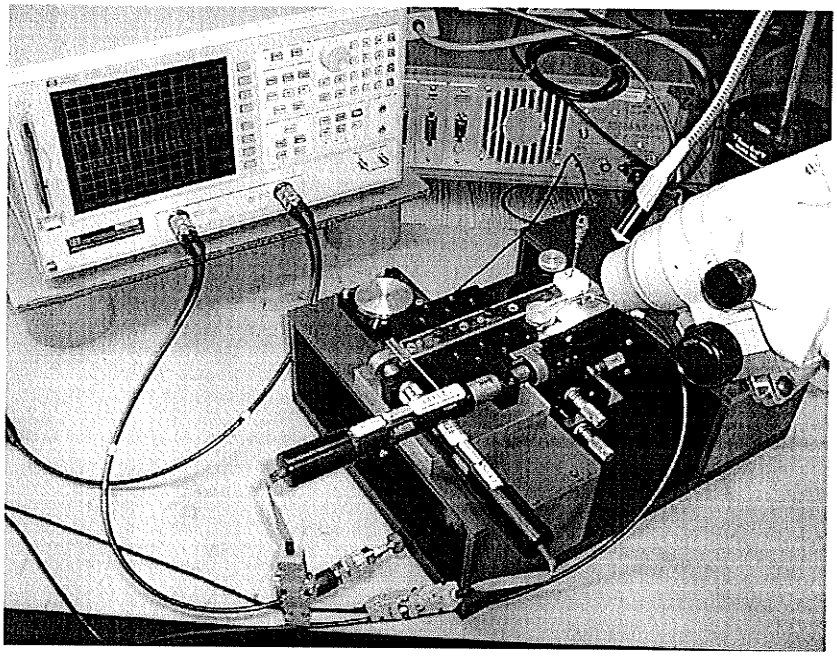

Figure 3-8 Setup of the Scanning System for μm level measurement

Figure 3-8 shows the whole setup for the computer controlled scanning system. The DC motors is connected to the computer via a 9-pin serial port. The Network Analyser is communicated with the computer through GPIB using an IEEE-488 cable. The test signal from the Network Analyser is the input to the device under test, the feed back signal from the probe is returned to the Network Analyser. The computer controls the movement of the DC motors and the operation of the Network Analyzer, collects, processes and displays the measurement data by the software programmed using LabVIEW.

3.4 Software Development with LabVIEW™

3.4.1 Introduction of LabVIEW

The introduction of LabVIEW pioneered a new instrumentation approach called virtual instrumentation. Virtual instrumentation empowers users to build their own instrumentation systems with standard computers and cost-effective hardware. These software-centered systems leverage off the computational, display and connectivity capabilities of popular computers to give users the power and flexibility to build each of your instrumentation functions.

LabVIEW is a revolutionary graphical programming development environment based on the G programming language for data acquisition and control, data analysis, and data presentation. LabVIEW features with the flexibility of a powerful programming language without the associated difficulty and complexity because its graphical programming methodology is inherently intuitive to scientists and engineers.

LabVIEW is a multi-platform, available for Windows 9x/NT/2000/, Mac OS, Sun, HP-UX, and Concurrent PowerMAX. Data can be acquired from thousands devices, including GPIB, VXI, PXI, serial devices, PLCs, and plug-in data acquisition (DAQ) boards. By using the LabVIEW inter-application communication tools such as ActiveX, dynamic data exchange (DDE), and structured query language (SQL) database links,

remote data sources can be accessed via Internet. LabVIEW program can be called from other environments. It can also call existing code in the form of a dynamic linked library (DLL) on windows or a shared library on other Operating Systems.

Users can easily find and download almost all the drivers of measurement equipment, such as oscilloscope, logic analyzer, network analyzer, spectrum analyzer, etc. in their labs from either equipment makers or National Instruments, even from some other users who have developed the drivers for the instruments. It empowers users a faster way to program instrumentation, data acquisition and control system, to build their own solutions for scientific and engineering systems. It gives the flexibility and performance of a powerful programming language without the associated difficulty and complexity. This will significantly reduce the time to develop a measurement system, and make users focused on their measurement itself instead of system development.

G programming language is the heart of the LabVIEW. Like C or BASIC, G is a general purpose programming language with extensive libraries of functions for any programming task. G also includes conventional programming debugging tool, user can set breakpoints, animate the execution to see how data passes through the program. G programs are called virtual instruments (VIs) because their appearance and operation can imitate actual instruments. A VI consists of an interactive user interface, a dataflow diagram that severs as the source code, and icon connections that set up the VI so that it can be called from higher level VIs.

The interactive user interface of a VI is called the front panel, because it simulates the panel of a physical instrument. The front panel can contain knobs, pushbuttons, graphs, and other controls and indicators. Users enter data using a mouse and keyboard, and view the results on the computer screen.

The VI receives instructions from a block diagram, which user constructs in G. The block diagram is a pictorial solution to a programming problem. The block diagram is also the source code of the VIs.

VIs are hierarchical and modular. User can use them as either top-level programs or subprograms. The icon and connectors of a VI work like a graphical parameter list so that data can be passed between VIs.

With these features, G makes the best use of the conception of the modular programming. Each subVI can be performed and debugged by itself, this makes programming much easier.

3.4.2 The LabVIEW™ Test Program for Computer Controlled Scanning System

A series of LabVIEW programs have been developed for controlling probe manoeuvring and data acquisition. The programs are the third generation of the automated scanning system software which is improved over the second generation [5] . It provides the way to easily integrate all hardware controlling involved in the measurement into a single graphic user interface, i.e. network analyzer, DC motor, plotter, spectrum analyzer, etc. The 2nd generation software EMDAP (ElectroMagnetic Data Acquisition Program) was developed based on the Turbo Pascal and provided the control of the scanning system by the command line interface on DOS Operating System. The current software is designed with a graphical user-interface which makes full use of the control components in the LabVIEW control palette (Figure 3-9).

Through GPIB (IEEE 488) interface, communication between the computer and the Network Analyser is established. All the features of the Network Analyser can be remotely accessed by the LabVIEW program in the Network Analyser Setup control box. The test frequency can be specified as the centre frequency and the scanning span and the data format can be log/linear magnitude, phase, smith chart, polar and standing wave

ratio. User can also select the measurement of S-parameters, R-parameters or A/B parameters. Via the COM1/COM2 serial port, the DC Motor or plotter can be controlled for μm or mm resolution scanning, respectively. In the DC Motor/plotter Control box, user can define start point, end point and scanning step.

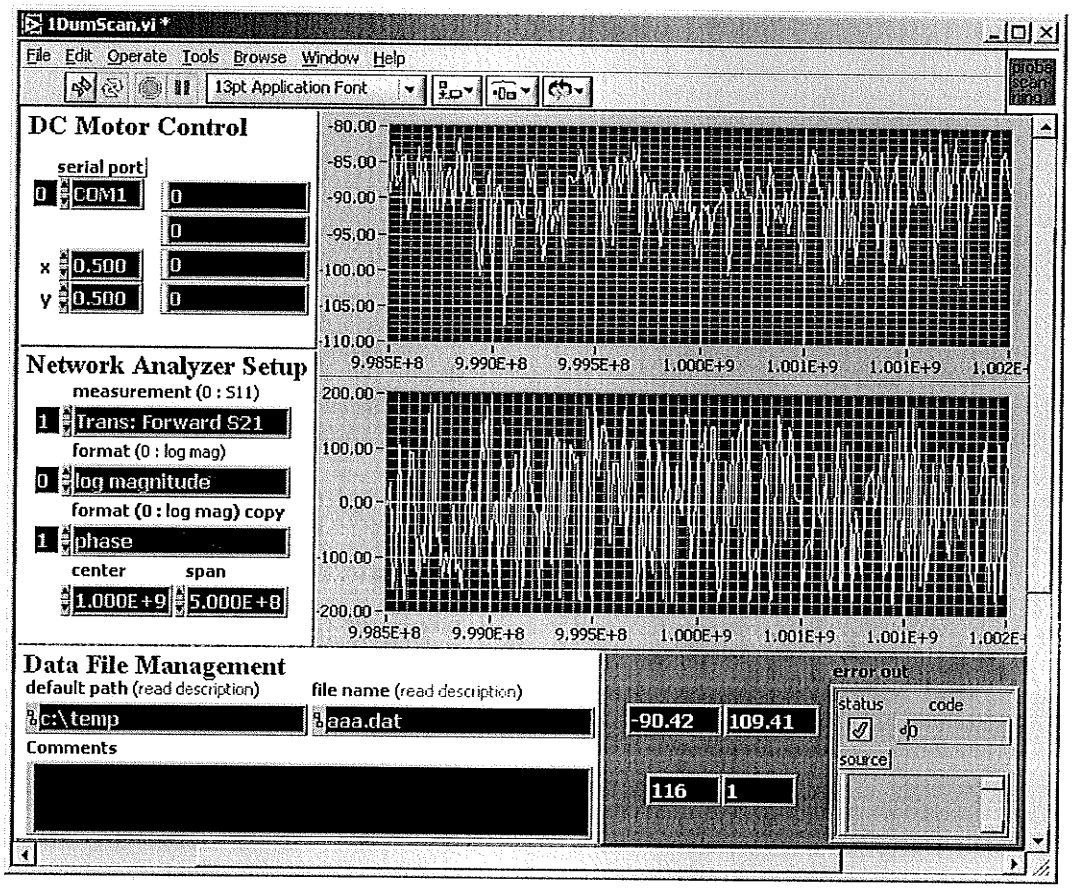

Figure 3-9 Frontpanel of the LabVIEW test program for Computer Controlled Scanning System

A real-time display of the spectrum magnitude and phase along with the automatic data filing is also provided in the LabVIEW program. A summary and comparison of the capabilities between the two generations of software is provided in Table 3-1 Summary and comparison of the two generation of software.

Table 3-1 Summary and comparison of the two generation of software

	Communication	Scans	Real time display	Resolution	Control	
Program	GPIB & COM	1D & 2D	Magnitude & phase	mm & μm	Command line	Graphical user interface
EMDAP	Yes	Yes	No	Yes	Yes	No
LabVIEW: 1DumScan.vi 2DumScan.vi 2DmmScan.vi	Yes	Yes	Yes	Yes	No	Yes

Chapter 4 NEAR-FIELD SCAN USING MONOPOLE AND COPLANAR WAVEGUIDE PROBES

To further expand on previous measurements [5] , more experiments were conducted to illustrate the value of the monopole coaxial probes as microwave circuit diagnostic tools. Tests on applications ranging from coplanar waveguide transmission lines, single patch microstrip antenna to microstrip antenna arrays have been done. As an alternative, the Coplanar Waver Guide (CPW) probes are also fabricated and tested. Some results comparing monopole probe with CPW probe is presented. Depending on the application the sampling interval may be in the mm to μm range. Typically, 50 to 100 field data samples per observation point are taken to minimize the noise effect to the measurement results.

4.1 Monopole Probes to Measure 50Ω CPW T- Line

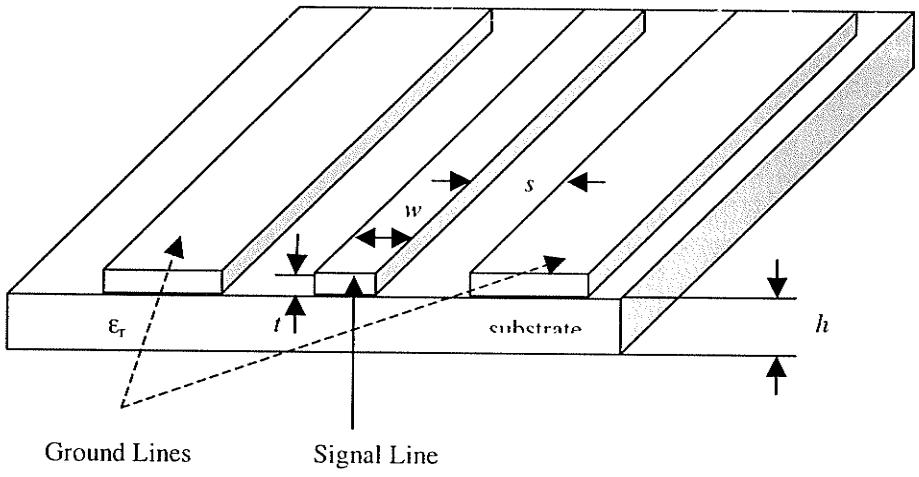

Figure 4-1 Structural diagram of a coplanar waveguide T-line

The use of coplanar waveguides (CPW) in microwave integrated circuits is very popular since it adds flexibility and improves the performance of some circuit functions at high frequencies. The CPW architecture allows for the mounting of lumped components in a shunt or series configuration, while eliminating the need for drilling holes or slots through the substrate. Figure 4-1 shows the structure of a coplanar waveguide transmission line circuit, where w is the width of the signal line, t is the thickness of the signal line, h is the substrate thickness. ε_r is the relative dielectric constant of the substrate, and ε_{eff} is the effective dielectric constant of the substrate.

4.1.1 Coplanar Waveguide Transmission Line Analysis

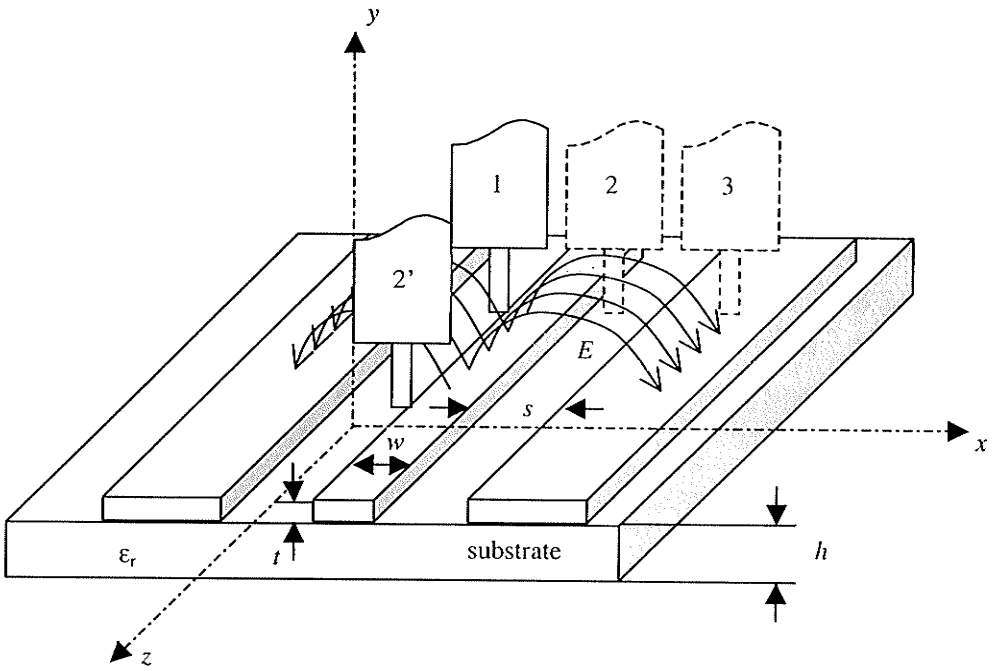

Figure 4-2 Electric field variation above CPW T-line and measurement with monopole probe

Figure 4-2 is a diagram that illustrates the electric field variation over the surface of CPW T-line. It also shows the monopole probe displacement at different spot when it is

scanning transverse (x direction, position 1, 2, and 3) and longitudinal scanning (z direction, position 1 and 2') over the CPW transmission line.

When it is in TEM mode the distribution of electric field over the surface of CPW transmission line can be summarized as

$$\overline{E}(x, y, z) \sim \overline{E}_T(x, y)e^{\pm \gamma z} \tag{4-1}$$

where E_T only has x and y components and the z-variation is of exponential form. So E_T should have same pattern at any given z expect for a phase and magnitude change. The electric field distribution over CPW T-line then can be discussed separately.

Two different CPW T-lines were scanned with monopole and CPW probes. Their geometries and parameters are shown in Figure 4-3 and Table 4-1 respectively. The two transmission lines will be referred as Type A and Type B transmission lines in the following measurement.

Table 4-1 Parameters of two tested CPW transmission lines (Figure 4-1)

	Type A	Type B
Z_0 (Ω)	68.9 *	49.2
ε_r	2.54	9.8
s (μm)	330	100
w (μm)	740	250
h (μm)	580	280
t (μm)	17	5
ε_{eff}	1.87	4.97

*It is noted that Z_0 of type A CPW calculated by PCAAD was not close to 50 Ω as expected. This is probably due to the change to the substrate property in the etching process. The Type A CPW is not a commercial but a house-made product.

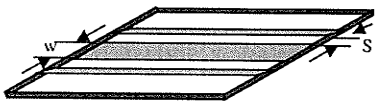

Type A: s = 0.3 mm w = 0.7 mm
Type B: s = 0.1 mm w = 0.25 mm

(a)

(b)

Figure 4-3 a) Structural diagram of CPW T-line; b) Type B CPW under test, s = 100 μm and w = 250 μm

4.1.1.1 Analysis of Transverse Electric Field Variation

An important property of TEM wave on transmission line is that the electric field can be uniquely related to the voltage on the transmission line. If the electric field $\overline{E}_T(x, y)$ due to the transmission line is known, an approximation to the induced voltage on the probe is

$$V_{ind} \approx \int_{path} \overline{E}_T(x, y)\, dl \xrightarrow[L_{Tip} \text{ is very small}]{} L_{tip} E_{Ty}(x_{tip}, y_{tip}) \qquad (4\text{-}2)$$

where L_{tip} is the probe tip length, E_{Ty} is the y component of electric field at the tip location (x_{tip}, y_{tip}).

As shown in Figure 4-2, when the monopole probe is right over the signal line of CPW transmission line at position 1, the electric field $\overline{E}_T(x, y)$ only has y component, the coupling voltage between the probe tip and the CPW circuit V_{pc} will then be maximum in magnitude. With the probe moving to the right, $\overline{E}_T(x, y)$ will have both x and y components till the probe moves to position 2, where the probe is right above the

gap between signal line and ground line of CPW, $\overline{E}_T(x, y)$ has now only x component and V_{pc} will then be zero. Again, $\overline{E}_T(x, y)$ at position 3 only has y component with an inversed phase, so V_{pc} will be seen at its second peak in magnitude.

To solve for $\overline{E}_T(x, y)$, we solve the Laplace Boundary Value problem for $\Phi(x, y)$, and then use $\Phi(x, y)$ to determine $\overline{E}_T(x, y)$ since $\overline{E}_T(x, y) = -\nabla\Phi(x, y)$. In order to estimate V_{ind} for a particular CPW geometry, under electrostatic conditions we can solve the Laplace Equation for that geometry to yield $\overline{E}_T(x, y)$ and then V_{ind}.

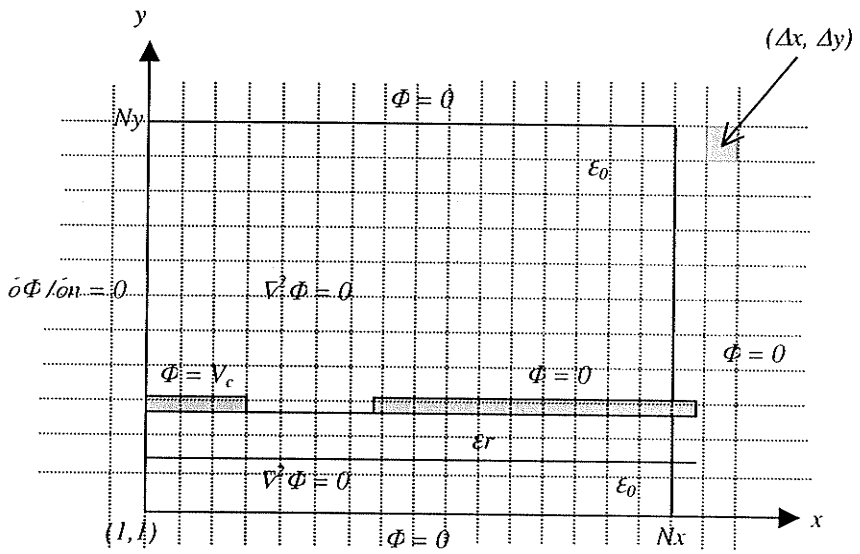

Figure 4-4 Laplace Boundary Value problem solving

We solve the Laplace BV problem numerically, as shown in Figure 4-4, using a finite difference MOM approach with an SOR Iterative Matrix Solver [40] . We set

- $\Delta x = 25$ μm, $\Delta y = 25$ μm and $Nx = 101$ and $Ny = 121$ to solve Laplace BV problem for Type A CPW, and

- Δx = 10 μm, Δy = 10 μm and Nx = 101 and Ny = 111 to solve Laplace BV problem for Type B CPW, and

Figure 4-5 is the plot of electric potential $\Phi(x, y)$ on x-y plane (refer to Figure 4-2 and Figure 4-4) by solving the Laplace BV problem. Given the contour plot of $\Phi(x, y)$, the electric field $\overline{E}_T(x, y)$ will then be drawn since it is normal to $\Phi(x, y)$.

Figure 4-6 is the plot that shows the Laplace BV problem solution for y component of the electric field $E_y(x, y)$ at different height above the Type B CPW transmission line circuit plane.

Figure 4-7 and Figure 4-8 demonstrate the solutions for Type A and Type B CPW T-line laplace problem using the SOR iteration algorithm, and they will be compared with the experimental results on Type A and Type B CPWs later in section 4.1 and 4.4. Figure 4-7 shows the results on Type A CPW with different probe tip length at a certain height over the circuit. Figure 4-8 shows the results on Type B CPW with probe at different heights over the circuit. Since a CPW probe will be used to measure the Type B CPW circuit in the later experiment, we choose the height at 0.5w, w and 2w, where w = 120 μm is the signal line width of the CPW probe.

To confirm that the convergence of FD method is not changing with the grid size $\Delta x \Delta y$, the calculation was repeated by using different values of Δx and Δy, namely Δx = *10 um* and Δy = *10 um* to calculate for the Type A CPW and Δx = *5 um* and Δy = *5 um* to calculate for the Type B CPW. The same results were obtained for each case.

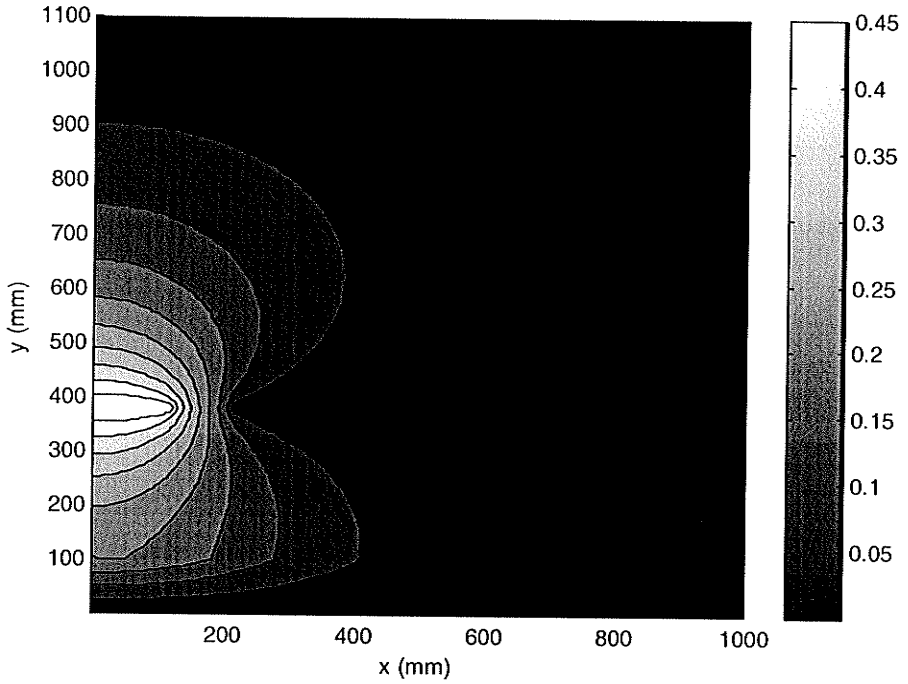

Figure 4-5 Contour plot of electric potential $\Phi(x, y)$ of Type A CPW provided that 5V applied to the CPW signal line

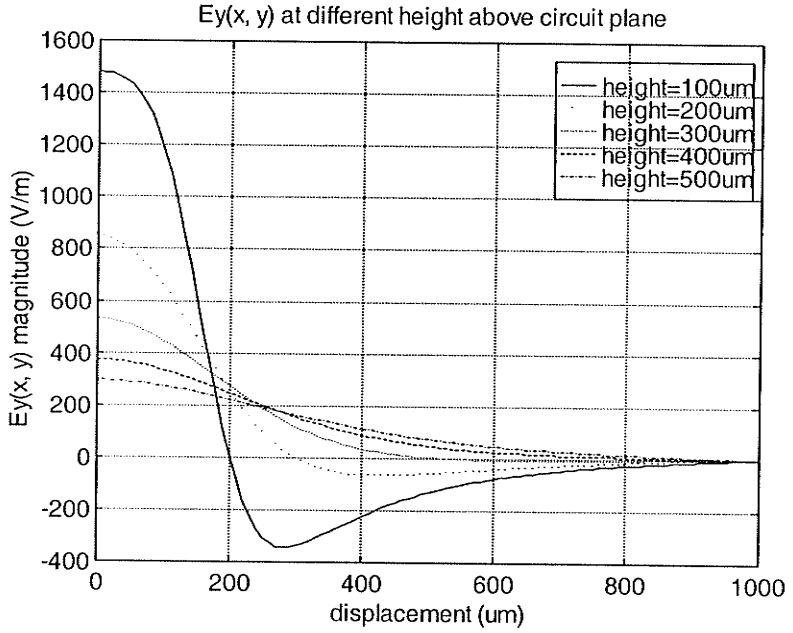

Figure 4-6 $E_y(x, y)$ at different height above Type B CPW circuit plane

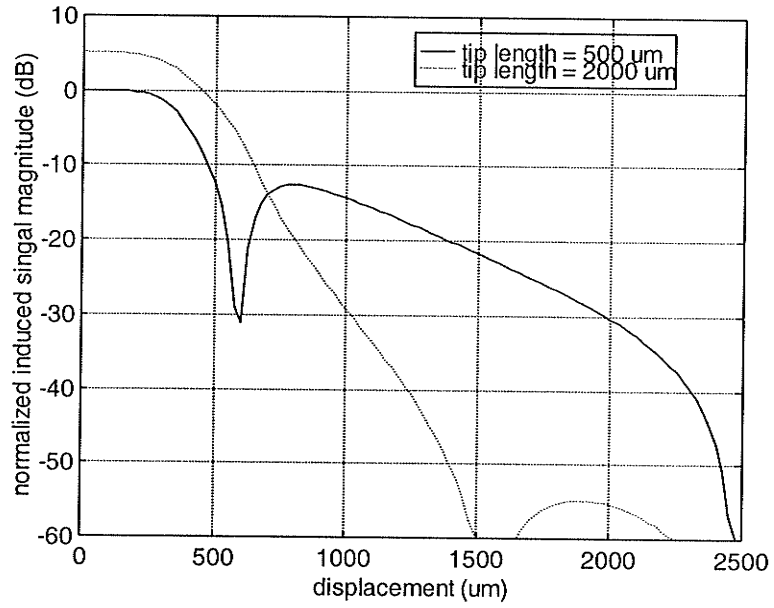

Figure 4-7 Laplace BV problem solution for Type A CPW provided that different monopole probes at same height of 100 μm over the circuit plane

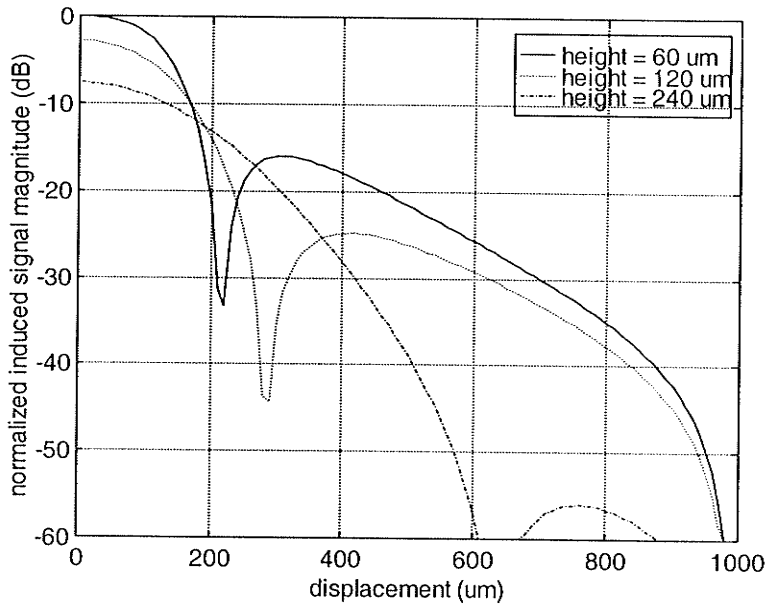

Figure 4-8 Laplace BV problem solution for Type B CPW provided that a CPW probe with tip length of 180 μm at different heights over the circuit plane

4.1.1.2 Analysis of Longitudinal Electric Field Variation

To investigate the longitudinal variation of the electric field, we can analyze the structures using circuit theory concepts, provided we break the problem into small parts so that the circuit element dimensions will be much smaller than a wavelength. To do this, we describe the transmission-line by a series resistance per unit length R, series inductance per unit length L, shunt conductance per unit length G, and shunt capacitance per unit length C. A small section of transmission-line with length dz thus has the following equivalent circuit:

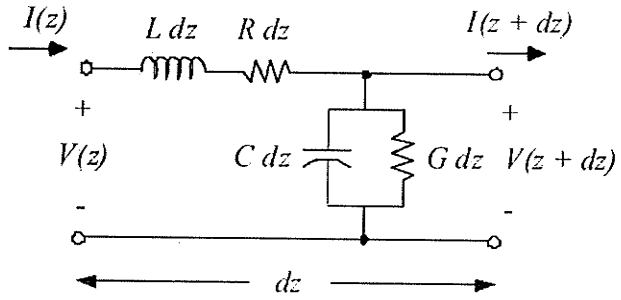

Figure 4-9 Equivalent circuit of a section of transmission line

Analysis of this circuit for time-harmonic signals gives the wave equations

$$\frac{\partial V(z)}{\partial z} - \gamma^2 V(z) = 0 \qquad \frac{\partial I(z)}{\partial z} - \gamma^2 I(z) = 0 \tag{4-3}$$

where γ is the complex propagation constant given by

$$\gamma = \alpha + j\beta = \sqrt{(R + j\omega L)(G + j\omega C)} \tag{4-4}$$

Given a lossless transmission line, $\alpha = 0$, and

$$\gamma = j\beta \tag{4-5}$$

The solutions to the wave equations are superpositions of forward and reverse waves,

$$V(z) = V_o^+ e^{-\gamma z} + V_o^- e^{\gamma z} \qquad I(z) = I_o^+ e^{-\gamma z} + I_o^- e^{\gamma z} \tag{4-6}$$

Just like with plane waves, we define a characteristic impedance as the ratio of voltage to current (for positive travelling waves)

$$Z_o = \frac{V_o^+}{I_o^+} = -\frac{V_o^-}{I_o^-} \tag{4-7}$$

and the wave velocity (or phase velocity) and wavelength are given by

$$\lambda_g = \frac{2\pi}{\beta} \qquad v_p = \frac{\omega}{\beta} = f\lambda_g \tag{4-8}$$

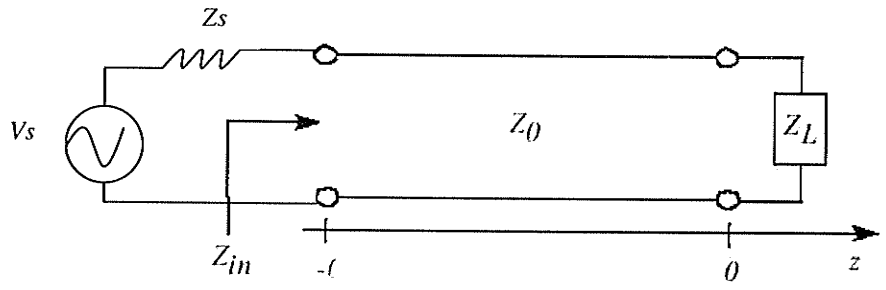

Figure 4-10 Schematic model of a generally loaded transmission line

For the transmission-line circuit above (Figure 4-10), we define a voltage reflection coefficient (at the load Z_L) as the ratio of reflected voltage to incident voltage, which can in general be complex:

$$\Gamma_L = \frac{V_o^-}{V_o^+} = |\Gamma_L| e^{j\theta\Gamma} = \frac{Z_L - Z_o}{Z_L + Z_o} \qquad (4\text{-}9)$$

Some special cases are:

Short: $Z_L = 0 \rightarrow \Gamma_L = -1$ Open: $Z_L = \infty \rightarrow \Gamma_L = +1$ Match: $Z_L = Z_0 \rightarrow \Gamma_L = 0$

Using the load reflection coefficient gives the input impedance Z_{in} for the lossless case

$$Z_{in} = Z_0 \frac{Z_L + jZ_o \tan \beta l}{Z_o + jZ_L \tan \beta l} \qquad (4\text{-}10)$$

The term βl is called the electrical length of the transmission-line. Some special cases for Z_{in} are considered with different load Z_L:

Short line: $Z_L = 0$ $Z_{in} = jZ_o \tan \beta l = jZ_o \tan \frac{2\pi}{\lambda g} l$ (4-11)

Open circuit: $Z_L = \infty$ $Z_{in} = -jZ_o \cot \beta l = -jZ_o \cot \frac{2\pi}{\lambda g} l$ (4-12)

Given Equation (4-6) and (4-9), $V(z)$ can be produced,

$$V(z) = V_0^+ [1 + \Gamma_L e^{2\gamma z}] e^{-\gamma z} \qquad (4\text{-}13)$$

where V_0^+ is determined by the source V_s (Figure 4-10) and its impedance. For a lossless transmission line,

$$V(z) = V_0^+ [1 + \Gamma_L e^{j2\beta z}] e^{-j\beta z} \qquad (4\text{-}14)$$

What are interested in is *V(z)* for different load conditions.

For a matched load, $Z_L = Z_0$ and $\Gamma_L = 0$, there is a linear phase variation with position

$$V(z) = V_0^+ e^{-j\beta z} \tag{4-15}$$

For an OC (open circuit) load, $Z_L = \infty$ and $\Gamma_L = +1$,

$$\begin{aligned} V(z) &= V_0^+ [1 + e^{j2\beta z}] e^{-j\beta z} \\ &= 2V_0^+ \cos(\frac{2\pi}{\lambda_g} z) \end{aligned} \tag{4-16}$$

Hence, there is a standing wave with minima at $\lambda_g/2$ spacing. Along the transmission line, as shown in Figure 4-10, *V(z)* has a minimum in magnitude at each test point where $z = n\lambda_g/4$, n = -1, -3, -5, ..., where $\lambda_g = c/f\sqrt{\varepsilon_{eff}}$.

4.1.2 50 Ω CPW T- Line Measurement with Monopole Probes of Different Tip Lengths

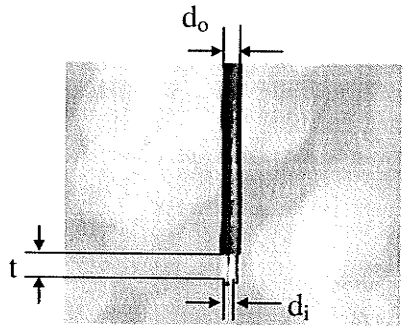

Coaxial Probe
t=0.5mm/2mm
do=0.32mm
di=0.05mm

Figure 4-11 Monopole probe

Coaxial probe is the simplest and easiest manufactured diagnostic tool in near field scanning system. The purpose of this test is to compare how difference of tip length *t* will take effect to the probe performances. The tip length of monopole probe is the length by which the inner conductor is made longer than the outer conductor (copper shield) at the probing end.

Figure 4-11 is the monopole probe used for scanning. The diameter of outer shield is 320 μm, and the diameter of inner conductor is 50 μm. The tests were conducted with two identical coaxial probes with different tip lengths (*t*) of 0.5 mm and 2 mm respectively. The DC motor scanning station (Figure 3-7) was used for testing.

Two 50 Ω open circuit CPW T-Lines (Type A and Type B) were measured at 5 GHz. Their parameters are listed in Table 4-1.

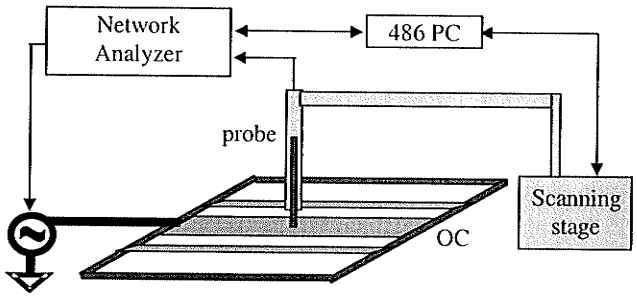

Figure 4-12 Test structure to measure CPW T-lines

The test set up is shown in Figure 4-12. HP 8753A network analyzer (up to 6 GHz) was used to excite the circuit under test and to pick up the signal to finally get the S_{21} forward transmission parameters. Two DC-controlled motors composed of the scanning stage that made the movable probe doing 1D/2D scanning over the circuit area. Computer workstation was controlling the activities of the network analyzer (through GPIB bus)

and the scanning stage (through RS-232 port), and processing data from the network analyzer.

The transverse scan, for which the probe was moving along the path 2.5 cm away form the edge of open circuit end of the CPW T-Line, was run over the open-circuited Type A CPW (w = 740 μm and s = 330 μm) with both monopole probes (different tip lengths) at frequency of 5 GHz. The probes were over the CPW circuit plane about 0.1 mm high. Figure 4-13 shows the scanning results with both monopole probes. The 0.5 mm tip length monopole probe found minimum induced signal at displacement around 820 μm. The Laplace BV problem solution for the same Type A CPW shows (Figure 4-7) that the minima occurs at displacement around 610 μm. The deviance of numerical and experimental results is about 34%. The 2-mm tip length monopole probe, on the other hand, was not able to reflect the proper electric field transverse variation as expected from the Laplace BV problem solution in Figure 4-7.

The longitudinal scan was also applied to an open-circuited Type A CPW T-Line by the 0.5 mm tip length monopole probe, the probe was over the CPW at about 0.1 mm height, and the signal frequency was 5 GHz. The test results are shown in Figure 4-14. From the standing wave pattern on the magnitude plot, half wavelength of guided wave $\lambda_g/2$, was measured 21.5 mm. Using $\lambda_g = c/f\sqrt{\varepsilon_{eff}}$, the ε_{eff} obtained by experiment was 1.94. Noted that the ε_{eff} calculated by PCAAD was 1.87, the deviance of simulation and measurement was 3.7%.

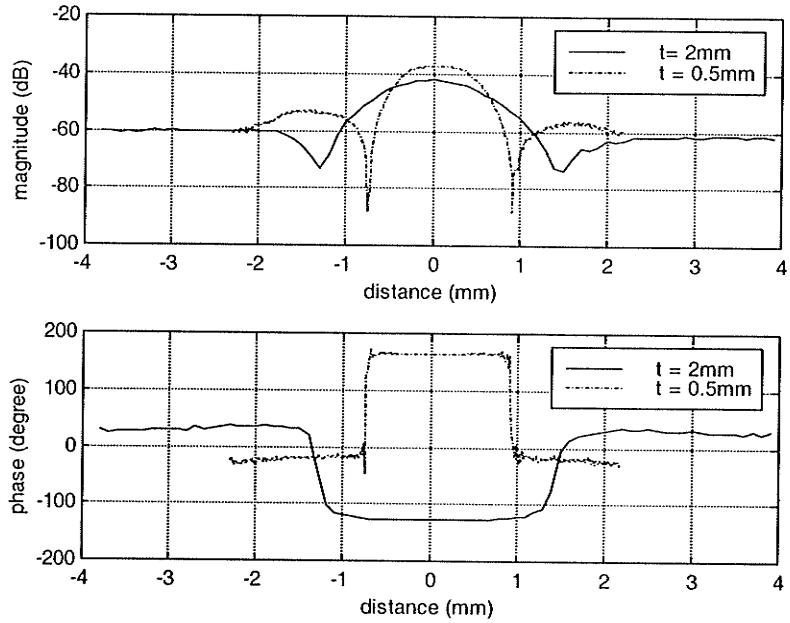

Figure 4-13 Magnitude and phase plot of transverse scan over Type A CPW with two monopole probes having different tip lengths

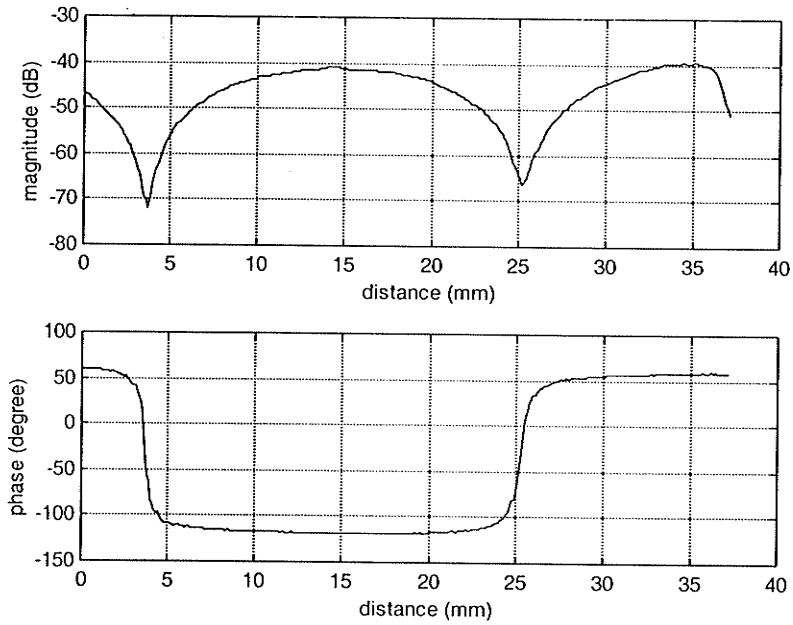

Figure 4-14 Magnitude and phase plot of longitudinal scan along the signal line of Type A CPW with 0.5 mm tip length monopole probe

4.2 Monopole Probe to Measure Single Patch Microstrip Antenna

Since the mid 1970's the rectangular patch has been one of the most widely used antennas in communication developments [41] . A single patch antenna is the fundamental element in the design of an ideal antenna array. To determine the pattern of amplitude and phase of a single patch antenna, a test system was set up as shown in Figure 4-18 b) which is almost the same as the configuration used for CPW T-Lines measurements except for the DUT here is a single patch antenna.

To investigate an antenna component, the most important measurements are:

- VSWR for indication of mismatch
- mode excitation for element cross-polarization
- surface wave excitation for estimation of the element mutual coupling level

4.2.1 Properties of Single Patch Microstrip Antenna

Generally a single patch microstrip antenna is composite of three segment of microstrip transmission lines with specific dimensions (width W and length L) working at the expected operating frequency f_r. Figure 4-15 shows the dimensions of a single patch microstrip antenna working at 3.455 GHz. The three segments are signal feed line, quarter wavelength transformer and rectangular patch built on the substrate with $\varepsilon_r = 3.2$. The single patch microstrip antenna is designed to be operating at its resonating mode, for which the frequency of signal fed to the patch is close to the resonant frequency f_r.

In following analysis, we are simply considering rectangular patch in the first mode that is the first order resonance frequency occurs on the patch.

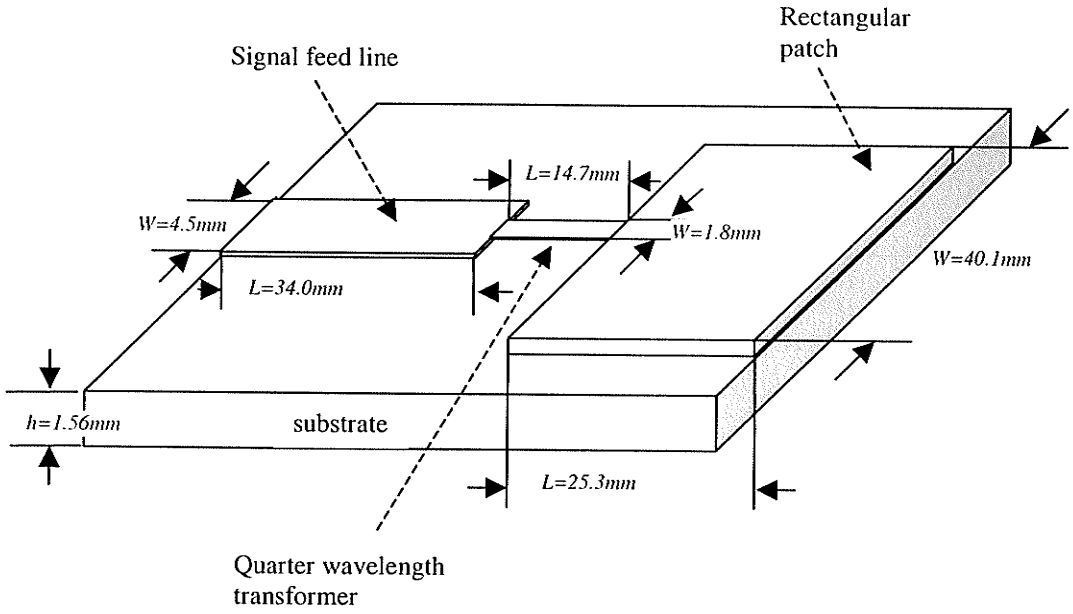

Figure 4-15 Dimensions of the open-ended single patch microstrip antenna design

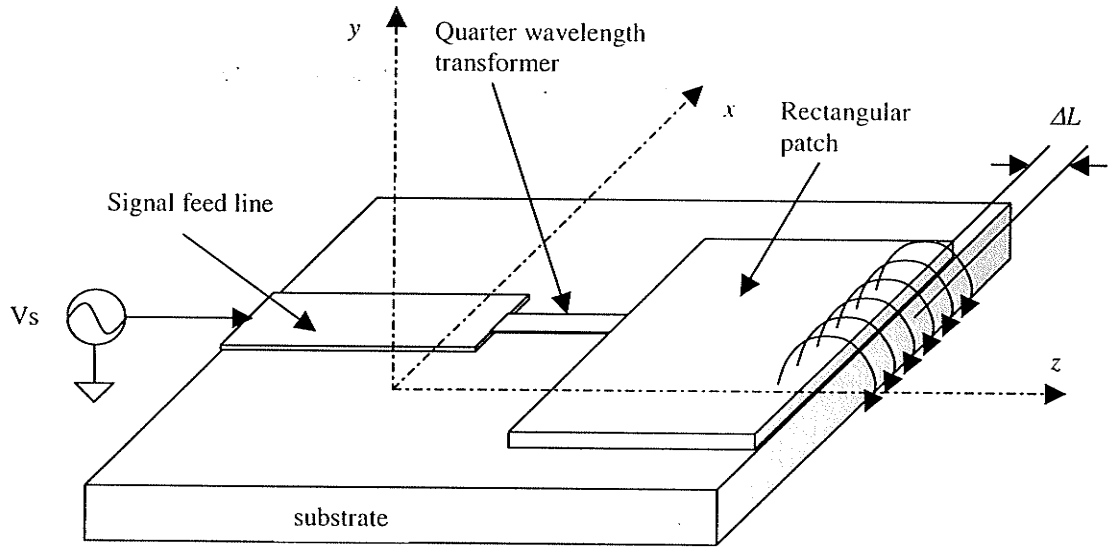

Figure 4-16 Structural diagram of a single patch microstrip antenna design

A typical single patch antenna design is to combine the microstrip transmission line, which is feeding the signal to antenna with the microstrip patch antenna on the same substrate (Figure 4-16). To match the impedance of the microstip signal feed line to the microstrip patch, a quarter-wavelength transformer has to be inserted between the signal feeding line and the patch. The quarter wavelength transformer technique is generally used to match purely resistive loads [42] .

It is also illustrated in Figure 4-16 that the electric fields, along the z direction, undergo fringing at the edges of the patch since the open-ended patch is finite along both length and width (x axis and z axis). This fringing effect has to be taken into account by adding equivalent lengths ΔL at both ends.

$$\frac{\Delta L}{h} = 0.412 \frac{(\varepsilon_{eff} + 0.3)(\frac{L}{h} + 0.264)}{(\varepsilon_{eff} - 0.258)(\frac{L}{h} + 0.8)} \qquad (4\text{-}17)$$

C. A. Balanis [41] gives out equations to calculate the parameters for rectangular patch design at resonant frequency. Some values are calculated now for the designed single patch antenna shown in Figure 4-15 and Figure 4-16.

The effective dielectric constant of the patch

$$\varepsilon_{eff} \cong \frac{\varepsilon_r + 1}{2} + \frac{\varepsilon_r - 1}{2}\left(1 + \frac{10h}{W}\right)^{-\frac{1}{2}} \approx 3.03 \qquad (4\text{-}18)$$

Given the resonant frequency f_r = 3.455 GHz,, the equivalent rectangular patch length can be calculated by (4-19), where c is the free space speed of light.

$$L_e = L + 2\Delta L = \frac{c}{2f_r\sqrt{\varepsilon_{eff}}} = 0.0249\,m \tag{4-19}$$

In a typical design, the signal feed line is a 50 Ω impedance transmission line. Given the substrate thickness h and dielectric constant ε_r, the transmission line width W and effective dielectric constant ε_{eff} can be then calculated. With the patch width W is much greater than the substrate thickness h ($W/h >> 1$), the antenna will behave more as transverse electromagnetic wave (TEM) transmission line, so the entire line feed single patch antenna can be equivalent to serialized transmission lines with different line impedance and ε_{eff}, as shown in Figure 4-17.

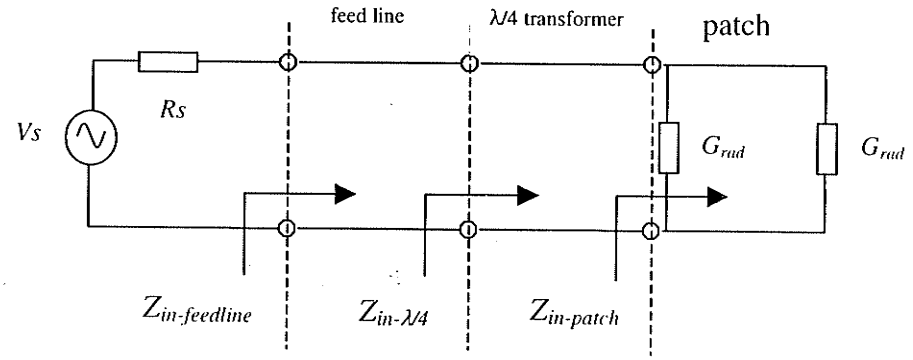

Figure 4-17 Equivalent circuit of microstrip line feed single patch antenna

For the design shown in Figure 4-15 and Figure 4-16, the radiation conduction at the open end of rectangular patch is calculated as [41]

$$G_{rad} = \frac{1}{3\pi\eta}\left(\frac{60(k_0W)^2}{1+(k_0W)^2}\right)\left[1+0.32+0.68\cos(0.77k_0L_e)\right] = 0.0388\,\Omega^{-1} \tag{4-20}$$

where

$$k_0 = \frac{2\pi f_r}{c\sqrt{\varepsilon_{eff}}} \approx 41.55$$

$$\eta = \frac{120\pi}{\sqrt{\varepsilon_{eff}}} \approx 216.45$$

From equivalent circuit Figure 4-17, the input impedance of rectangular patch can be approximated as

$$Z_{in-patch} = \frac{1}{2G_{rad}} \approx 12.88\Omega \tag{4-21}$$

The characteristic impedance of the $\lambda_g/4$ transformer can be calculated as

$$Z_{0(\lambda/4)} = \frac{120\pi}{\sqrt{\varepsilon_{eff(\lambda/4)}}} \frac{1}{\frac{W_{\lambda/4}}{h} + 1.393 + 0.667\ln\left(\frac{W_{\lambda/4}}{h} + 1.444\right)} \tag{4-22}$$

$$= 75.59\Omega$$

$$Z_{in-\lambda/4} = (Z_{0(\lambda/4)})^2 / Z_{in-patch} \approx 443.56\Omega \tag{4-23}$$

It is noted in (4-23) that the transformer appears not correctly designed since the look-in impedance from the transformer input port is not 50 ohms as expected. There will be mismatching between the 50 ohm signal feed line and rest of the antenna circuit.

For a lossless transmission line shown in Figure 4-10

$$V(z) = V_0^+ [1 + \Gamma_L e^{j2\beta z}] e^{-j\beta z} \tag{4-24}$$

where V_0^+ is determined by the source *Vs* and its impedance.

For an OC load, $Z_L = \infty$ and $\Gamma_L = +1$,

$$V(z) = V_0^+[1 + e^{j2\beta z}]e^{-j\beta z}$$
$$= 2V_0^+ \cos(\frac{2\pi}{\lambda_g} z) \qquad (4\text{-}25)$$

Hence, there is a standing wave with a minimum at $\lambda_g/4$ from the end of the $\lambda_g/2$ patch.

4.2.2 Single Patch Microstrip Antenna Measurement

To measure the single patch microstrip antenna shown in Figure 4-18 a), we excited the antenna patch with a 3.544 GHz RF signal from the network analyzer. The coaxial probe is right above the antenna at the height of about 0.2 mm. (The coaxial probe was touch down an isolation of plastic film lying on the surface of the antenna patch, the thickness of the film was about 0.2 mm). The pattern shape in 3-D display for the magnitude measurement is shown in Figure 4-19. The magnitude and phase pattern of the single patch antenna are shown in Figure 4-20 and Figure 4-21, respectively.

Figure 4-22 is the magnitude and phase plots along the central line in *y* direction. It is noted that the magnitude plot of the 50 ohm signal feed line section is not flat as expected due to mismatching of impedance. Given the $Z_{in\text{-}patch}$ of 12.88 ohms in (4-21), the $\lambda_g/4$ transformer had to be designed such that the $Z_{0(\lambda g/4)}$ equals to 25.38 ohms in stead of 75.59 ohms (4-22) to make $Z_{in\text{-}\lambda g/4}$ close to 50 ohms.

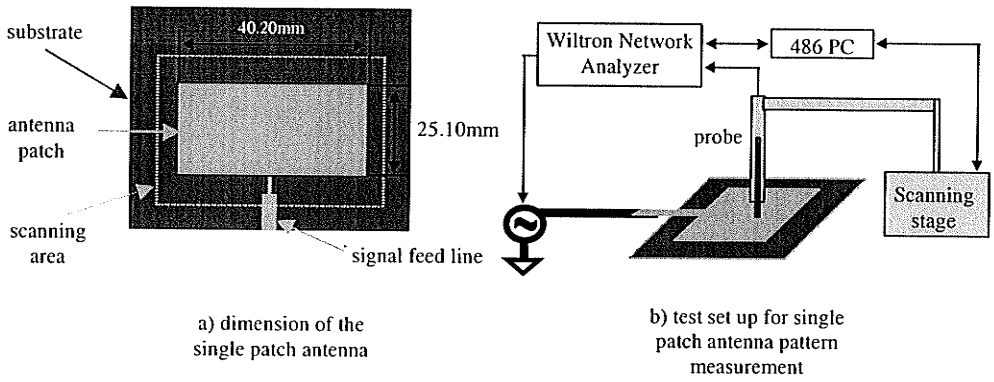

Figure 4-18 a) Single patch antenna; b) Single patch antenna test structure

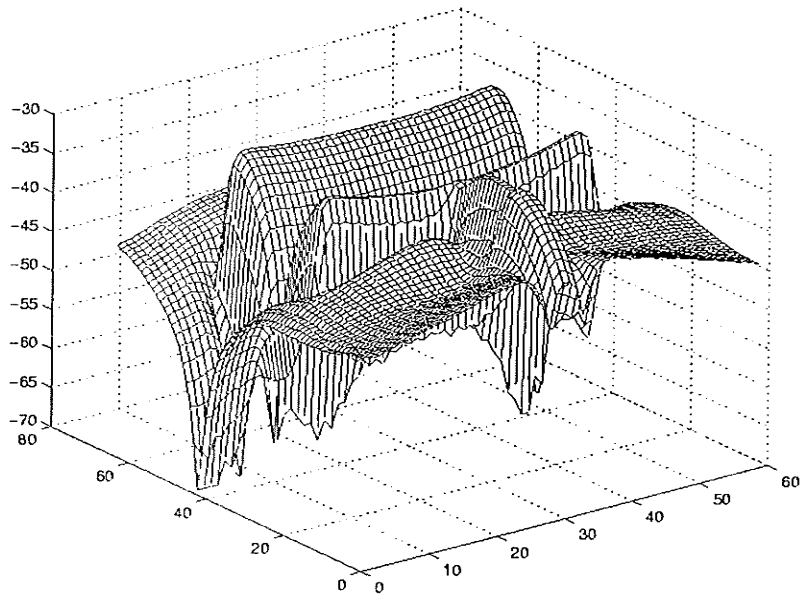

Figure 4-19 3-D display of the magnitude pattern of the single patch antenna

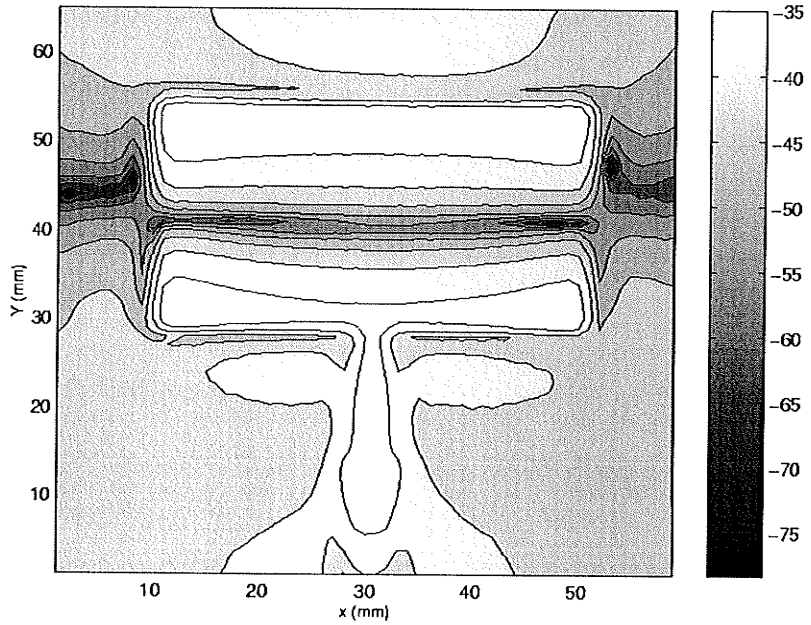

Figure 4-20 Magnitude pattern of the Single patch antenna

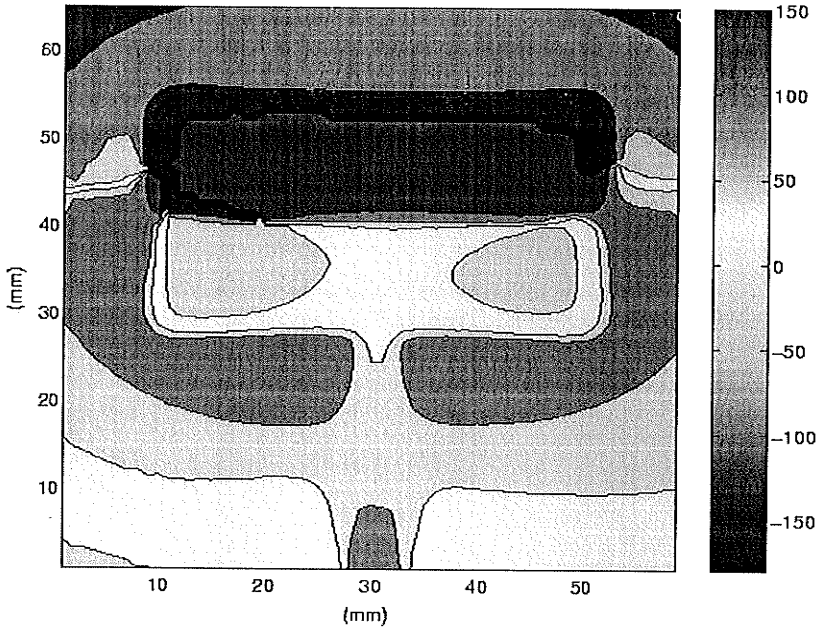

Figure 4-21 Phase pattern of the Single patch antenna

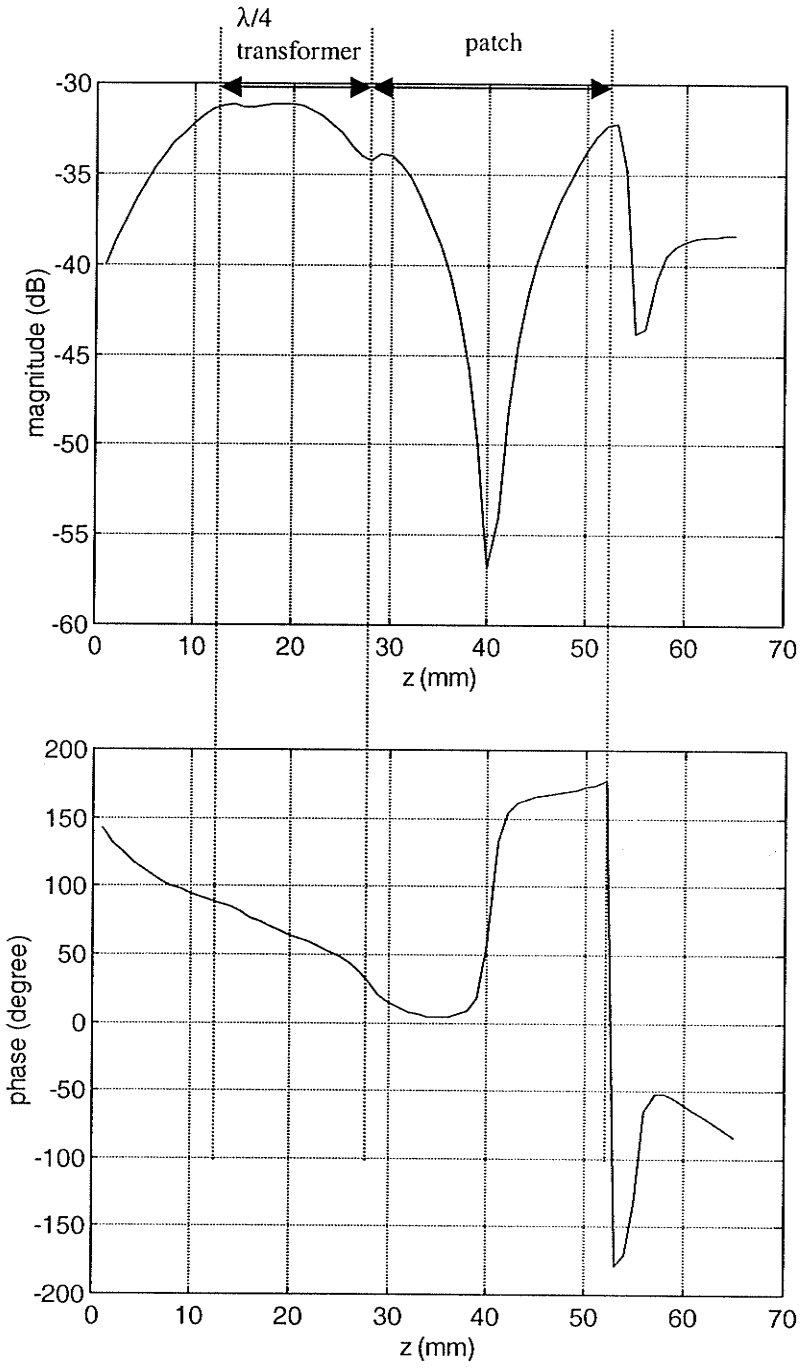

Figure 4-22 Magnitude (upper) and phase (lower) plot - longitudinal scanning over the antenna patch along the central line

4.3 Monopole Probe to Measure Microstrip Antenna Array

4.3.1 Microstrip Antenna Array Topologies and Signal Feeding Network

As an application of near-field probing technology to measure the microwave circuits, the monopole probe scanning system was used for investigation on 4x4 antenna array topologies at 12 GHz. A survey of 4x4 array topologies at 12 GHz was conducted by D. Gray, a Ph.D. student of the Department of Electrical and Computer Engineering at the University of Manitoba. Seven 4x4 Microstrip antenna arrays fed with different singal feeding networks were fabricated using 0.794 mm thick, ½ ounce copper clad Arlon Diclad substrate ($\varepsilon_r = 2.5$) [43] . Use of a constant substrate and design frequency allows for direct comparison of the arrays behaviour as a function of topology alone. The designed resonant frequency of the antenna arrays are both between 11 GHz – 13 GHz. Two types of antenna array, type C and type E [43] were chosen for the tests using monopole probe scanning system. The dimensions of type C and type E antenna array are shown in Figure 4-23 and Figure 4-24, respectively.

The purpose of the measurement is to experimentally investigate the performance of microstrip feeding network and radiation pattern of each antenna patch. It was expected to see same radiation pattern for both magnitude and phase on all patches and fundamental mode as the only dominant mode and no other higher order modes. It was also investigated if the feeding network is imbalance.

Figure 4-25 shows the measurement results on the type C antenna array with 12 GHz RF feed signal from the network analyzer. The coaxial probe was at about 0.2 mm height above the antenna. For patch 1 and 2, it was observed that they are fed with the same

amplitude and phase but with slight excitation of 3rd order mode. Patch 3 and 4 have similar behaviour show that higher order modes had predominant effects.

The feeding network show small VSWR in the section marked in Figure 4-25, the linear phase shift indicates impedance matching.

The same measurement was applied to the antenna array type E fed with 12 GHz RF signals, and the results are shown in Figure 4-26. The modes generated on four patches are more predominantly the fundamental modes. The feeding network also show small VSWR in the section marked in Figure 4-26.

Type E has better performance than type C as shown in Figure 4-28, which agrees well with the theoretical modelling [43] .

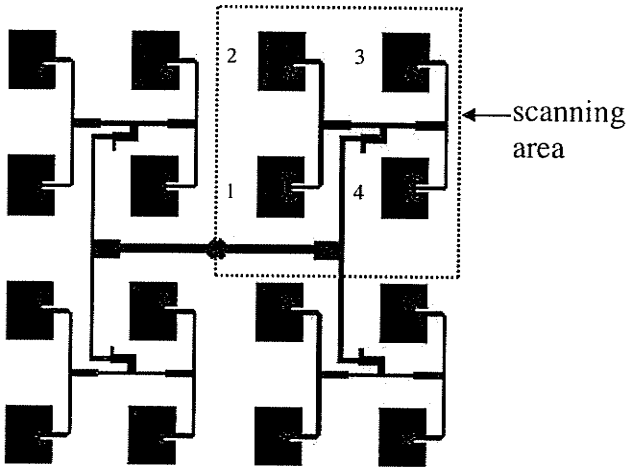

Figure 4-23 The layout of type c antenna array

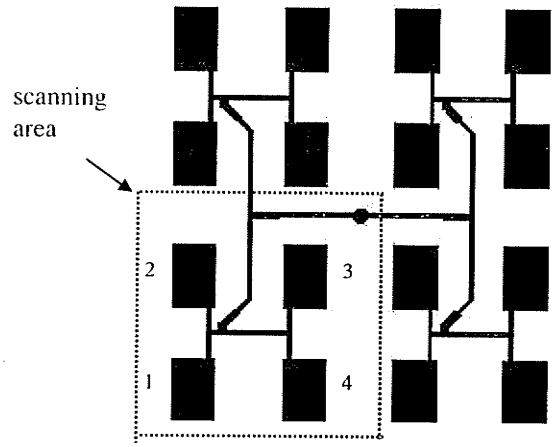

Figure 4-24 The layout of type e antenna array

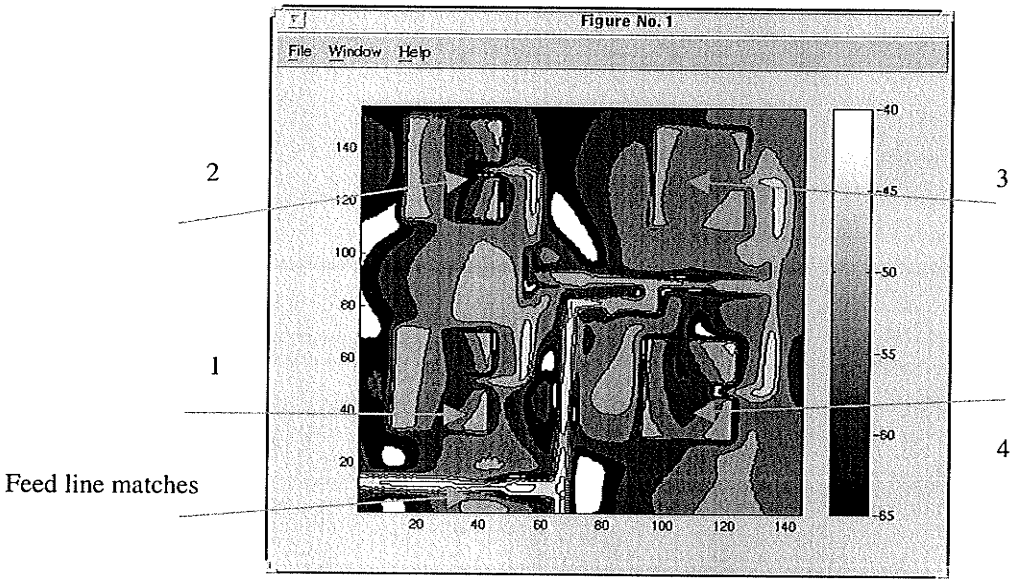

a) measured magnitude pattern of type c antenna array driven by 12GHz RF signal

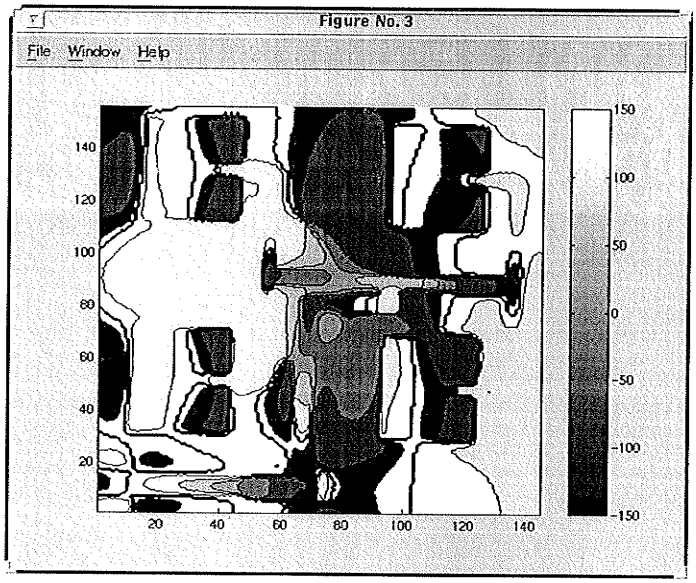

b) measured phase pattern of type c antenna array driven by 12GHz RF signal

Figure 4-25 Near-field image of type C antenna array driven by 12 GHz RF signal

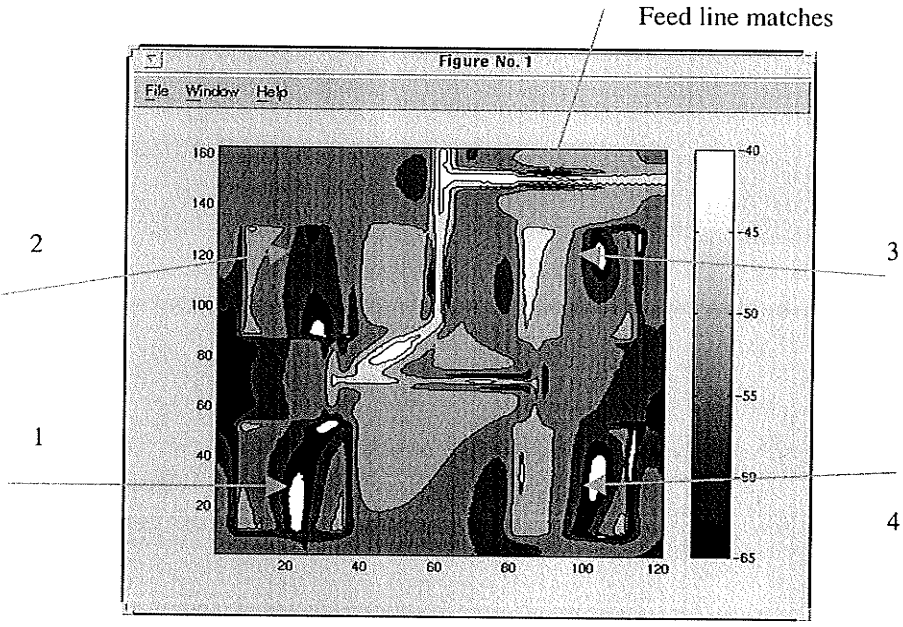

a) measured magnitude pattern of type e antenna array driven by 12GHz RF signal

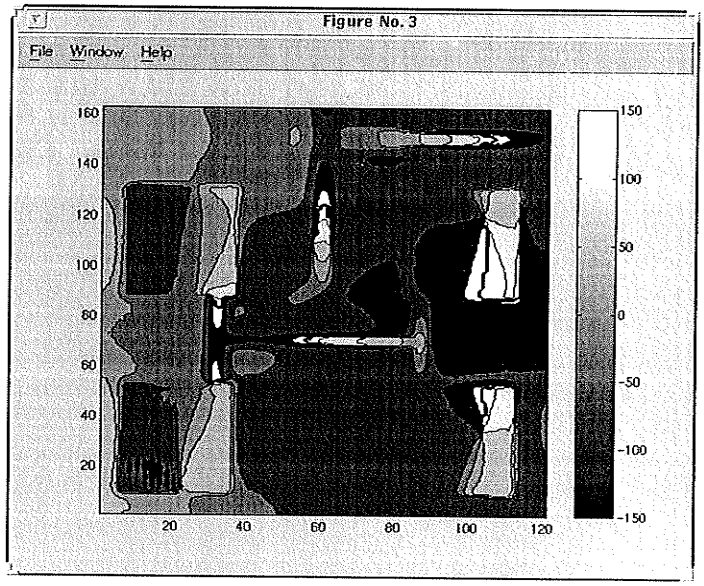

b) measured phase pattern of type e antenna array driven by 12GHz RF signal

Figure 4-26 Near-field image of type E antenna array driven by 12 GHz RF signal

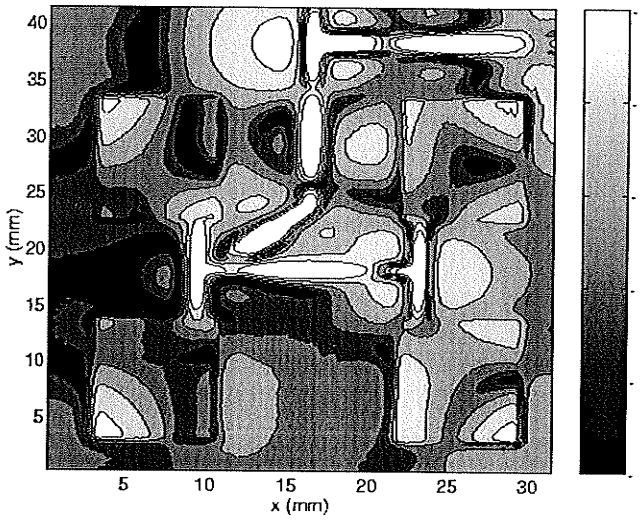

a) measured magnitude pattern of type e antenna array driven by 13GHz RF signal

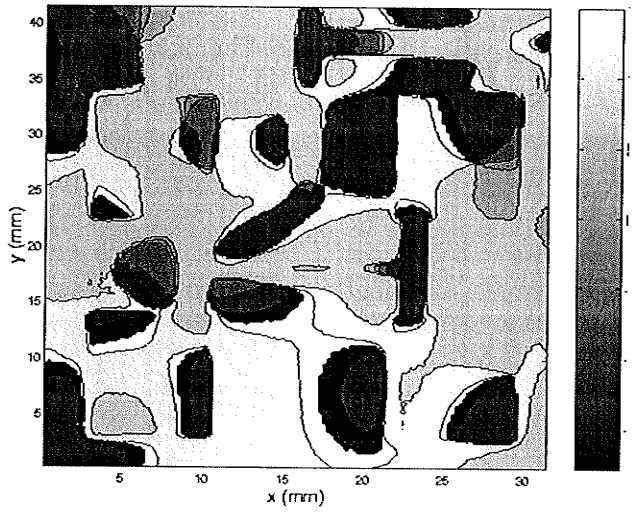

b) measured phase pattern of type e antenna array driven by 13GHz RF signal

Figure 4-27 Near-field image of type E antenna array driven by 13 GHz RF signal

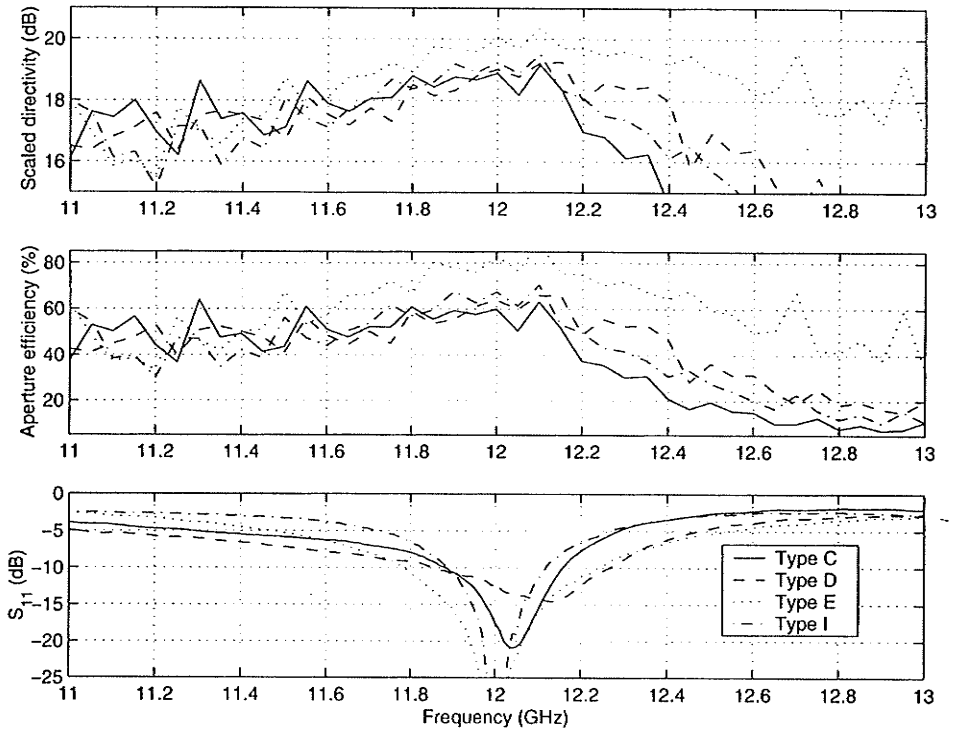

Figure 4-28 Boresight radiation and input impedance characteristics of 12 GHz 4x4 microstrip arrays [43]

4.4 CPW Probe to Measure 50Ω CPW T- Line

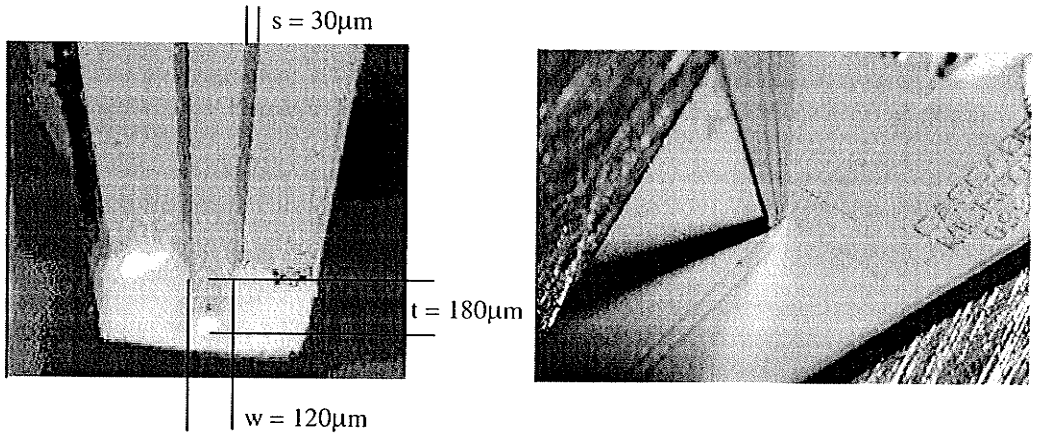

a) CPW probe

b) CPW probe to measure the type B CPW

Figure 4-29 a) CPW Probe b) snapshot of CPW probe and the DUT

To improve the spatial resolution of an electric near-field probe the micromachining process has been employed to fabricate μm-scale probes. It is, however, unfeasible to build probes in a form of coaxial cable by micromachining technique. The planar structure of coplanar waveguide has provided much flexibility in design, reduced weight and volume, and cost of production. It is for this reason that a CPW probe was fabricated and tested as a scale model of the micromachined coplanar waveguide probe. The test configuration and dimension of the CPW probe is shown in Figure 4-29.

4.4.1 CPW T-line Probe Circuit Modelling

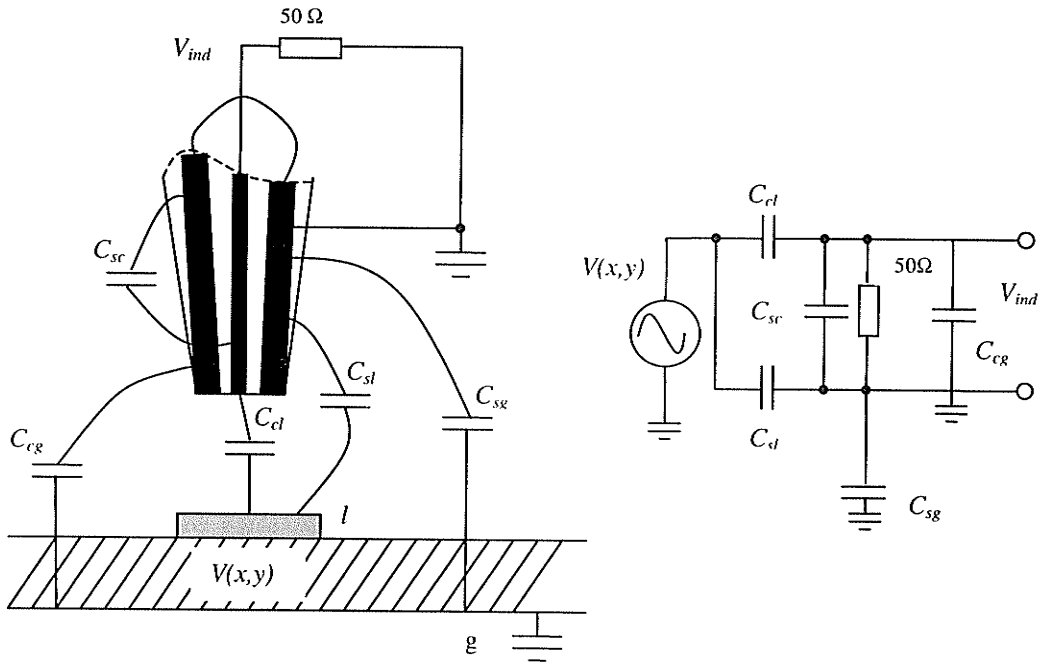

Figure 4-30 An approximate coplanar waveguide transmission line probe model and the corresponding equivalent circuit model

Figure 4-30 shows the model of coplanar waveguide transmission line (CPW) probe and its approximate equivalent circuit. The model is quite similar to a monopole probe model shown in Figure 3-2, so the modelling and analysis will be also similar. The results drawn from the analysis of monopole probe in section 3.2 is also applicable to CPW

probe modelling. The model also assumes that the probe load impedance is much greater than local circuit impedance. C_{cl} is the capacitance formed between conductor of probe and transmission line circuit, C_{sc} is the capacitance formed between probe conductor and shield, C_{sl} is the capacitance formed between shield of probe and transmission line circuit, C_{cg} is the capacitance formed between probe conductor and ground plane, C_{sg} is the capacitance formed between probe shield and ground plane.

4.4.2 50 Ω CPW T- Line Measurement with Different CPW Probe Orientations

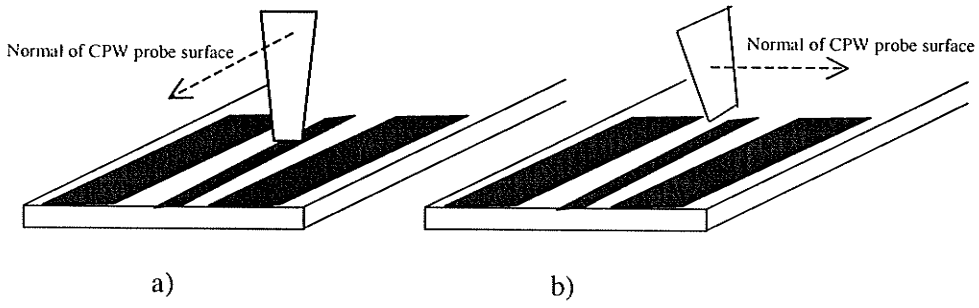

Figure 4-31 a) The CPW probe surface normal is parallel to signal line and b) The CPW probe surface normal is orthogonal to signal line

This measurement is performed to find the effect to the electric coupling level between CPW probe and circuit under test when the probe is set to different orientations over the circuit plane. The normal of CPW probe surface, as shown in Figure 4-31 a) and b), is either parallel to or orthogonal to the signal line of CPW T-line. A Type A CPW T-line was measured and the results are shown in Figure 4-32 and Figure 4-33. From the analysis to CPW in section 4.1.1.1, it is expected that the orientation of the CPW probe not to make much difference on measurement results, since the induced voltage on the probe is mostly depending on probe height and tip length. Figure 4-32 and Figure 4-33 experimentally state the same conclusion.

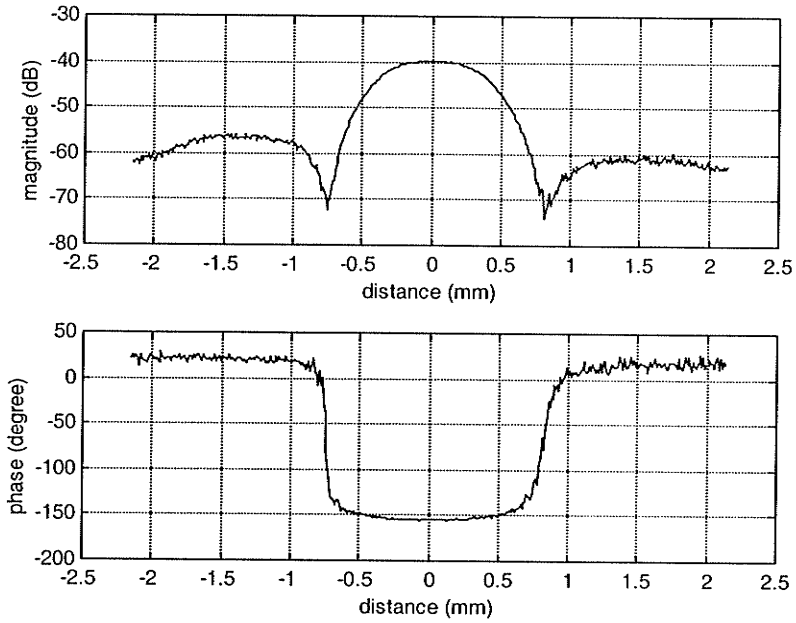

Figure 4-32 CPW probe transverse scan over the Type A CPW with probe surface normal parallel to the CPW T-line under test

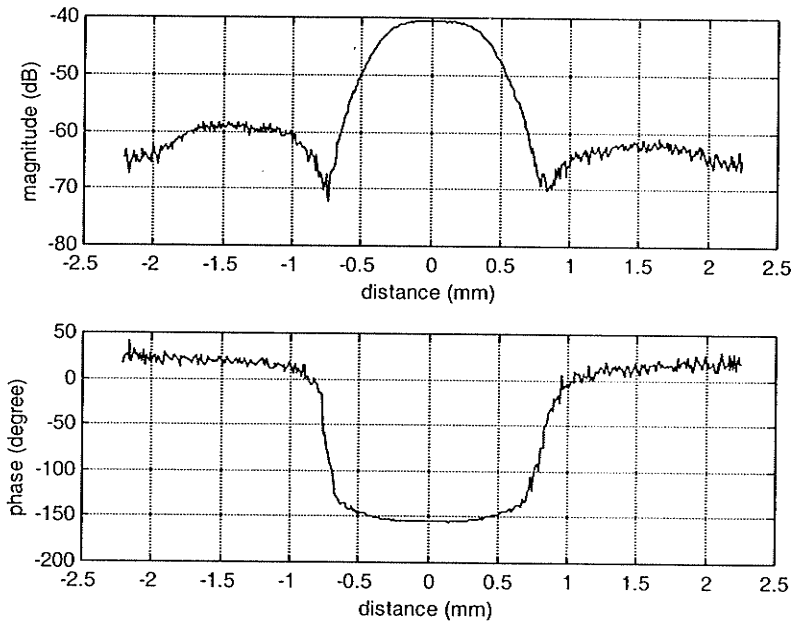

Figure 4-33 CPW probe transverse scan over the Type A CPW with probe surface normal orthogonal to the CPW T-line under test

4.4.3 50 Ω CPW T- Line Measurement with CPW Probe at Different Heights above DUT

The heights at which the probe is positioned over the CPW T-line have effects to the measurement performance. The tests discussed in this section were performed in order to investigate these effects. The circuit was running at frequency of 5 GHz, and the probe was set at the height of 0.5w, w, 2w and 4w, where w is the width of the signal line of CPW T-line, to scan transversely over the DUT. A Type B CPW T-line (w = 0.2 mm and s = 0.1 mm) was measured for this purpose. The measurement results for the probe set at different heights are presented in Figure 4-34, Figure 4-35, Figure 4-36 and Figure 4-37, respectively. Figure 4-38 compares the magnitude of measurements and shows that height of 2w has the best performance.

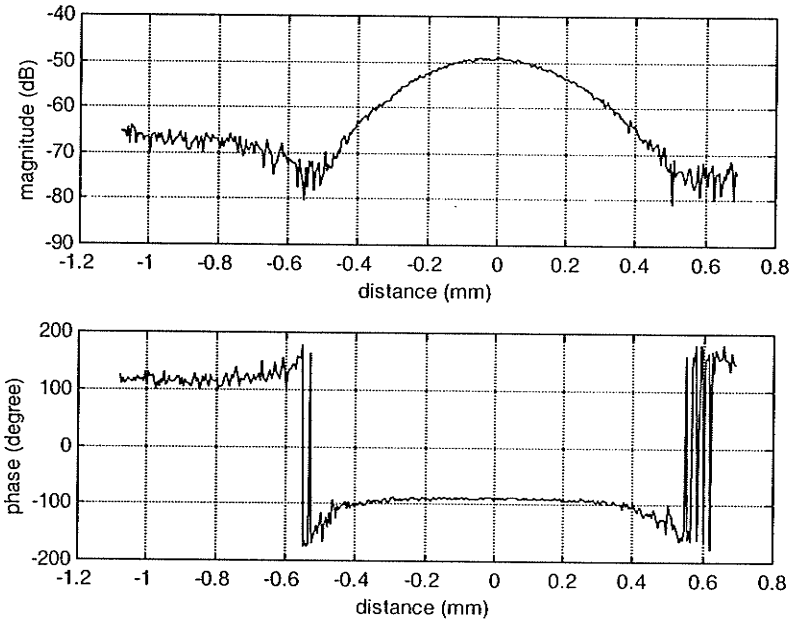

Figure 4-34 CPW probe transverse scan result on CPW transmission line, height of 0.5w

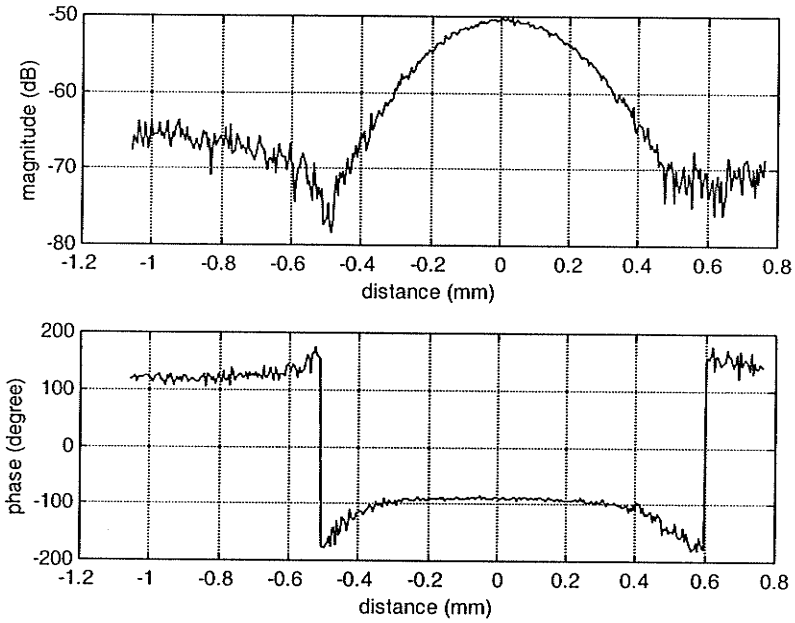

Figure 4-35 CPW probe transverse scan result on CPW transmission line, height of w

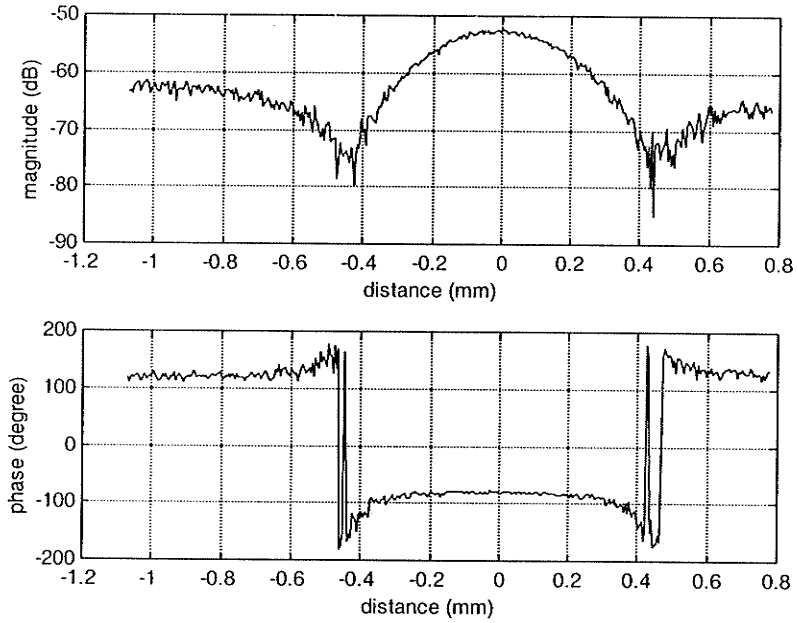

Figure 4-36 CPW probe transverse scan result on CPW transmission line, height of 2w

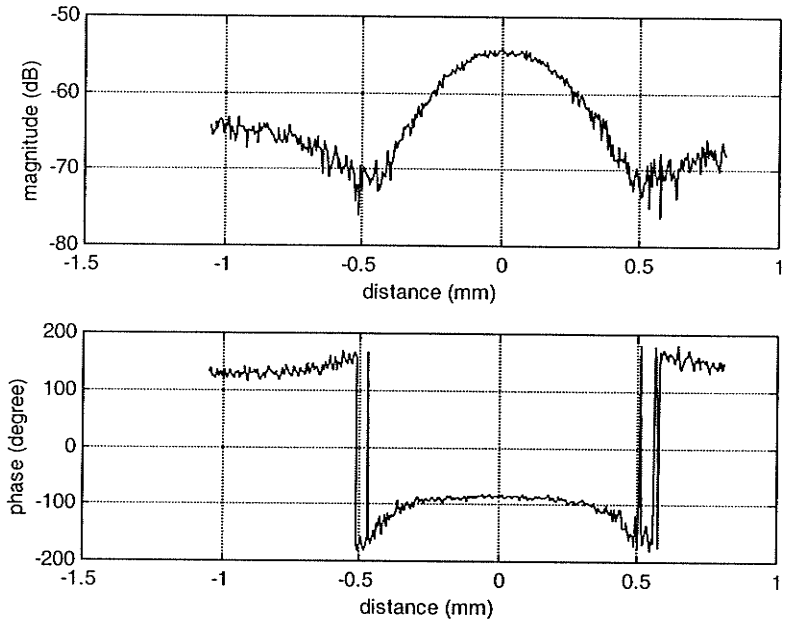

Figure 4-37 CPW probe transverse scan result on CPW transmission line, height of 4w

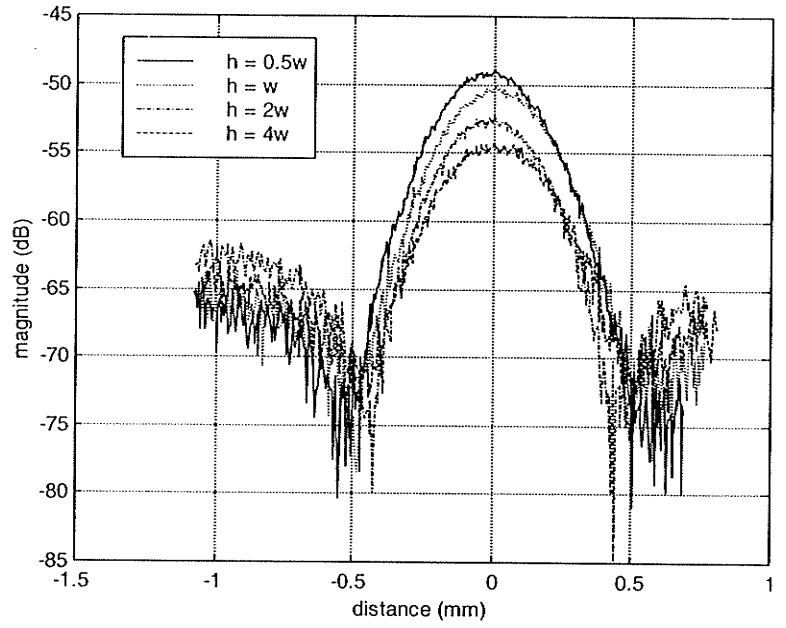

Figure 4-38 Measurement of magnitude, CPW probe transverse scan over the DUT at height of 0.5w, w, 2w, 4w

4.4.4 50 Ω CPW T- Line Measurement with CPW Probe and Monopole Probe – A Comparison

The transverse scan is applied to both Type A and B CPW T-Lines with CPW probe, and the results are shown in Figure 4-39 and Figure 4-41. The probe is right above the CPW with height between 25 μm to 50 μm.

The same measurement was repeated using the monopole probe with the tip length t = 0.5 mm. The results are shown in Figure 4-40 and Figure 4-42. The monopole probe is also at a height between 25 μm to 50 μm over the DUT. These results can be referred to, for evaluating the performance of the CPW probe.

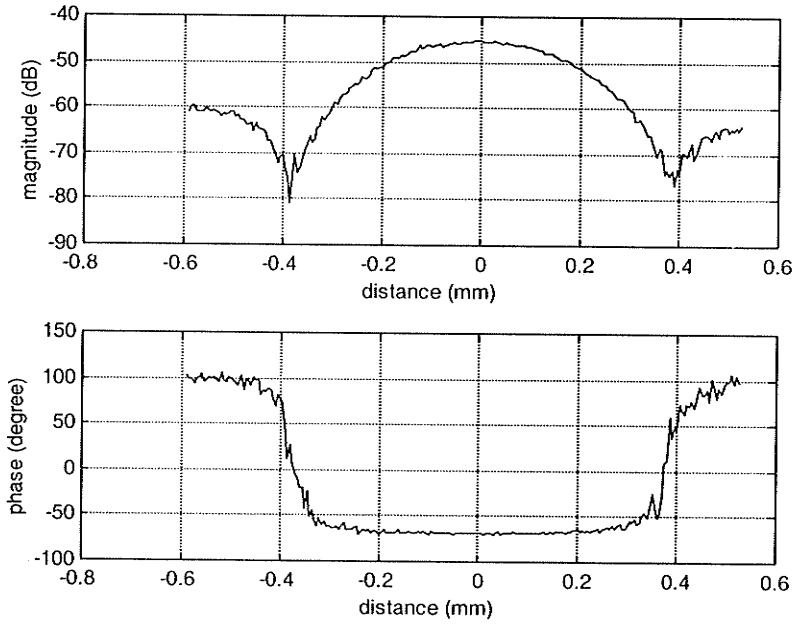

Figure 4-39 CPW probe transverse scan result on the Type B CPW T-Line

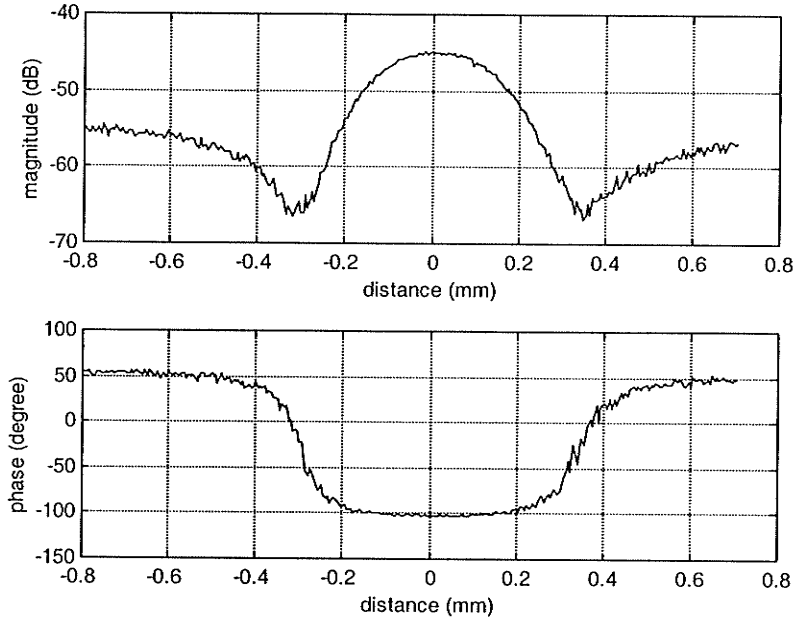

Figure 4-40 Monopole probe transverse scan result on the Type B CPW T-Line

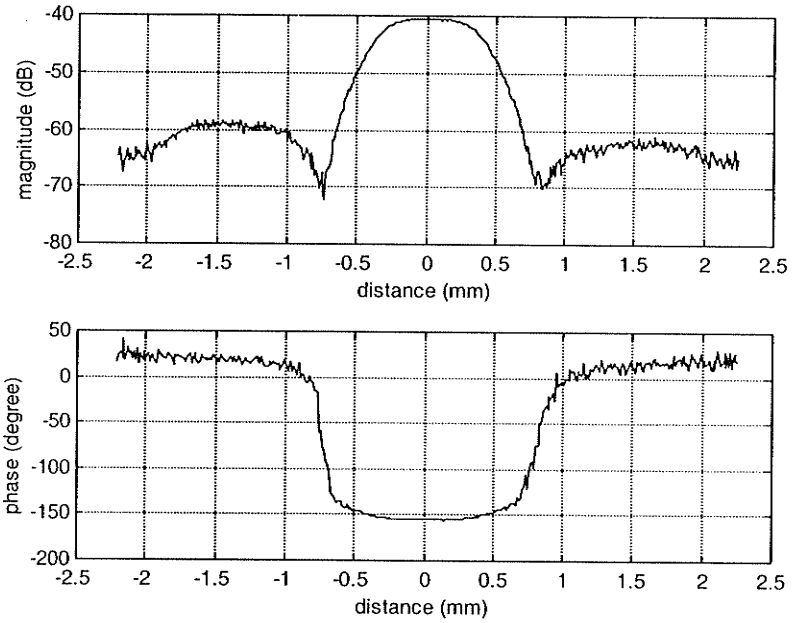

Figure 4-41 CPW probe transverse scan result on the Type A CPW T-Line

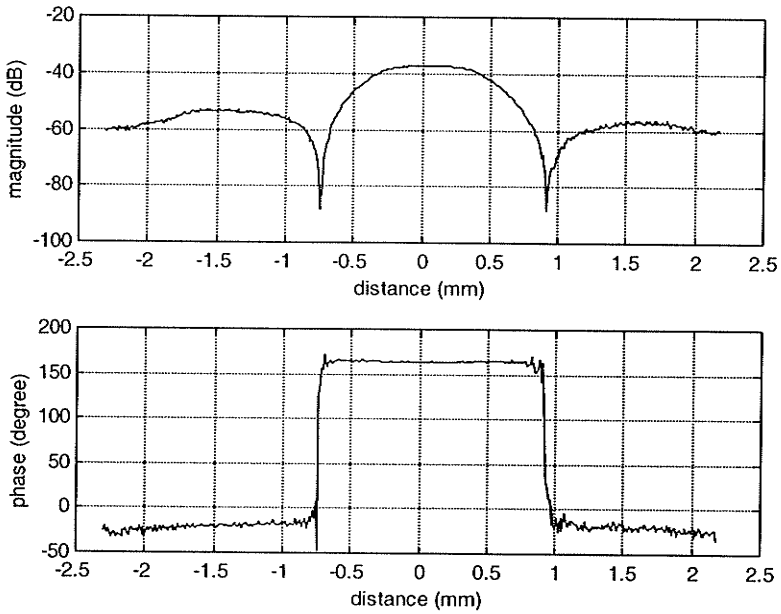

Figure 4-42 Monopole probe transverse scan result on the Type A CPW T-Line

4.5 Conclusion

Various microwave devices were tested by monopole and CPW probes with the automated near-field scanning system described in Chapter 3. The performance of both monopole and CPW probes were investigated by measuring two different CPW transmission lines. Both transverse and longitudinal scan were conducted and results were compared with the numerical analysis of transverse and longitudinal variation of electric field in section 4.1.1. The probes were also used to measure the single patch antenna of 3.45 GHz resonance frequency and two types of microstrip antenna arrays.

Chapter 5 MICROFABRICATED CPW PROBES

With constantly increasing frequencies in communications and integrated circuits, there is a great demand for low-cost, miniature microwave components. The planar transmission lines, such as microstrip, stripline, and coplanar waveguide have provided much flexibility in design, reduced weight and volume, and cost of production. Planar component size has reduced so much that the fabrication by conventional machining techniques has become too costly and difficult. It is for this reason that the recent advanced micromachining techniques have found numerous applications in the microwave field.

5.1 Introduction

In conjunction with its conventional role as an electronic material, silicon can also be exploited as a high-precision, high-strength and high-reliability mechanical material by taking advantage of an already advanced micro-fabrication technology. This is especially applicable wherever miniaturized mechanical devices and components must be integrated or interfaced with electronics. Texas Instruments has been marketing a thermal point head [46] in several computer terminal and plotter products since early 1977 in which the active printing element abrasively contacting the paper is a silicon integrated circuit chip. The crucial detector component of a high-bandwidth frequency synthesizer sold by Hewlett-Packard [46] was made as a silicon chip in 1980 from which cantilever beams have been etched to provide thermally isolated regions for the diode detectors. High-precision alignment and coupling assemblies for fiber-optic communication systems are produced by Western Electric [46] from anisotropically etched silicon chips simply because it is the only technique capable of the high accuracies required. Some recent works carried out by G. M. Rebeiz [47] in the Radiation Laboratory in the University of Michigan shows that micromaching techniques can be used to alter the electromagnetic

characteristic of the underlying substrate so as to result in better performance than standard planar designs. They designed some high Q resonators, low-cost filters, and high efficiency micromachined antennas. The similar work is also done by V. Milanovic [48] on coplanar waveguides. It is verified that the absence of the lossy silicon substrate after top side etching results in significantly improved insertion-loss characteristics, dispersion characteristics and phase velocity.

5.2 Basic Procedures of Micromachining

The mostly used micromechanical processing techniques are etching, epitaxial processes/deposition, thermomigration, thermal bonding, and membrane techniques. The etching, deposition and membrane techniques were used in our application which will be discussed in detail in section 5.4.

5.2.1 Etch

The commonly used etching systems are chemical, plasma, sputtering and reactive-ion etching (RIE). Chemical etching is suitable for large and deep area removal while the other three etching techniques are usually used for surface/mask removal.

The chemical etchants for silicon are numerous and they can be isotropic or anisotropic, dopant dependent or not, and have varying degrees of selectivity to the masking materials. What we used in the microfabrication of CPW probe is KOH [46] , the anisotropic chemical etching which exhibits much higher etch rate ratios than any other chemical etching. A disadvantage of KOH is that SiO_2 can't be used as a mask in many applications. Si_3N_4 is the preferred masking material for KOH.

In plasma, sputtering and reactive-ion etching (RIE), the high-accelerated and heated ions are applied to the surface of silicon to remove the materials such as SiO_2 and Si_3N_4.

5.2.2 Deposition

While etching is for the material removal, the material addition in the form of film deposition, metal plating is very important structural tool. Deposited thin films have obvious applications in mask, passivation, wear resistance, corrosion protection, fatigue strength enhancement. The most common used deposition methods are chemical vapour deposition (CVD), e-beam and sputtering deposition.

CVD is a widely used method for depositing thin films of a large variety of materials such as SiO_2 and Si_3N_4. The CPW probe discussed in section 5.3 was fabricated with this technology. In a typical CVD process, reactant gases (often diluted in a carrier gas) at room temperature enter the reaction chamber. The gas mixture is heated as it approaches the deposition surface, heated radiatively or placed upon a heated substrate. Depending on the process and operating conditions, the reactant gases may undergo homogeneous chemical reactions in the vapour phase before striking the surface. Near the surface thermal, momentum, and chemical concentration boundary layers form as the gas stream heats, slows down due to viscous drag, and the chemical composition changes. Heterogeneous reactions of the source gases or reactive intermediate species (formed from homogeneous pyrolysis) occur at the deposition surface forming the deposited material.

The electron beam evaporator deposits thin metal films by means of electron beam heating and evaporation inside a high vacuum chamber. This system is primarily used for the deposition of microelectronic contact or interconnects. To avoid contaminating the metallization processes, the types of source materials and substrates allowed into the system is limited. Evaporation materials allowed are Al (pure), Al-1%Si, Pt (user must supply own Pt material). Allowed Substrates are Inorganic substrates only - Si, glass, Silicon-on-Sapphire, compound semiconductor. Sputtering deposition use the cryopumped chamber for RF/DC sputtering to form a metal plane such as Al, Cr and gold on the silicon surface.

5.2.3 Silicon Membrane

While etching and deposition are two essential procedures in micromachining, some other procedures such as thermomigration, thermal bonding, especially the dopant-dependent etching for the realization of thin silicon membranes are all employed in many applications. We used the silicon membrane in our CPW manufacturing.

Silicon membrane is important in controlling the etching processing. The etching processing will stop while arriving at a silicon layer which is highly doped with boron. It is simply because the etching rate inside the boron medium is really slow compared to the other normal silicon material.

One application of the boron-doped membrane is illustrated in the following application in the ink jet nozzle design. Without the membrane, the hole size of the ink jet nozzle will be affected by the thickness of the wafer layer (Figure 5-1 a) and b)). The size of the hole (l) equals L-(2t/tanθ), where the L is the mask dimension and t is the thickness of the wafer layer and θ = 57.74°. If a boron doped silicon membrane is produced and suspended across the bottom of the pit with an orifice in the center corresponding to the location previously left undoped (Figure 5-1 c), the hole size can be precisely controlled.

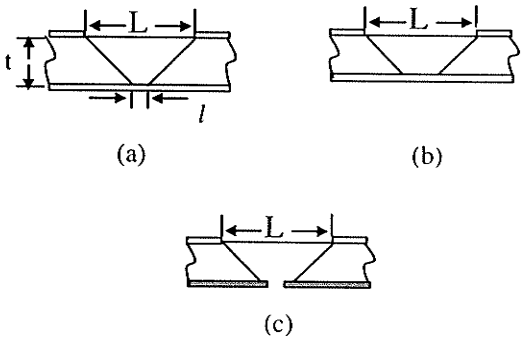

Figure 5-1 Boron membrane in the fabrication of silicon ink jet nozzle - a) and b) show the errors in final nozzle size which occurs when the wafer thickness varies c) shows a boron membrane structure to minimize the effects of the wafer thickness.

5.3 Micromachined CPW Probe

Before we start to describe the processing procedures of the manufacture of our CPW probe, it is helpful to understand its architecture and dimension. Its dimension and a picture of micromachined CPW probe are shown in Figure 5-2.

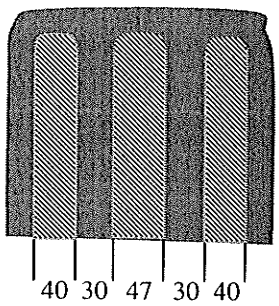

The dimension of the probe tip
(unit is μm)

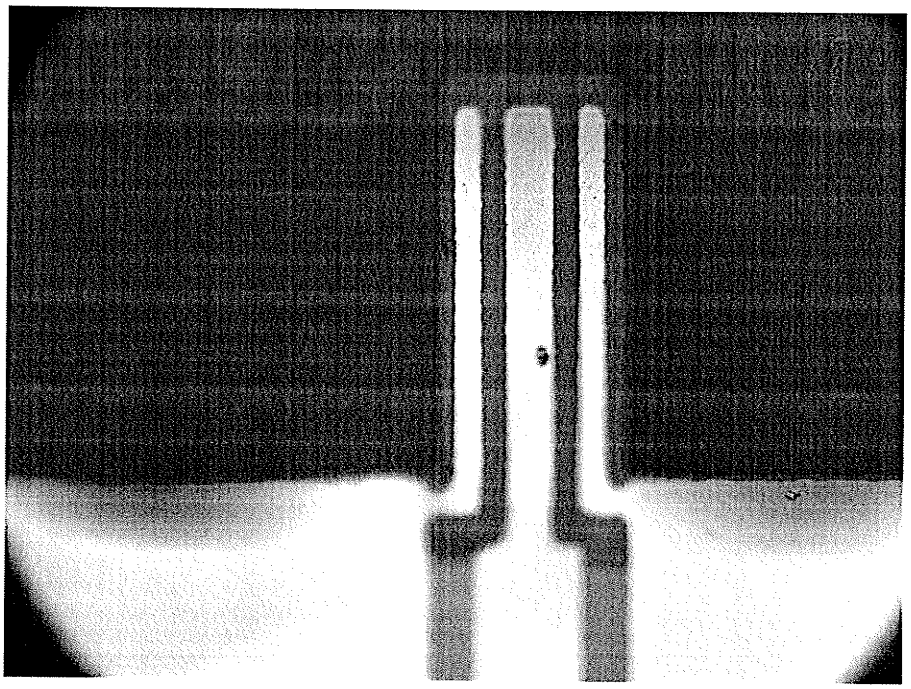

Figure 5-2 Dimension and the picture of the micromachined Coplanar Waveguide (CPW) probe

The probe was manufactured on a 400 μm Si wafer, which is partially etched previously until a 30 μm boron doped membrane layer is reached. The extra layers of 1.2 μm SiO_2 and 0.1 μm Si_3N_4 are deposited on the 400 μm Si wafer surface, which is the platform of the probe tip. The conductive material for the CPW three transmission line is 1.13 μm Au and 500 Å Cr. (Figure 5-3 a) and b)). This was designed and fabricated at the Alberta Microelectronics Centre by Dr. C. Shafai in 1996 [62] .

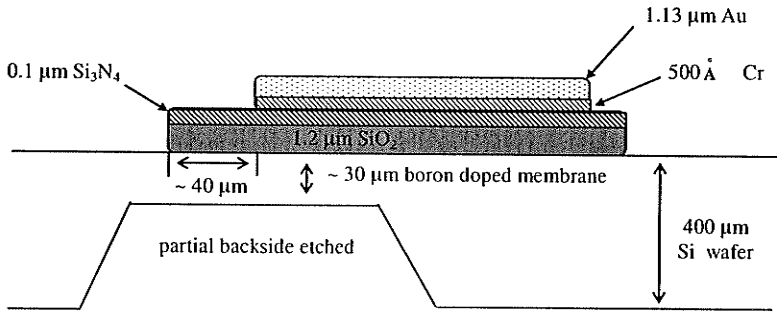

(a) the side view of the layout of the CPW probe

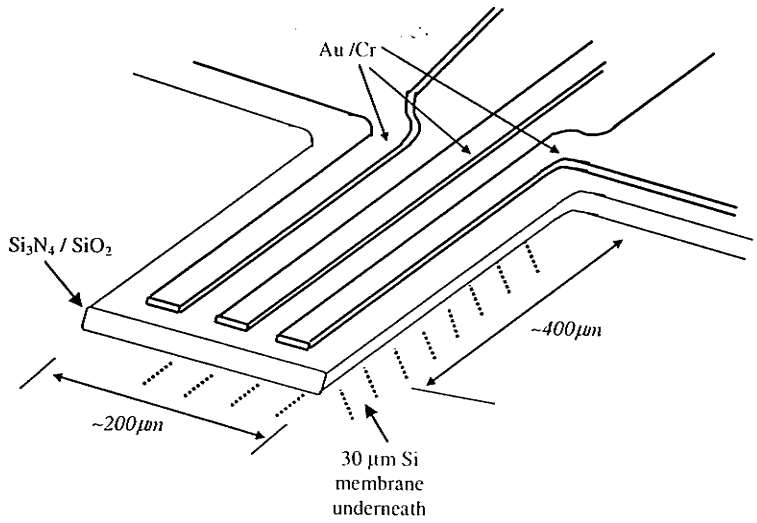

(b) top view of the layout of the CPW probe

Figure 5-3 The layout of Co-Planar Waveguide (CPW) Probe [62]

The fabrication procedure [62] started with Si wafer <100> with 400 μm in thickness.

- Dope the Si wafer with boron dopant on the surface with 30 μm thickness to form a boron membrane.
- Deposit 1.2 μm SiO2 @ 300 °C on the surface of Si wafer by Chemical Vapour Deposit (CVD), annual @ 1100 °C for 20 minutes, Figure 5-4 a).
- Deposit 0.1 μm Si3N4 @ 300 °C on the surface of SiO2 layer by CVD, Figure 5-4 a).
- Deposit 0.1 μm Si3N4 @ 300 °C at the back of the Si wafer by CVD. Then pattern the backside Si3N4 layer with RIE plasma etch. This patterned layer will be used as mask for the next KOH etch procedure, Figure 5-4 a).
- KOH etch @ 80 °C for 6 hours to remove the Si until arriving the boron membrane layer to form Si diaphragm, Figure 5-4 b).
- Pattern and etch top Si3N4 and SiO2 dielectrics by RIE to make Si exposed, Figure 5-4 c).
- Deposit 1.13 μm Au, 500Å Cr and 0.25 μm gold by sputtering deposition and then patter and etch metals to form probe tip, Figure 5-4 d).
- To remove the exposed Si, etch the Si diaphragm from back by RIE, Figure 5-4 e).

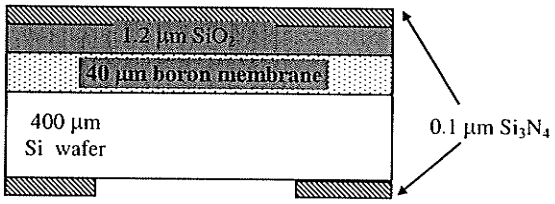

(a) the 400 μm Si wafer doped with boron membrane and deposited with 1.2 μm SiO_2 and 0.1 μm Si_3N_4 mask

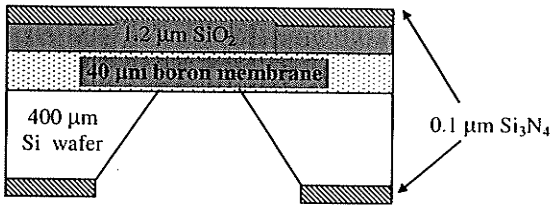

(b) the Si wafer after KOH etch to form Si diaphragm.

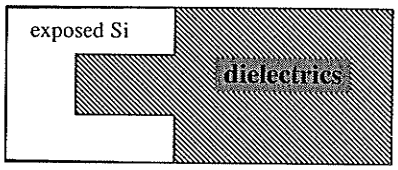

(c) the top view with exposed Si

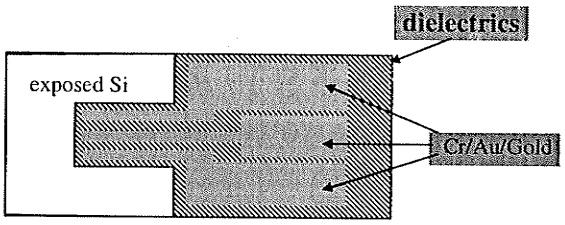

(d) depositing the Cr and Au and gold and then etch the metal layer to form the probe tip

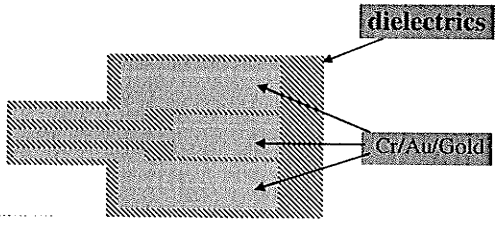

(e) the final probe tip is formed by etching the Si diaphragm from back in RIE to remove the exposed Si

Figure 5-4 The silicon wafer of CWP during the micromachining processing[62]

5.4 Conclusion

As shown in Figure 5-5, a micromachined cantilever was mounted to a CPW circuit. This created a near-field probe that was used to measure a Type B CPW transmission line (Figure 4-3). Unfortunately, the signal coupled to the probe was at noise level. The structure of the micromachined cantilever is the major reason to cause the problem. Since the signal line and the ground lines had the same length (Figure 5-2), there was no probe tip constructed. The probe has to be redesigned and fabricated in the future work. Other than that, the gap between the probe tip and the CPW circuit plane has also to be precisely controlled, and the vibration of such a tiny cantilever has to be reduced as much as possible.

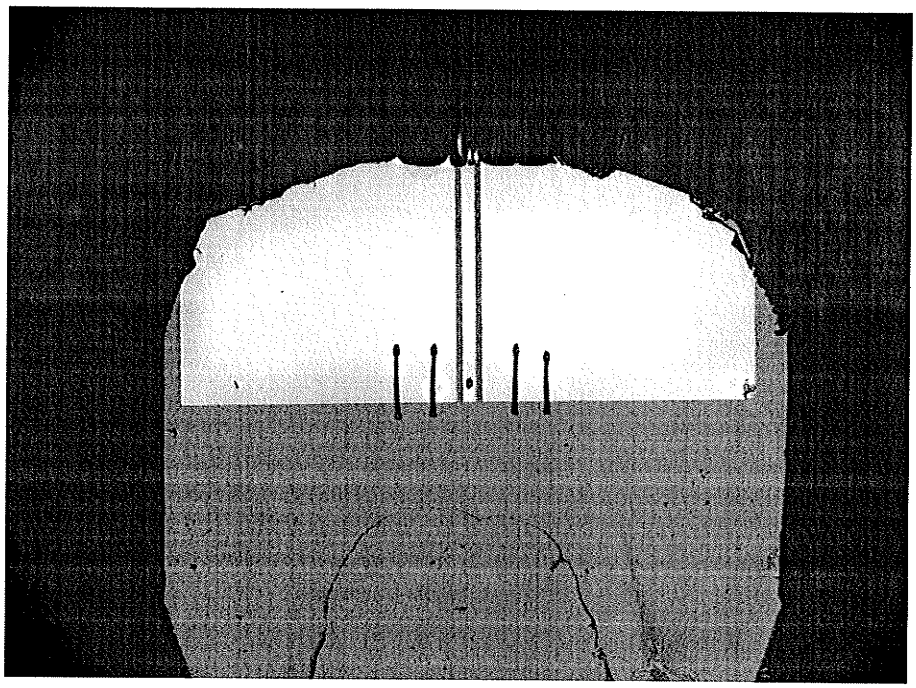

Figure 5-5 CPW probe made with the micromachined cantilever

Chapter 6 SIMPLE PCB MEASUREMENT WITH MAGNETIC LOOP PROBES

As an alternative to the electric field probing techniques, the magnetic near field variation has been studied in recent years, and techniques have been subsequently developed to measure the magnetic near field produced by a radiating structure [28] [29] [30] . One of the developments is proposed for examining Printed Circuit Board (PCB) through non-contact means. Goulette etc. developed a system for testing electromagnetic emission and diagnosing faults in PBCs [55] [56] , the system comprises a planar sensor array of probes consisting of two serially connected wire loops aligned perpendicular to one another. The sensor array is positioned close to the energized board under test such that the magnetic field produced by the currents within board conductors will be picked up by the sensor element located in the proximity. Similarly, Soiferman [57] utilized an array of planar printed spiral loop antennas as the non-contact sensors for mapping the near-field patterns of bare PCBs. They both, for PCB failure detection, compare the near-field image pattern of board under test to a reference pattern obtained from known non-faulty boards.

This chapter is based on a set of experiment reports that was part of the investigation to determine detection capabilities of faults in Multi Layers Boards [58] [59] . The probe design is such that the magnetic field generated by sources (such as neighbouring lines) other than the printed line under test does not couple to the probe. Alternatively, printed lines directly under the probe couple efficiently with the probe, inducing currents which add constructively. The test set up is shown in Figure 6-1 which includes:

- Single-loop/four-loop probes made from a rigid coaxial cable, the inner conductive wire is coiled to form the ring(s). The ring diameter d_r is about 10 mm and the inner wire diameter d_w is about 0.5 mm.

- Wiltron network analyzer, which was used to energize and to collect the magnetically coupled signal to get the S21 forward transmission parameters.

- HP plotter, a scanning stage to drive the movable probe conducting 1D/2D scanning over the circuitry area.

- PC to control both network analyzer and plotter, and reading data from the network analyzer.

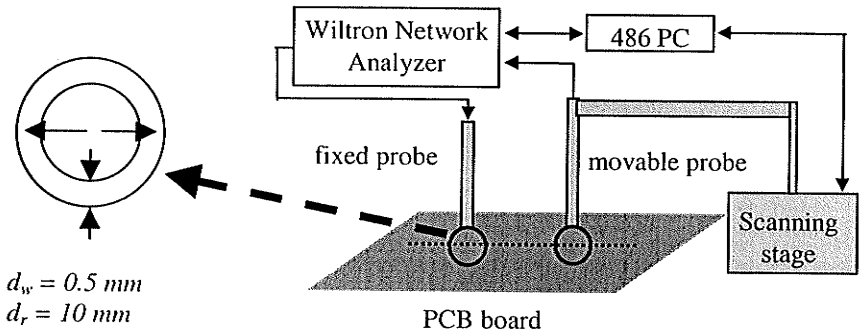

Figure 6-1 Test setup for PCB failure detection with magnetic probes

6.1 Near-field RF Inspection of PCBs

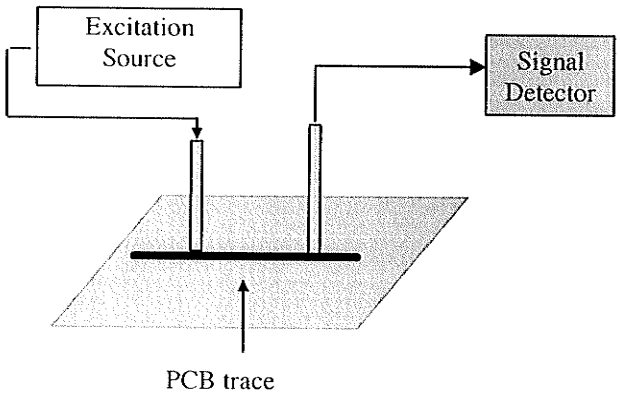

Figure 6-2 Traditional PCB fault detection with bed of nails

A traditional solution of PCB fault detection is a contact measurement as shown in Figure 6-2. It requires a bed of nails for excitation and signal detection, which turns out placement of too many switches and yield of low resolution.

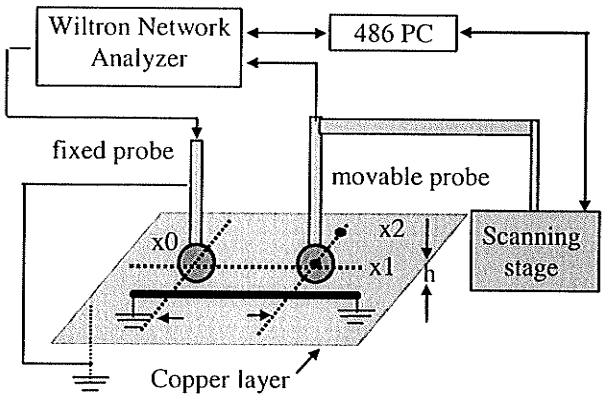

Figure 6-3 Illustration of indirect excitation

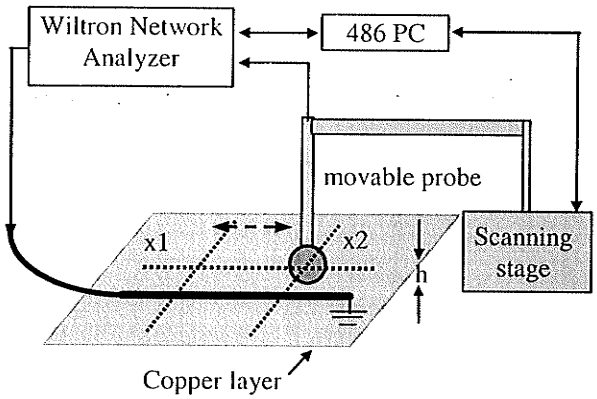

Figure 6-4 Illustration of direct excitation

Figure 6-3 shows the indirect excitation solution. Indirect excitation measurement induces currents on conducting paths on PCB by one of the loop pair, and generates magnetic near-field pattern by the other loop. Indirect sources don't need to touch

circuits. Indirect excitation has some drawbacks which are weak induced single and interfere due to direct source-loop coupling.

In contrast, direct excitation can induce currents on conducting paths on a printed circuit board as shown in Figure 6-4. The advantage of direct excitation is strong coupling signal. The drawbacks are that it needs to contact PCB and needs bed of nails for exciting.

6.2 Measurements on Indirect excitation

6.2.1 Magnetic Coupling between Loops over a PCB Ground Plane

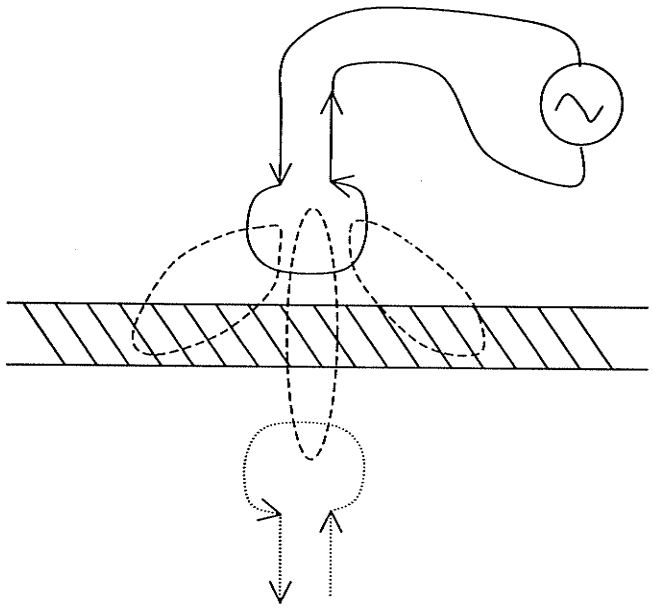

Figure 6-5 Indirect excitation over a ground plane

The purpose of the measurements conducted in this section is to investigate the effects of ground plane to indirect excitation. As shown in Figure 6-5, the ground plane

tends to repel the magnetic field away with the induced eddy-currents. However, the magnetic field can still go through the ground plane if the ground plane thickness is less than a few skin depths [60] . For copper the skin depth can be calculated by $\delta = \sqrt{2/\omega\mu\sigma}$, where $\omega = 2\pi f$, $\mu \approx \mu_0 = 4\pi\times10^{-7}$ Wb/m, and $\sigma \approx 5.8\times10^{7}$ S/m. The thickness of copper sheet on the PCB tested is about 17 μm for a ½ oz. cladding. When excited at 100 MHz, the skin depth of the copper sheet is about 6.6 μm, so the effect of ground plane can be modelled by perfect image current as shown in Figure 6-5.

Considering the scenario shown in Figure 6-6, two loop probes are placed over a PCB ground plane. One probe is sitting relatively at x_0, the other is movable and is moved from x_1 to x_2. The port 1 of network analyzer feeds the fixed probe for indirect excitation and the port 2 is connected to the movable probe for collecting magnetically induced signal. The ring surface normals are parallel. Provided that the left edge of PCB is marked as x = 0, the fixed probe is located at x_0 = 12 mm, the movable probe is scanning from x_1 = 25 mm to x_2 = 125 mm. Two loops are about h = 8 mm above the plane.

The equivalent circuit for Figure 6-6 is shown in Figure 6-7.

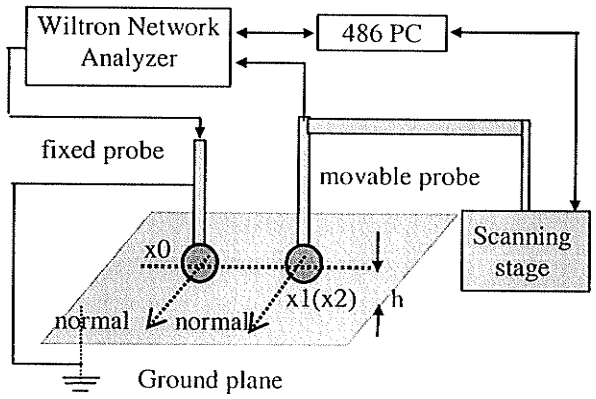

Figure 6-6 Two loop probes over a large ground plane, ring surface normals are parallel

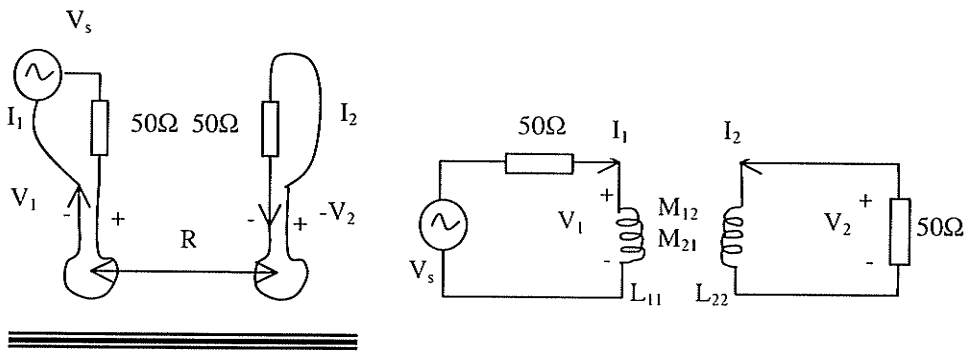

Figure 6-7 Equivalent circuit of two probes over a ground plane

The relations between V_1, V_2, I_1, I_2 can be expressed by the network theory as following,

$$\begin{bmatrix} V_1 \\ V_2 \end{bmatrix} = \frac{d}{dt}\begin{bmatrix} L_{11} & -M_{12} \\ -M_{21} & L_{22} \end{bmatrix}\begin{bmatrix} I_1 \\ I_2 \end{bmatrix} \tag{6-1}$$

the mutual inductance between loops is [61]

$$\begin{aligned} M_{21} = M_{12} &= -\frac{1}{I_1}\iint_{s_2} \bar{B}_{loop1}(\bar{r}')d\bar{s}' \\ &\approx -\frac{1}{I_1}\iint_{s_2}\left(\frac{\mu_0 A_1}{4\pi R^3}\right)\hat{n}_1\cdot\hat{n}_2\, d\bar{s}' \\ &\approx -\frac{\mu_0 A_1 A_2}{4\pi R^3}(\hat{n}_1\cdot\hat{n}_2) \end{aligned} \tag{6-2}$$

where R is the distance between two loops, A_1 and A_2 are the areas of two loops, and $\hat{n}_1$, $\hat{n}_2$ are the normals to loop 1 and loop 2, respectively.

Given the same geometry, the self inductance of each loop is [61]

$$L_{11} = L_{22} \cong \mu_0 r\left(\ln\frac{8\pi r}{d} - 2.45\right) \tag{6-3}$$

where r is the ring radius of loops and d is the wire diameter.

From the equivalent circuit in Figure 6-7, V_1 and V_2 can be calculated.

$$V_1 = \frac{j\omega L_{11}}{50 + j\omega L_{11}} V_s + \frac{50}{50 + j\omega L_{11}} j\omega M_{12} I_2 \tag{6-4}$$

$$V_2 = -50 I_2 = \frac{50}{50 + j\omega L_{22}} j\omega M_{21} I_1 \tag{6-5}$$

under unilateral approximation, which assumes loop 2 does not give any loopback coupling to the source circuit, loop1, we will have the approximation

$$I_1 \approx \frac{V_s}{50 + j\omega L_{11}} \tag{6-6}$$

substitute (6-6) into (6-5),

$$V_2 \approx -\frac{50}{50 + j\omega L_{22}} j\omega M_{21} \frac{V_s}{50 + j\omega L_{11}} \tag{6-7}$$

Hence, $S_{21} = V_2 / V_s$ can then be calculated with

$$S_{21} \approx -j\omega M_{21} \cdot \frac{50}{50 + j\omega L_{22}} \cdot \frac{1}{50 + j\omega L_{11}} \tag{6-8}$$

The above discussion does not take into account the effects of self-inductance and mutual inductance of the images. As shown in Figure 6-8, when considering the effects of

images, the self-inductance and mutual inductance equations (6-2) and (6-3) must be recalculated.

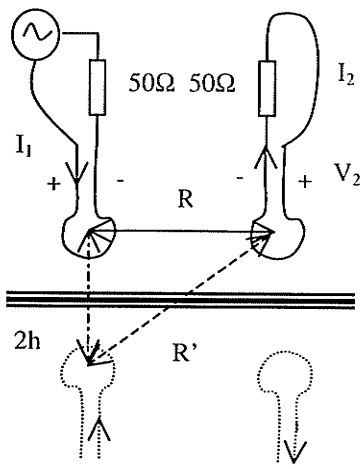

Figure 6-8 Two probes over a ground plane and their images

$$M_{21}^{image} \approx -\frac{\mu_0 A_1 A_2}{4\pi(\sqrt{R^2+(2h)^2})^3} \tag{6-9}$$

$$L_{11}^{image} \approx -\frac{\mu_0 A_1 A_2}{4\pi(2h)^3} \tag{6-10}$$

$$M_{21} \cong -\frac{\mu_0 A_1 A_2}{4\pi}\left(\frac{1}{R^3}-\frac{1}{(\sqrt{R^2+(2h)^2})^3}\right)(\hat{n}_1\cdot\hat{n}_2) \tag{6-11}$$

$$L_{11} \cong \mu_0 r\left(\ln\frac{8\pi r}{d}-2.45\right)-\frac{\mu_0 A_1 A_2}{4\pi(2h)^3} \tag{6-12}$$

Figure 6-9 shows both theoretical and experimental results of S_{21}. The calculations of either with the consideration of image effects (Equations (6-11) and (6-12)) or without

the consideration of current image effects (Equations (6-2) and (6-3)) are plotted. Regardless of the magnitude offset, the experimental result agrees well with the numerical result. Figure 6-9 also shows that S_{21} is at the noise level when the distance between two loops is greater than 50 mm, and there is minor magnetic coupling between them. When the distance is less than 50 mm, the inter-probe coupling (interfere) is dominant.

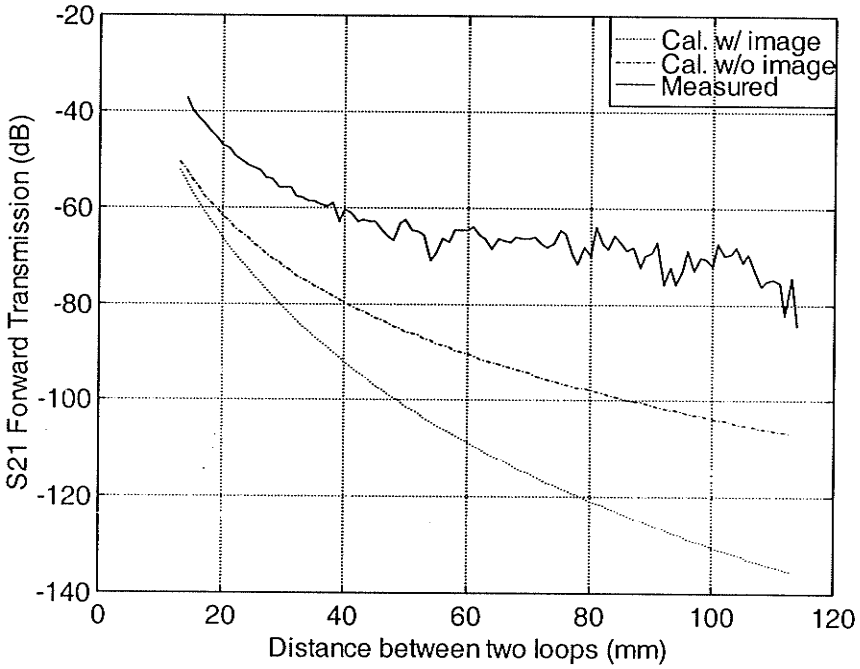

Figure 6-9 The numerical simulation vs. experimental data for two loops over a ground plane and ring surface normals are parallel

A measurement was also conducted for the scenario where ring surface normals are orthogonal, as shown in Figure 6-10. Similarly, the fixed probe was located at $x_0 = 12$ mm, the movable probe was scanning from $x_1 = 27$ mm to $x_2 = 127$ mm, two loops were at 8 mm above the circuit plane. The test result is shown in Figure 6-11. As expected from Equation (6-2), there was no magnetic coupling between two loops when their ring surface normals are perpendicular to each other, and S_{21} plot is at the noise level.

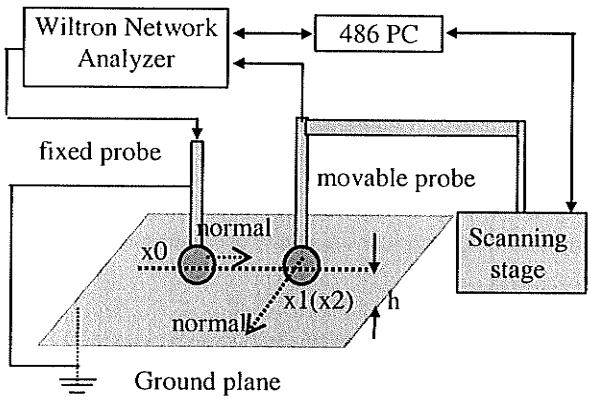

Figure 6-10 Two loop probes over a large ground plane, ring surface normals are orthogonal

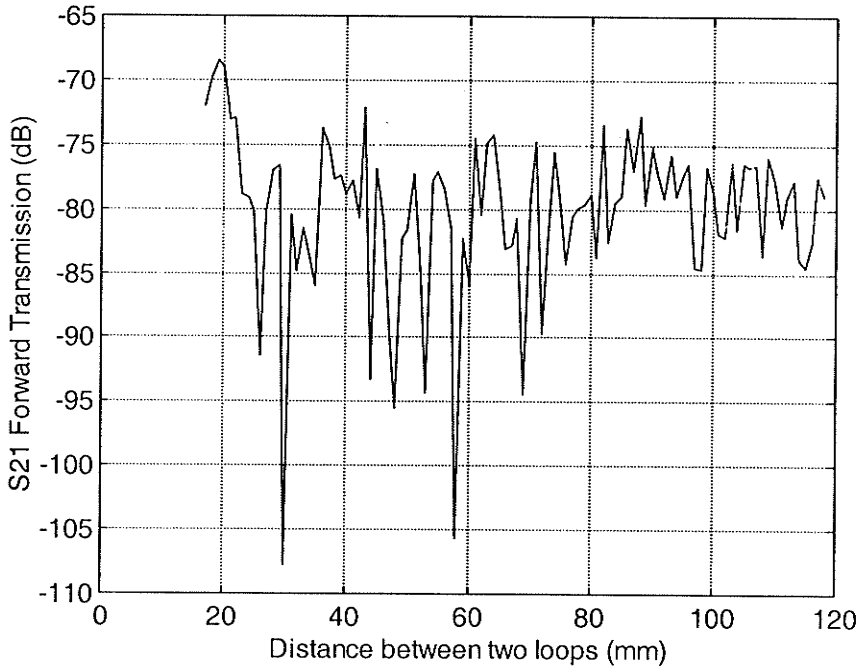

Figure 6-11 S_{21} plot for two loops over a ground plane and ring surface normals are orthogonal

Trying to enhance the performance of the measuring system, a multi-loop (four-loop) probe was also made and tested to be used as the movable probe. Measurements were

repeated with the four-loop probe for both configurations where normal vectors to ring surfaces are parallel and orthogonal. Unless mentioned, the setups are the same as shown in Figure 6-6 and Figure 6-10. The single-loop probe was fixed at $x_0 = 0$ mm, and the movable four-loop probe was scanning from $x_1 = 15$ mm to $x_2 = 115$ mm. Two probes were at 8 mm above the ground plane. Figure 6-12 and Figure 6-13 show the single loop probe vs. the four loop probe performance.

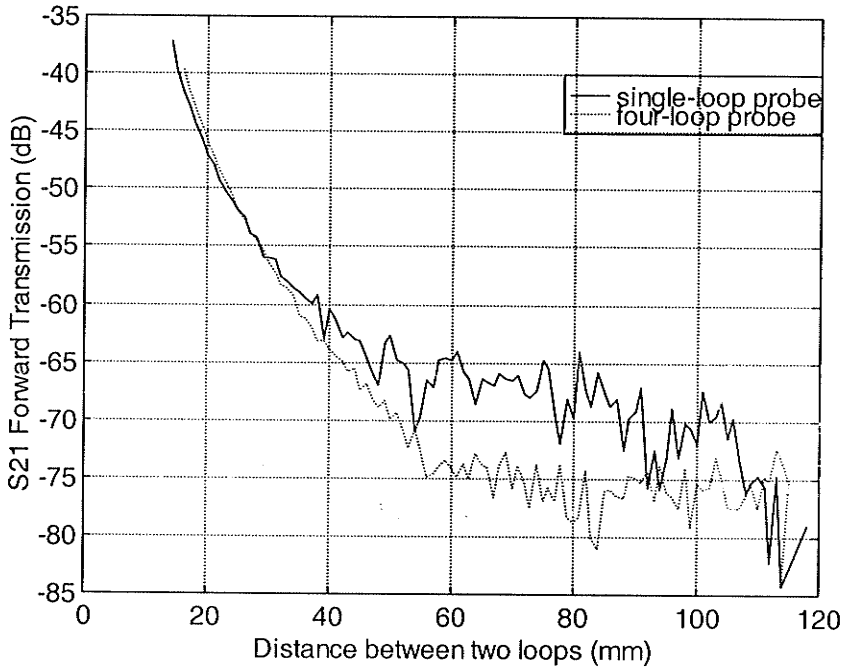

Figure 6-12 Performance comparison of single-loop and four-loop probes, ring surface normals are parallel

It is noticed in Figure 6-12 that the inter-probe coupling level between two single-loop probes does not change significantly by using a single-loop or a four-loop probe. Provided that the self-inductance of a single loop, i.e. loop 2 is L_{22} and the mutual inductance between two single loop, i.e. loop 2 and loop 1 is M_{21}, when loop 2 is replaced with an N toroid loop, i.e. $N = 4$, the self-inductance of the 4-loop probe will be N^2L_{22}, assuming that the loop 2 is an infinite thin wire loop. The mutual inductance

between loop 2 and loop 1 is now NM_{21}. Equation (6-8) can be rewritten for the four loop configuration.

$$S_{21}^{4loop} \approx -j\omega M_{21}^{4loop} \cdot \frac{50}{50 + j\omega L_{22}^{4loop}} \cdot \frac{1}{50 + j\omega L_{11}} \tag{6-13}$$

L_{22} turns out to be approximately 0.047 μH by Equation (6-3) given the ring parameters shown in Figure 6-1. The inductance $|j\omega L_{22}|$ of a single loop is roughly 30 Ω at frequency of 100 MHz. The S_{21} for both configurations can be calculated by Equation (6-8) and (6-13).

$$\begin{aligned} |S_{21}| &= |\omega M_{21}| \cdot \frac{50}{|50 + j\omega L_{22}|} \cdot \frac{1}{|50 + j\omega L_{11}|} \\ &= |\omega M_{21}| \cdot \frac{50}{\sqrt{50^2 + 30^2}} \cdot \frac{1}{|50 + j\omega L_{11}|} \\ &= 0.86|\omega M_{21}| \cdot \frac{1}{|50 + j\omega L_{11}|} \end{aligned} \tag{6-14}$$

$$\begin{aligned} |S_{21}^{4loop}| &= |\omega M_{21}^{4loop}| \cdot \frac{50}{|50 + j\omega L_{22}^{4loop}|} \cdot \frac{1}{|50 + j\omega L_{11}|} \\ &= 4|\omega M_{21}| \cdot \frac{50}{|50 + j16\omega L_{22}|} \cdot \frac{1}{|50 + j\omega L_{11}|} \\ &= |\omega M_{21}| \cdot \frac{200}{\sqrt{50^2 + 480^2}} \cdot \frac{1}{|50 + j\omega L_{11}|} \\ &= 0.41|\omega M_{21}| \cdot \frac{1}{|50 + j\omega L_{11}|} \end{aligned} \tag{6-15}$$

In actual loop probe design, the wire cannot be infinitely thin and hence the self inductance L_{22} will be between N^2L_{22} and NL_{22}. The $|S_{21}{}^{4loop}|$ will then be closer to $|S_{21}|$. This gives an approximate explanation to measurement result in Figure 6-12.

Note that from Equation (6-15), S_{21} is very sensitive to L_{22} value accuracy, in another words, is sensitive to the value of ωL_{22} vs. Z_0. If $\omega L_{22} << Z_0$, then the inter-loop coupling will increase 4 times (~ +12 dB), while the coupling will decrease 4 times (~ -12 dB) if $\omega L_{22} >> Z_0$.

Figure 6-13 shows the result when normal vectors to ring surfaces are orthogonal. As expected from Equation (6-2) there is no coupling between two loops and S_{21} plot is at the noise level for this test configuration.

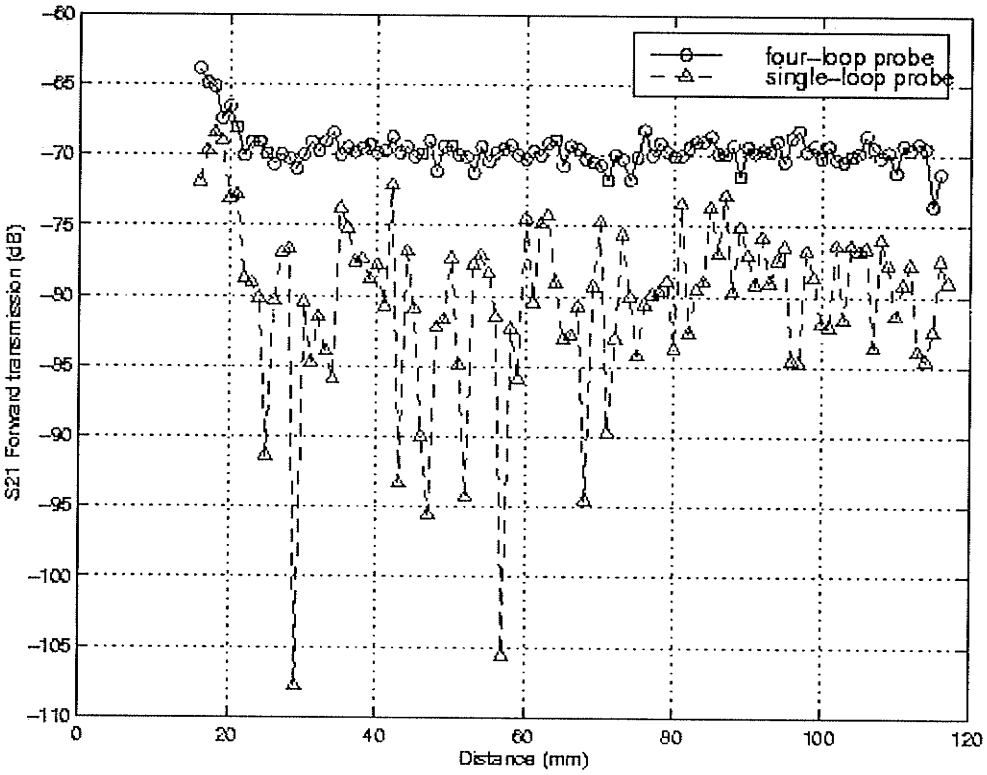

Figure 6-13 Performance comparison of single-loop and four-loop probes, ring surface normals are orthogonal

6.2.2 Magnetic Coupling between loops over a PCB Trace with Both Ends Shorted to Ground

This section will investigate the feasibility of using two loop probes to detect PCB trace failure. Instead of a large ground plane, a circuit board was used. This circuit board consists of a dielectric layer with dielectric constant $\varepsilon_r = 3.3$, a copper layer on one side as ground plane, and a 10 cm long by 1 mm wide circuit trace on the other side. Both ends of the trace were shorted to ground.

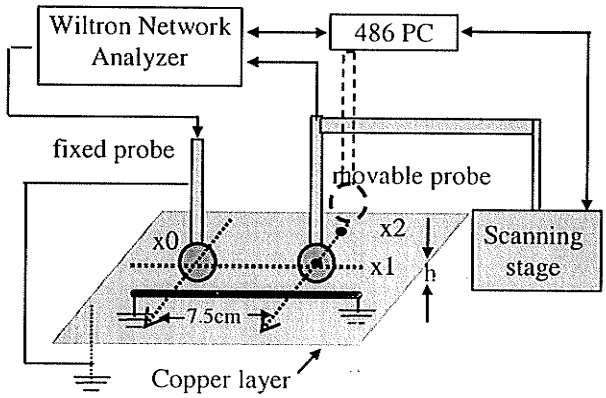

Figure 6-14 Two loop probes over the circuit trace with both ends shorted

6.2.2.1 Frequency Sweeping to Measure the Coupling Characteristic

As shown in Figure 6-14, two probes are at 8 mm above the circuit board. The fixed probe is at x_0, and the movable probe is at x_1 or x_2. Port 1 of network analyzer feeds the fixed probe for excitation, port 2 was connected to the movable one to collect the inductive coupling signal.

The sweeping frequency is from 40 MHz to 1000 MHz. Two measurements were taken for the movable probe at two spots x_1 and x_2 (Figure 6-14), x_1 is 7.5 cm away from x_0 along the trace, while x_2 is 2 cm away from x_1 along the ring surface normal.

As shown in Figure 6-15, plot A is the measurement of movable probe being at x_1 and plot B is for the measurement at x_2. The peaks around -50 dB are the trace resonant frequencies. The first resonant frequency is at about 300 MHz. When $f < 300$ MHz, the wavelength is less than 1 m, there will be no resonance, so the trace can then be treated as lumped coil (loop) inductive element. If $f > 300$ MHz it will see line resonance effects. Hence, the operation should be in quasi-static region, for which frequency is less than 250 MHz to have the inter-loop coupling measured independent of trace resonance.

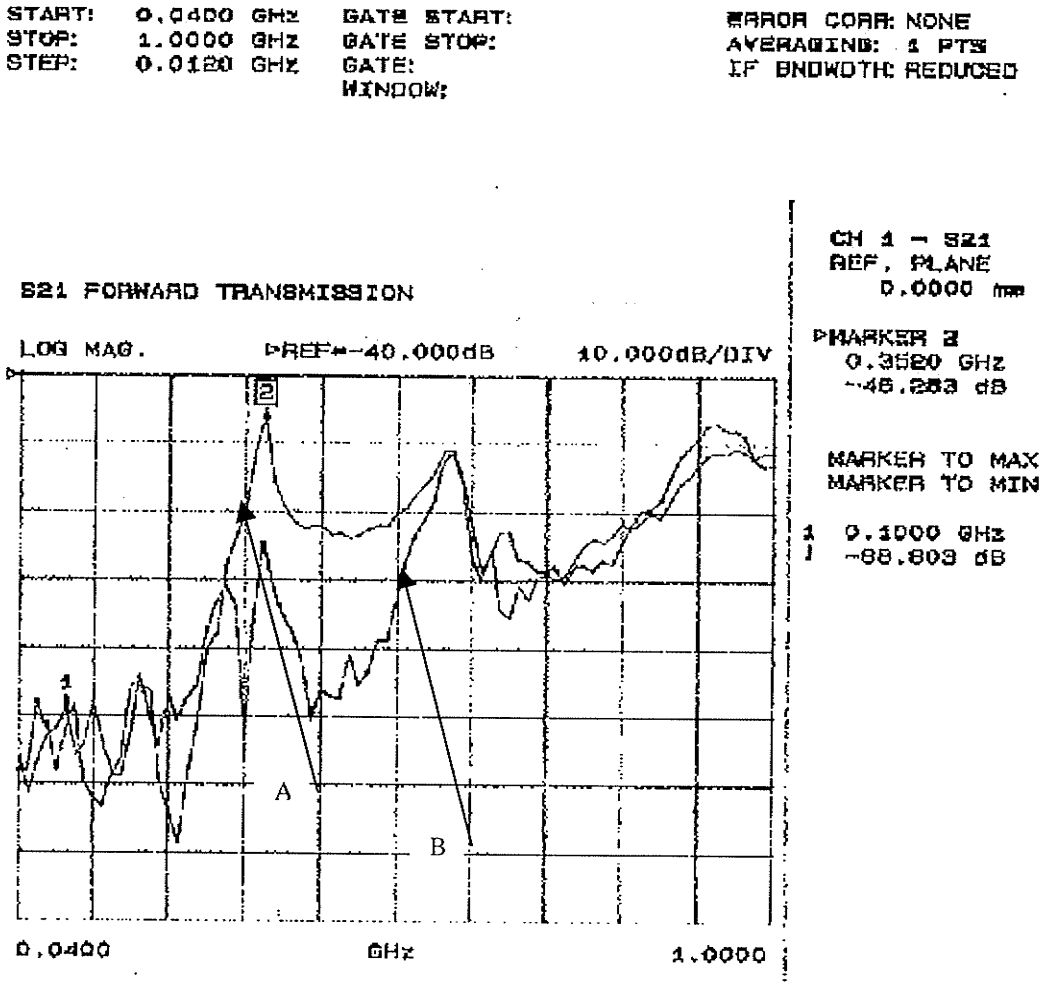

Figure 6-15 Frequency sweeping results by two single-loop probes

6.2.2.2 Scanning along the PCB Trace

When two conductive wire loops are right over a trace, as shown in Figure 6-16, the relations between V_1, V_2, V_t and I_1, I_2, I_t can be written as,

$$\begin{bmatrix} V_1 \\ V_2 \\ V_t \end{bmatrix} = \frac{\partial}{dt} \begin{bmatrix} L_{11} & M_{12} & M_{1t} \\ M_{21} & L_{22} & M_{2t} \\ M_{t1} & M_{t2} & L_{tt} \end{bmatrix} \begin{bmatrix} I_1 \\ I_2 \\ I_t \end{bmatrix} \tag{6-16}$$

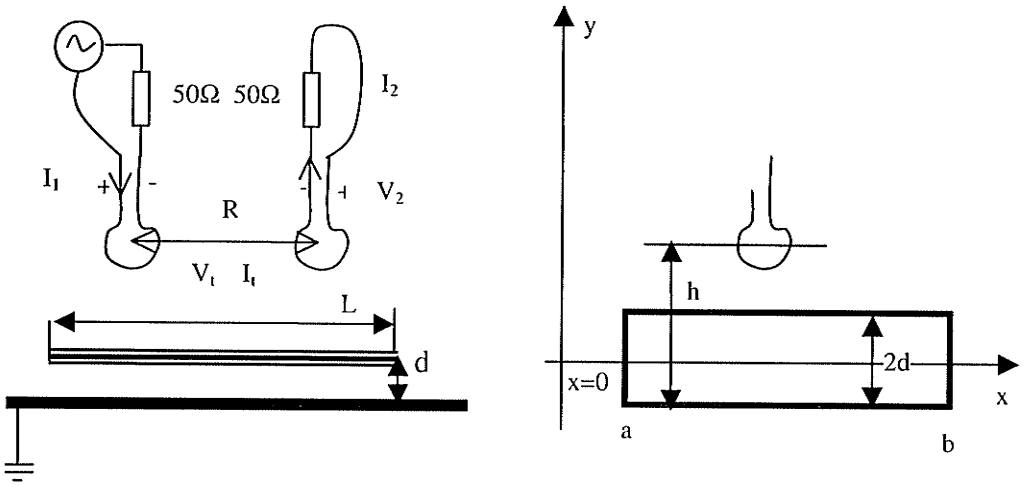

Figure 6-16 Two loops over a PCB trace

For case that excited frequency is well below the resonance frequency, $f < 300$ MHz, the PCB trace can be treated as a lumped parameter device by ignoring the distributed nature of the transmission line and thus can be modelled as a single loop. The inductance of the loop is L_t and loop area is $2d \cdot L$.

Since the trace is shorted to ground, $V_t = 0$, hence

$$0 = \frac{\partial}{dt}\left[M_{t1} I_1 + L_{tt} I_t\right] \Rightarrow \qquad I_t = -\frac{M_{t1} I_1}{L_{tt}} \tag{6-17}$$

given that $M_{2t} \cong M_{t1}$,

$$V_{ind}^{loop2} = -j\omega M_{t2} I_t = \frac{j\omega M_{t1}^2 I_1}{L_{tt}} \tag{6-18}$$

$$V_2 = \frac{50}{50 + j\omega L_{22}} V_{ind}^{loop2} \tag{6-19}$$

$$S_{21} = \frac{V_2}{V_s} = \frac{j\omega M_{t2}^2}{L_{tt}} \cdot \frac{50}{50 + j\omega L_{22}} \cdot \frac{1}{50 + j\omega L_{11}} \tag{6-20}$$

where L_{tt} is the inductance per unit length of microstrip t-line, and

$$M_{t2} = \frac{\mu_0 A_2}{4\pi} \int_a^b \frac{2d}{(\sqrt{x^2 + h^2})^3} dx = \frac{\mu_0 A_2}{4\pi} \frac{2d}{h^2 \sqrt{x^2 + h^2}} \Bigg|_a^b \tag{6-21}$$

From Equation (6-20), as the substrate thickness d is in order of 1 mm, much less than the distance h (about 8 mm) between the loop and the trace, and also much less than the PCB trace length L, the value of M_{t2} can be approximately estimated to be a very small value. This will be demonstrated in the experiments that follow.

Figure 6-17 shows the numerical result of magnetic coupling between the PCB trace and the loop probe by Equation (6-20). Provided that L_{tt} is in order of 100 nH for the PCB trace under test, the magnetic coupling is very small at -76 dB level.

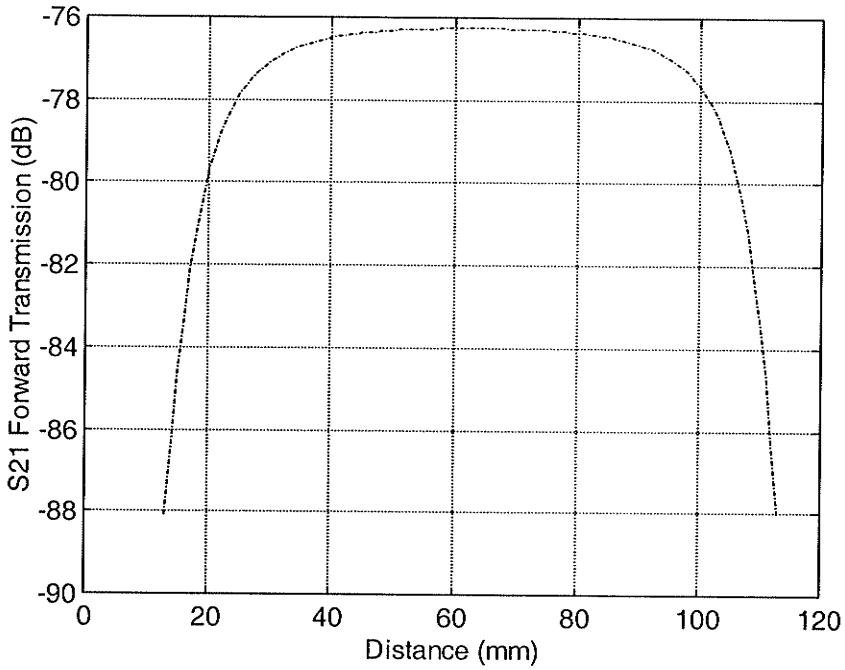

Figure 6-17 Calculated magnetic coupling between the PCB trace and the movable loop probe

Similar to the experimental investigation done in 6.2.1, both single loop and four-loop movable probe were used for measurement of the PCB trace. The fixed probe was at x_0 = 1.0 cm, the movable probe was scanning from x_1 =2.6 cm to x_2 = 9.5 cm. These two loops were 0.8 cm high right above the circuit trace. Figure 6-18 shows the measurement results when two ring surface normals were parallel. There is a 3-4 dB enhancement when using a four-loop probe in place of a single-loop probe. The S_{21} plot is at noise level when the distance between two probes is greater than 50 mm, and there is minor magnetic coupling between them. While the distance is less than 50 mm, the inter-probe coupling (interfere) is dominant.

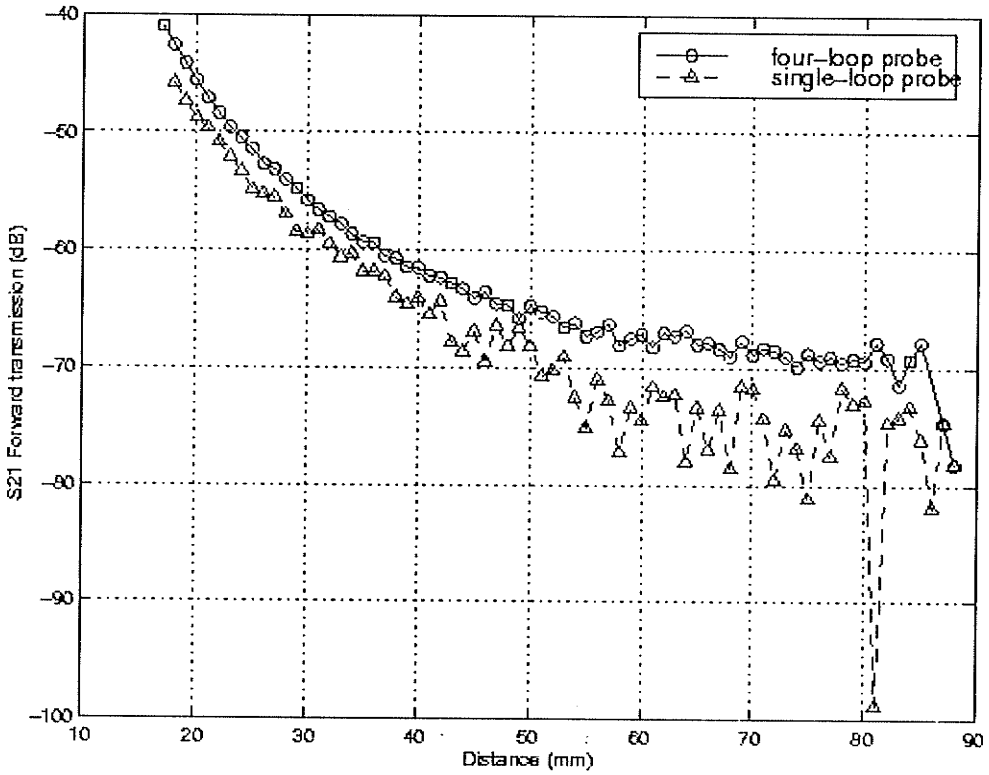

Figure 6-18 Performance comparison of single-loop and four-loop probes scanning along the trace, ring surface normals are parallel

Measurement was also conducted for scenario that ring surface normals were orthogonal. Figure 6-19 shows there was minor coupling between loops and between loops and trace.

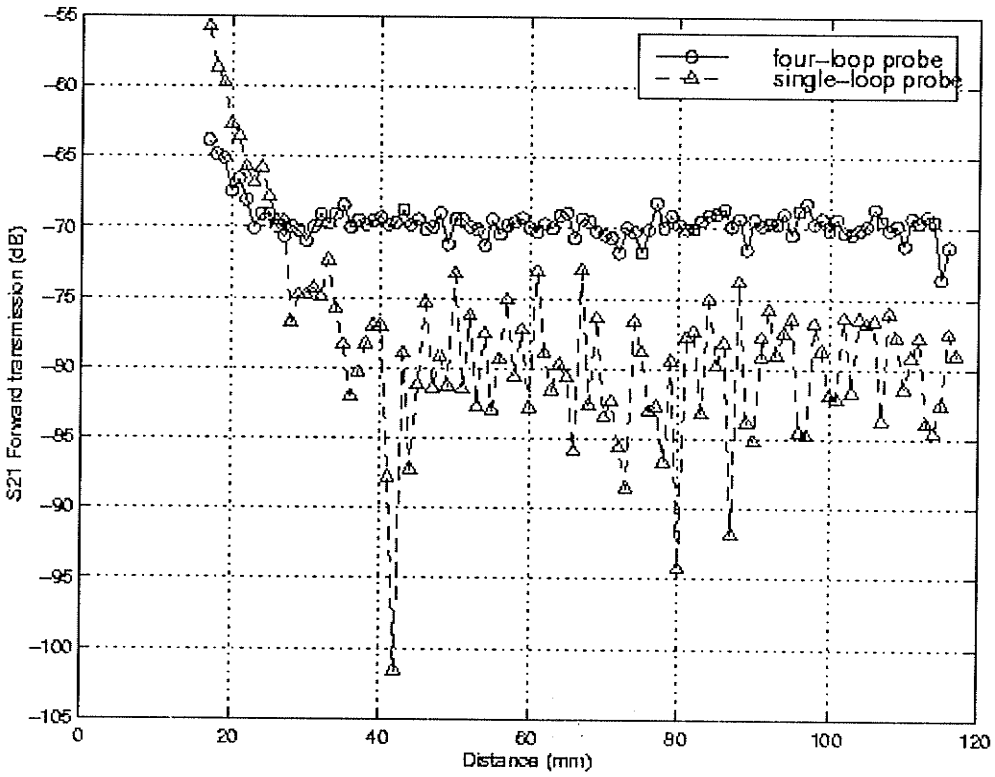

Figure 6-19 Performance comparison of single-loop and four-loop probes scanning along the trace, ring surface normals are orthogonal

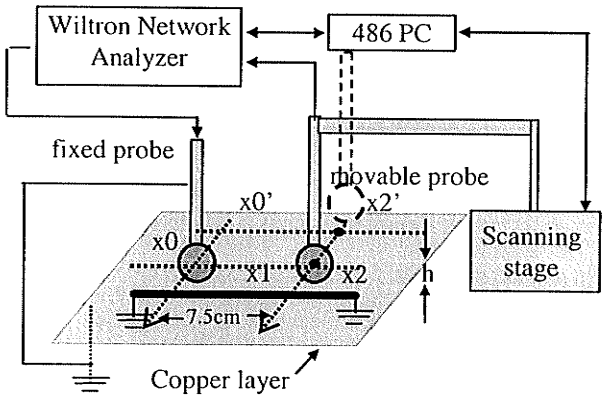

Figure 6-20 Scanning along the path aside from but parallel to the trace

To investigate the coupling level of scanning right over the trace from that of scanning along a path aside from but parallel to the trace, a measurement also was conducted as shown in Figure 6-20. In the measurement two loops right over the circuit trace, the fixed probe was located at x_0 = 3.6 cm, the movable probe was scanning from x_1 = 5.3 cm to x_2 = 12.3 cm. These two loops were directly over the trace at height of h = 0.8 cm.

In the test that two loops were both 3.5 cm away from the trace, the fixed probe was located at x_0' = 5.3 cm, the movable probe was scanning from x_1' = 7.0 cm to x_2' = 14.0 cm. Figure 6-21 shows the scanning results of the S_{21} forward transmission ratio versus the distance between the fixed loop and the movable loop.

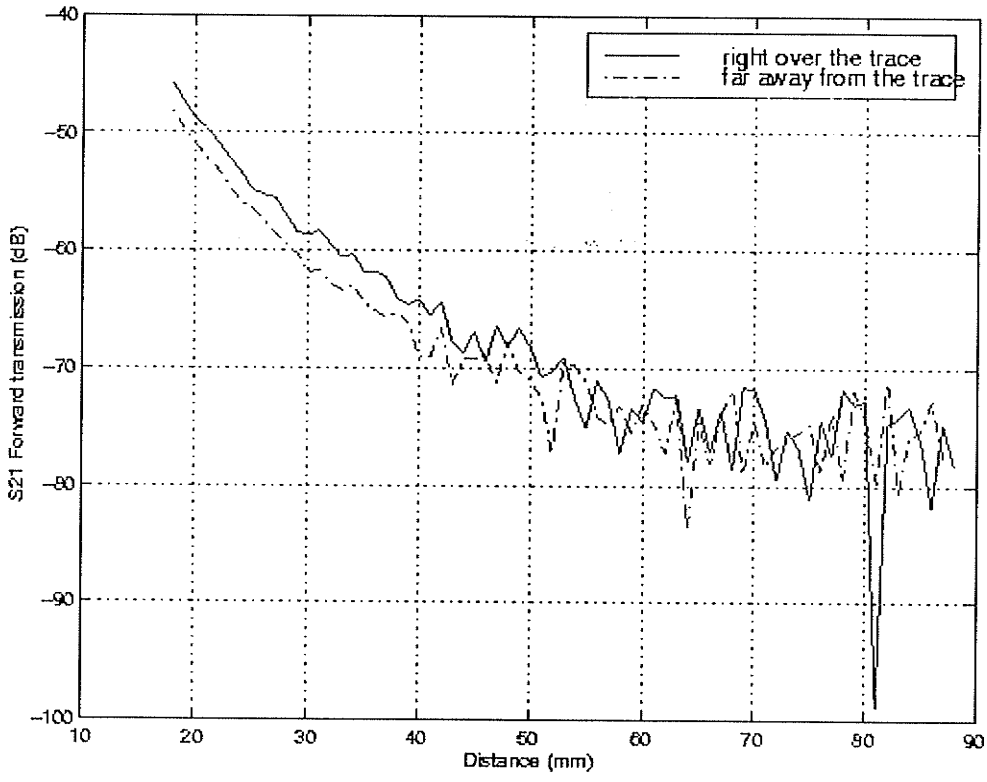

Figure 6-21 Distance scanning results by two single-loop probes in the case of circuit trace with each end short circuited

6.3 Measurement on Direct excitation

This section will discuss some measurement results on direct excitation. As shown in Figure 6-22, only one single-loop probe was used in the measurement. The circuit board is the same as that used in 6.2. The port1 of network analyzer was directly connected to one of the trace ends, and the port2 was connected to the movable probe to collect the coupling signal from the trace. The other end of the circuit was short circuited. Two measurements were conducted for this configuration:

- Frequency sweeping to measure the coupling characteristic versus the stimulus frequency.
- Transverse scanning over the circuit trace.

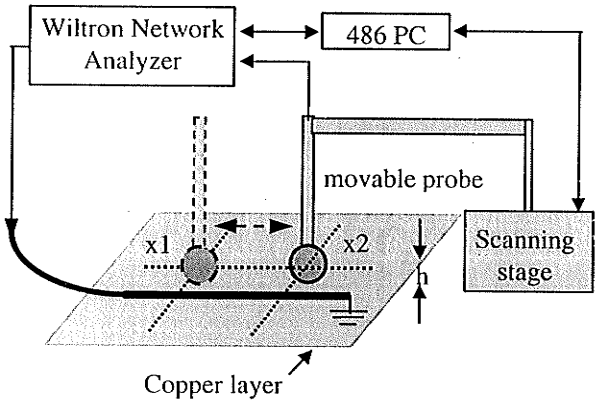

Figure 6-22 Measurement on direct excitation

6.3.1 Frequency Sweeping to Measure the Coupling Characteristic

The frequency sweeping measurement was taken at x_1 and x_2 (Figure 6-22). x_1 is 2.5 cm away from the signal feeding end, while x_2 is 7.5 cm away from the end. The loop was 0.7 cm high over the circuit trace. The sweeping frequency is from 40 MHz to 1000

MHz. As shown in Figure 6-23, Plot A is the result at x_1 and Plot B is the result at x_2. It is expected to see the similar results explained in 6.2.2.1.

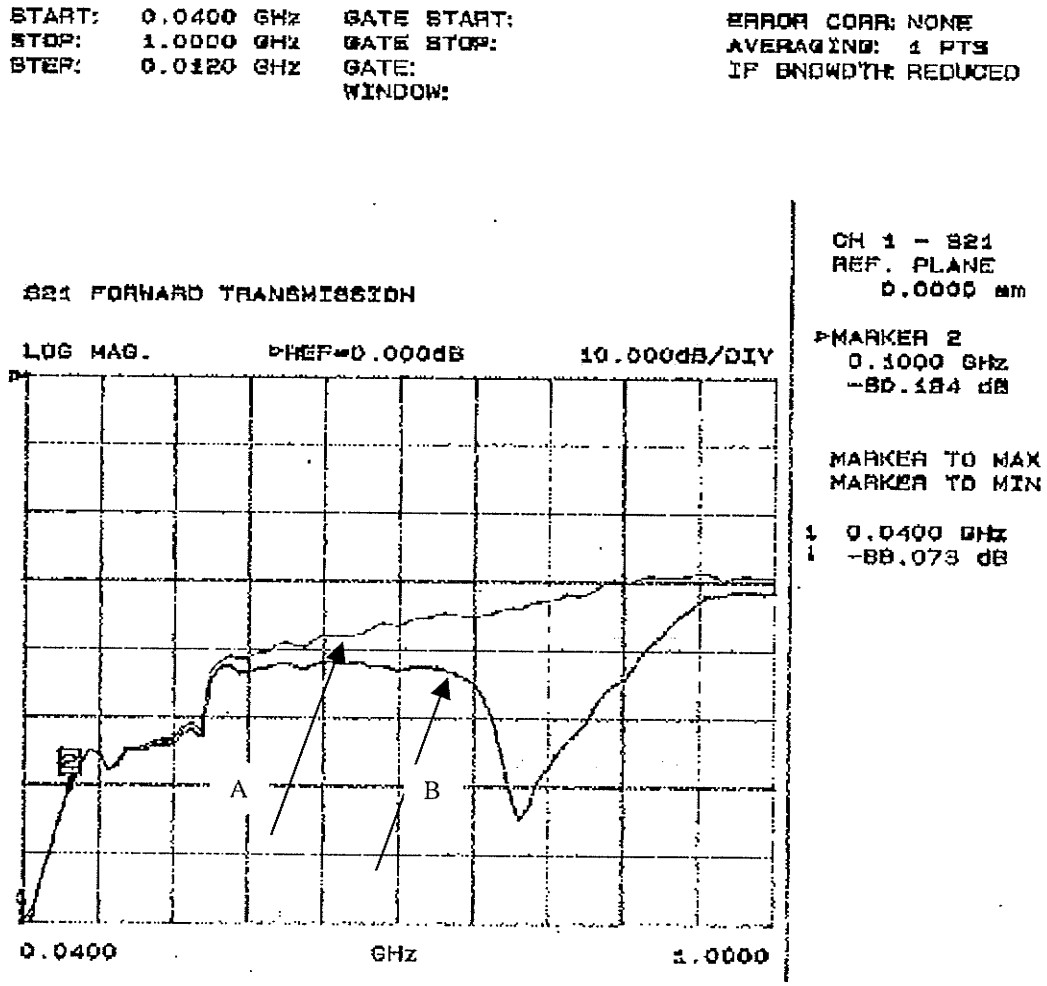

Figure 6-23 Frequency sweeping for a single-loop probe from 40 MHz to 1000MHz

Figure 6-24 is a zoomed-in plot for 40 MHz $< f <$ 200 MHz.

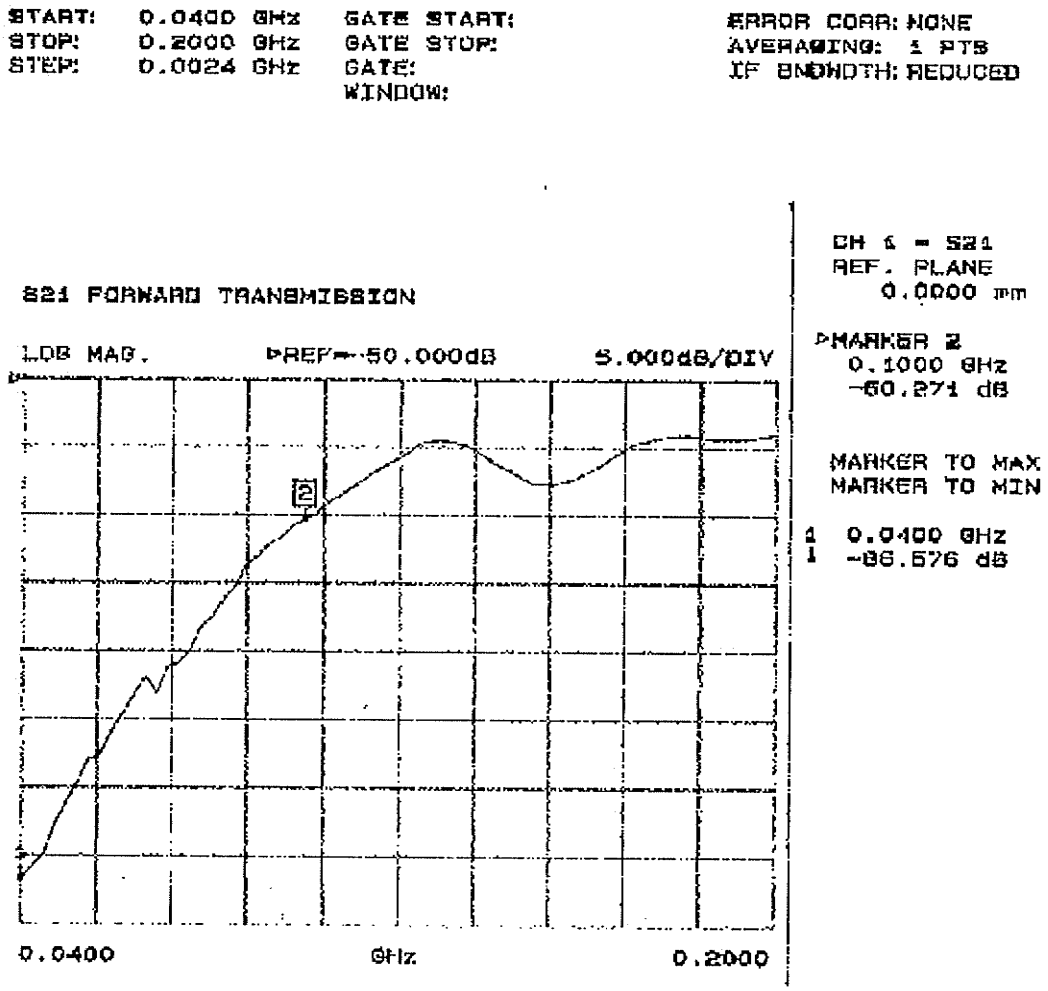

Figure 6-24 Frequency sweeping for a single-loop probe from 40MHz to 200MHz

6.3.2 Transverse Scanning across the PCB Trace

Transverse scanning over circuit trace with a single loop probe for direct excitation was conducted as shown in Figure 6-25. The intersection x_1 of the scanning path and circuit trace was 2.5 cm away from the signal feeding end. The scanning range was 10 cm, 5 cm aside on each side of the trace.

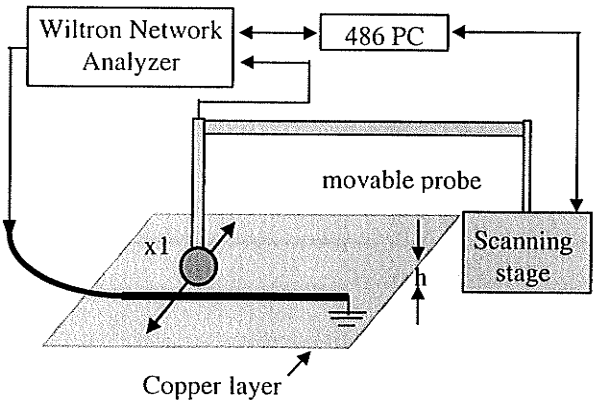

Figure 6-25 Transverse scanning across the circuit trace

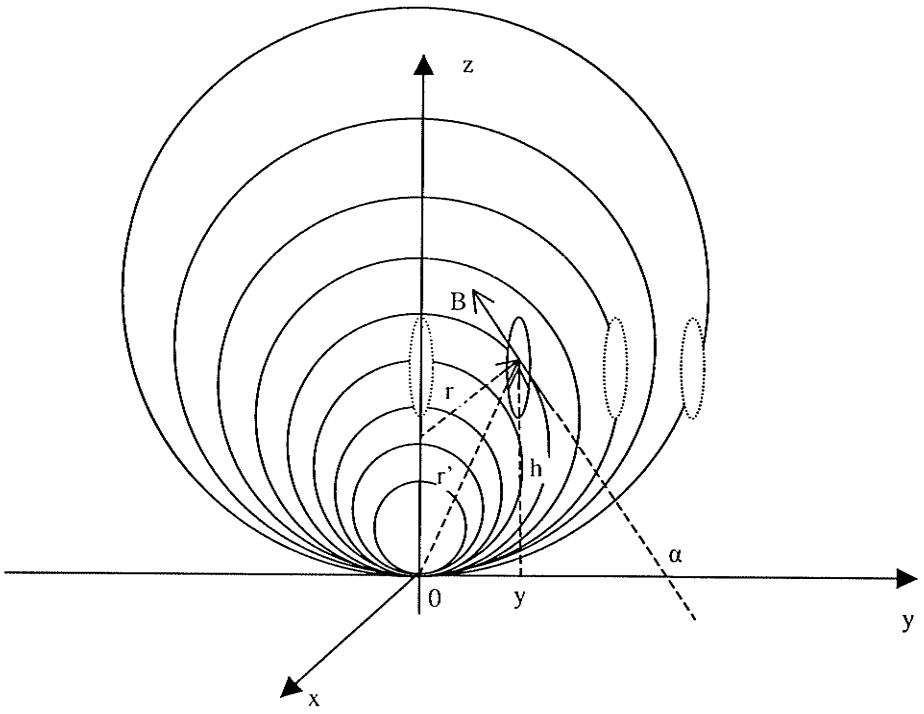

Figure 6-26 An approximate model for magnetic field calculation without consideration of image current effect

An approximate magnetic field distribution over the PCB surface is shown in Figure 6-26 when looking at the cross section of the PCB trace. With the consideration of image

current effect, the closed magnetic field curls in the very near field region can be considered approximately as a group of circles having a common tangential line at point (y = 0, z = 0). Provided that the electric current is along x axis, the y component B_y of the magnetic field B at the central point of the loop can be formulated when the probe is at y.

$$B_y = \frac{\mu_0 I}{2\pi r'}\cos\alpha \tag{6-22}$$

where I is the current in circuit trace, r' is the distance between the central point of the loop and circuit trace, and α is the angle formed by the vector B and y axis.

For a closed magnetic field curl, the radius r is

$$r = h + \Delta z = \sqrt{y^2 + (\Delta z)^2} \tag{6-23}$$

Δz can then be expressed as

$$\Delta z = \frac{y^2 - h^2}{2h} \tag{6-24}$$

Substitute Δz in (6-23) with (6-24),

$$r = h + \Delta z = \frac{y^2 + h^2}{2h} \tag{6-25}$$

Hence,

$$B_y = \frac{\mu_0 I}{2\pi\sqrt{y^2 + h^2}}\cos\alpha = \frac{\mu_0 I}{2\pi\sqrt{y^2 + h^2}}\frac{y^2 - h^2}{y^2 + h^2} \tag{6-26}$$

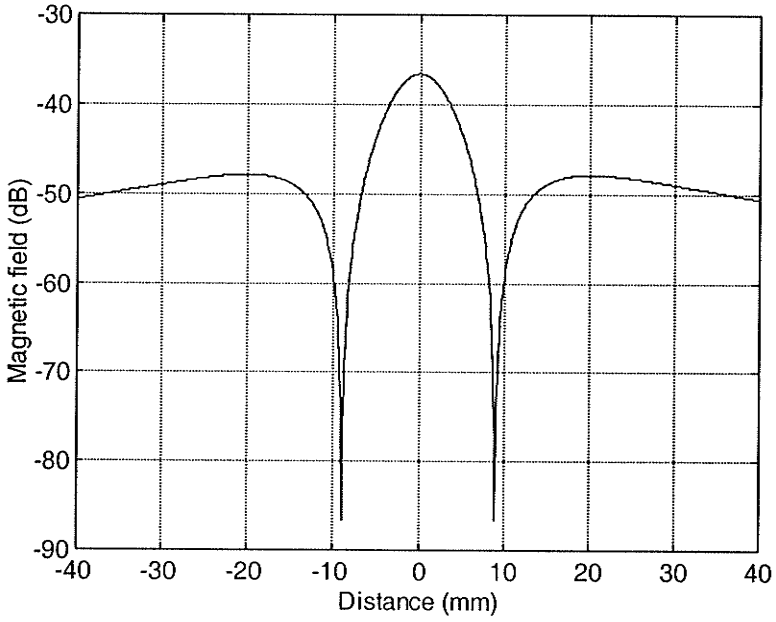

Figure 6-27 Simulation result of transverse scan over the circuit trace with a single-loop probe

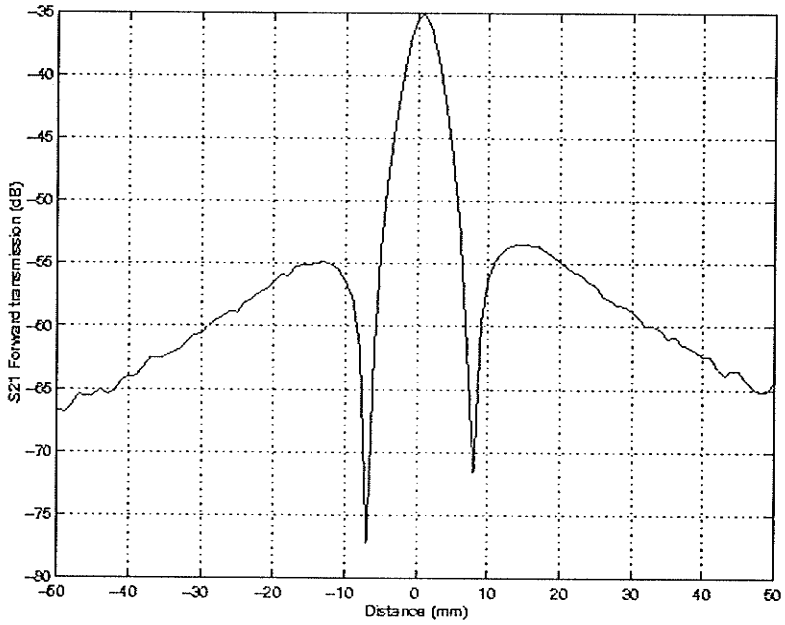

Figure 6-28 Measurement result of transverse scan over the circuit trace with a single-loop probe

Figure 6-27 is the magnitude plot of B_y calculated by (6-26). The coupled current signal to the probe will be proportional to B_y. Figure 6-28 is the measurement result. With the assumptions for the very near field region the measurement result agrees with the simulated result.

6.4 Conclusion

In this chapter, both indirect and direct excitation measurements with magnetic probes were investigated as an alternative to capacitively coupled probing technique. Frequency sweeping performed indicated that to eliminate trace resonance at high frequency where PCB traces cannot be treated as lumped coil (loop) inductive elements, the measurement with magnetic probes can be only done at frequency lower than 300 MHz.

The measurement and simulation results also illustrated that in the indirect excitation measurement, the inter-probe coupling (interfere) is dominant when two probes were close to each other. Increasing the loop coil number of probe did not enhance the performance very much, for instance, using a four coil loop was giving a 3dB performance enhancement.

Chapter 7 CONCLUSIONS

The feasibility of the applications of electromagnetically coupled probes as diagnostic tools for a broad range of microwave circuits has been investigated. Unlike a traditional circuit measurement technique, non-contact near-field probes are much less likely to disturb the normal operation of the device under test at Gigahertz frequency.

An automated near-field probing system has been designed and built capable of producing information unavailable from conventional measurement techniques. A system transfer model was created to prove that the transfer function of device under test can be obtained provided that the transfer function of near-field probe is derivable from modelling. By using a method of moment (MOM) solution, T. Forzley has given a approximate model for various heights of the probe above the transmission line and incremental displacements relative to the center of the transmission line [5] . The system hardware and software were built in a module-oriented manner such that the system was flexible and scalable to facilitate testing on wide range of microwave devices. The system is capable of one-dimension and two-dimension scanning for mm and μm resolution applications. The software developed based on LabView® is user friendly and capable of communicating to various measurement instruments, i.e. Network Analyzer, Spectrum Analyzer and Oscilloscope.

Various microwave devices have been tested by monopole and CPW probes with the automated near-field scanning system. The performance of both monopole and CPW probes were investigated by measuring CPW transmission lines. To verify the measurement results, CPW transmission line analysis was performed. The transverse electric field variation of CPW transmission line was modeled by solving the Laplace boundary value (BV) problem using a finite difference MOM approach with a SOR Iterative Matrix Solver [40] . The longitudinal electric field variation modelling was

performed by traditional transmission line theory. Both transverse and longitudinal scan over the CPW transmission lines were conducted and the results were compared with the numerical models. The test results recommend that the CPW probe and monopole probe have a comparable measurement performance, thus micron-meter electric near-field probes can be fabricated in a form of planar structure through the micromachining process to improve the spatial resolution. In addition, the probes were also used to measure the GHz single patch antennas and microstrip antenna arrays. The test results illustrate further proof to the feasibility of electric near-field probe application.

As an alternative to the electric near-field probing technique, the magnetic near-field probing has been also investigated to determine detection capabilities of faults in Multi Layers Boards [58] [59] . The signal frequency in such applications is limited up to 300 MHz range, and strong coupling between magnetic probes has been found to have considerable impact on the performance of this near-field measurement approach

A micromachined electric near-field probe designed and fabricated at Alberta Microelectronics Centre has been evaluated at scale less than 100 um measurement. The electric coupling between the probe and the transmission line under test was not strong enough and data acquired was at noise level. This was mainly due to the structure of the micromachined cantilever. There was no probe tip constructed since the signal line and the ground lines had same length. The probe has to be redesigned and fabricated in the future work. Other than that, the gap between the cantilever and the CPW circuit plane has also to be precisely controlled, and the vibration of such a tiny cantilever has to be reduced as much as possible.

REFERENCES

[1] B. T. Rosner, D. W. van der Weide, "High-frequency near-field microscopy", Review of Scientific Instruments, Vol. 73, No. 7, July 2002, pp.2505-2525

[2] N. Richardson, "E-beam probing for VLSI circuit debug", VLSI System design, Vol. 8, Aug, 1987, pp.24

[3] W. T. Lee, "Engineering a device for electron-beam probing", IEEE design and test of Computers, June 1989, pp.36-48

[4] H. Todokoro, S. Fukuhara, and T. Komoda, "Electron-beam LSI tester," Japan annual reviews in electronic, computers and telecommunications, Vol. 13, edited by J. Nishizawa, North-Holland, 1984, pp.373-382

[5] T. S. Forzley, "Non-Invasive Diagnostics of Microwave Integrated Circuits Using a Scanning Near-Field Probe", M.Sc. thesis, Department of Electrical and Computer Engineering, University of Manitoba, 1992

[6] K.Ura and H. Fujioka, "Function testing of semiconductor devices with stroboscopic scanning electron microscope", Japan annual reviews in electronics, computers and telecommunications, edited by J. Nishizawa, North-Holland, 1982, pp.308-327

[7] G. E. Bridges and D. J. Thomson, "High-frequency circuit characterization using the AFM as a reactive near-field probe", Ultramicroscopy 42-44, 1992, pp.321-328

[8] G. E. Bridges, T. S. Forzley, and D. J. Thomson, "Novel near-field probe for on-wafer intergrated circuit measurements", Microeletronics Journal, Vol. 23, No. 5, 1992, pp.363-369

[9] C. Böhm, C. Roths, E. Kubalek, "Contactless electrical characterization of MMICs by device internal electrical sampling dcanning-force-microscopy", IEEE MTT-S Digest 1994, pp.1605-1608

[10] D. W. van der Weide and P. Neuzil, "The nanoscilloscope: Combined topography and AC field probing with a micromachined tip", J. Vac. Sci. technol. B 14(6), Nov/Dec 1996, pp.4144-4147

[11] A. Leyk, C. Böhm, D. W. van der Weide, and E. Kubalek, "104 GHz signals measured by high frequency scanning force microscope test system," Electronics Letters, vol. 31, 1995, pp.1046-1047

[12] D. W. van der Weide, "Localized picosecond resolution with a near-field microwave/scanning-force microscope", Appl. Phys. Lett., Vol. 70, No. 6, 10 February 1997, pp.677-679

[13] R. A. Said, G. E. Gridges and D. J. Thompson, "Noninvasive scanned probe potentiometry for integrated circuit diagnostics," IEEE Transactions on Instrumentation and Measurement, Vol. 43, No. 3, June 1994, pp.469-474

[14] G. E. Bridges, R. A. Said, M. Mittal and D. J. Thompson, "High-frquency pattern extraction in digital integrated circuits using scanning electrostatic force microscopy," J. Vac. Sci. Technol. B 13(3), May/June, 1995, pp.1375-1379

[15] G. E. Bridges, R. A. Said, M. Mittal, and D. J. Thompson, "Sampled waveform measurement in integrated circuits using heterodyne electrostatic force microscopy," Rev. Sci. Instrum. 65 (11), Nov. 1994, pp.3378-3381

[16] R. A. Said, G. E. Gridges and D. J. Thompson, "High frequency potential probe using electrostatic force microscopy," J. Vac. Sci. Technol. A 12(4), Jul/Aug, 1994, pp.2591-2594

[17] D. Noruttun, G. Bridges, and etc., "Failure analysis of high speed microelectronics using non-contact probing," 1997 Micronet Annual Workshop, Ottawa, 1997, pp.53-54

[18] W. Mertin, A. Leyk, and etc., "Two-dimensional mapping of amplitude and phase of microwave fields inside a MMIC using the direct electro-optic sampling technique", IEEE MTT-S Digest 1994, pp.1597-1600

[19] G. David, W.Schroeder, and etc., "2D electro-optic probing combined with field theory based multimode wave amplitude extraction: a mew approach to on-wafer measurement", IEEE MTT-S Digest 1995, pp.1049-1042

[20] P. O. Müller, D. Erasme, and B. Huyart, "Wavelength oprimized electro-optic scanning of MMICs with fabry-perot enhancement", IEEE MTT-S Digest 1997, pp.1329-1332

[21] K. Yang, D. David, S. Robertson, J. F. Whitaker and L. P. B. Katehi., "High-resolution electro-optic mapping of near-field distributions in integrated mocrowave circuits", IEEE Microwave Theory and Techniques Digest, 1998, pp.949-952

[22] K. Yang, G. David, et al, "Electrooptic mapping and finite-element modeling of the near-field pattern of a microstrip patch antenna", IEEE Transactions on Microwave Theory and Techniques, Vol. 48, No. 2, February 2000, pp.288-294

[23] K. Yang, T. Marshall, et al, "Active-amplifier-array diagnostics using high-resolution electrooptic field mapping", IEEE Transactions on Microwave Theory and Techniques, Vol. 49, No. 5, May 2001, pp.849-857

[24] R. Reano, K. Yang, et al, "Simultaneous measurements of electric and thermal field utilizing an electrooptic semiconductor probe", IEEE Transactions on Microwave Theory and Techniques, Vol. 49, No. 12, December 2001, pp.2523-2531

[25] T. P. Budka and G. M. Rebeiz, "A microwave circuit electric field imager", IEEE MTT-S Digest 1995, pp.1139-1142

[26] T. P. Budka, E. M. Tentzeris and etc., "Near-field mapping above a coupled-line filter and a MMIC", Microwave Journal, March 1998, pp.94-106

[27] T. P. Budka, E. M. Tentzeris, and etc., "An experimental and theoretical comparison of the electric fields above a coupled line bandpass filter", IEEE MTT-S Digest 1995, pp.1487-1490

[28] S. S. Osofsky and S. E. Schwarz, "Design and performance of a non-contacting probe for measurements on high-frequency planar circuits", IEEE Transacrions on Microwave Theory and Techniques, Vol. 40, No. 8, August 1992, pp.1701-1708

[29] R.Grzybowski and R.Bansal, "Magnetic field probe for measuring surface current distribution on millimetre wave microstrip antennas," Electronics Lett., vol. 27, Jan. 1991, pp.71-73

[30] Y. Gao and I. Wolff, "A new miniature magnetic field probe for measuring three-dimensional fields in planar high-frequency circuits", IEEE Transacrions on Microwave Theory and Techniques, Vol. 44, No. 6, June 1996, pp.911-918

[31] J. S. Dahele and A. L. Cullen, "Electric probe measurements on microstrip", IEEE Transacrions on Microwave Theory and Techniques, Vol. MTT-28, No. 7, July 1980, pp.752-755

[32] Y. Gao and I. Wolff, "Miniature electric near-field probes for measuring 3-D fields in planar microwave circuits", IEEE Transacrions on Microwave Theory and Techniques, Vol. 46, No. 7, July 1998, pp.907-913

[33] Y. Gao and I. Wolff, "Calibration of Electric Coaxial Near-Field Probes and Applications", IEEE Transacrions on Microwave Theory and Techniques, Vol. 46, No. 11, November 1998, pp.1694-1703

[34] K. karrai and R. D. Grober, "Piezoelectric tip-sample distance control for near field optical microscopes", Appl. Phys. Lett., Vol. 66, No. 14, 3 April 1995, pp.1882- 1884

[35] T. Wei and X. D. Xiang, "Scanning tip microwave near-field microscope", Appl. Phys. Lett., Vol. 68, No. 24, 10 June 1996, pp.3506-3508

[36] S. Hubbell and D. J. Angelakos, "A technique for measuring the effictive dielectric constant of a microstrip line", IEEE Transacrions on Microwave Theory and Techniques, Vol. MTT-31, No. 8, August 1983, pp.687-688

[37] P. G. Frayne and J Whitehurst, "Mode analysis in radiating and no traiating planar open structures using a scanning microwave probe", 5th ICAP Conf., York, 1987, pp.501-505

[38] P. G. Frayne, "Handbook of Microstrip Antennas - Microstrip field diagnostics",

[39] E. Levine, "Handbook of Microstrip Antennas - Special measurement techniques for printed antennas",

[40] P. M. Knupp and S. Steinberg, "The fundamentals of grid generation", CRC Press LLC, 1993

[41] C. A. Balanis, "Antenna Theory: Analysis and Design," Second edition. John Wiley & Sons, 1997

[42] J. Zurcher and F. E. Gardiol, "Broadband Patch Antennas," Atrech House, 1995

[43] D. Gray, "Oversized elements for hig efficiency EHF boresight array", Ph.D. candidacy report, Department of Electrical and Computer Engineering, University of Manitoba, 2000

[44] A. Sebak, "Simulation of EM emissions from printed board traces", ANTEM'98-Symponium on Antenna Technology and Applied Electromaginetics, pp.585-588

[45] F. Lan, etc., "A new method for tapered open-ended coaxial line probe in determining relative complex permittivity at radio and micrewave frequencies", ANTEM'98-Symponium on Antenna Technology and Applied Electromaginetics, pp.497-500

[46] K. E. Petersen, "Sillicon as a mechanical material," Proc. IEEE, Vol. 70, No. 5, May, 1982, pp.420-457

[47] Gabriel M. Rebeiz, "Micromachining for microwave and millimeter-wave applications", ANTEM'98-Symponium on Antenna Technology and Applied Electromaginetics, pp.11-14

[48] Veljko Milanovic, ...etc. "Micromachined microwave transmission lines in CMOS technology", IEEE Transacrions on Microwave Theory and Techniques, Vol. 45, No. 5, May 1997, pp.630-634

[49] Kyung S. Oh, etc., "Computation of the equivalent capacitance of a via in a multi-layered board using the closed-form Green's function", IEEE Transacrions on Microwave Theory and Techniques, Vol. 44, No. 2, February 1996, pp.347-349

[50] B. J. Feenstra, etc., "Near-field scanning micrewave microscopy: measuring local microwave properties and electric field distributions", IEEE Microwave Theory and Techniques Digest, 1998, pp.965-968

[51] A. F. Lann, M. Golosovsky, and etc., "Mapping the thickness of conducting layers by a mm-wave near-field mocroscope", IEEE MTT-S Digest 1998, pp.1337-1340

[52] G. David, J. F. Whitaker, and etc., "DC-to-mm-wave absolute potential measurements insde digital micrewave ICs using a micromachined photoconductive sampling probe", IEEE MTT-S Digest 1998, pp.1333-1336

[53] M. Golosovsky and D. Davidov, "MM-wave near-field scanning resistuvity mocroscope", IEEE MTT-S Digest 1997, pp.1333-1334

[54] T. Pfeifer, H. M. Heiliger, and etc, "High-frequency on-wafer testing with freely prositionable silicon-on-sapphire photoconductive probes", IEEE MTT-S Digest 1995, pp.1053-1056

[55] R. R. Goulette, S. K. Xavier, and R. L. Greenfield, "Method and apparatus for monitoring electromagnetic emission level", Us Patent No. 4,829,238, May 9, 1989

[56] R. R. Goulette, S. K. Xavier, and R. L. Greenfield, "Method and apparatus for monitoring electromagnetic emission level", Us Patent No. 5,006,788, April 9, 1991

[57] J. Soiferman, "Contactless test method for testing printed circuit boards", US Patent No. 5,218,294, June 8, 1993

[58] R. Zhai, G. Bridges, "Experiment Report – investigation on detection capabilities of fults in Multi layers Boards", the Dept. of Electrical and Computer Engineering, the University of Manitoba, November, 1998

[59] Cirlog Inc. "MLB testing Capabilities", May, 1997

[60] H. C. Han, "A report on the evaluation of ATTI contactless PCB test system" 349 Durham Computation Center, Iowa State University, Sept. 7 1993

[61] M. N. O. Sadiku, "Elements of electromagnetics", Oxford, August, 2000, ISBN: 019513477X

[62] C. Shafai, G. Bridges, communications by emails on MEMS cantilever fabrication at Alberta Microelectronics Centre, Aug. 1996